

**POWER SCALING AND FREQUENCY STABILIZATION
OF AN
INJECTION-LOCKED LASER**

BY

RUSSELL F. TEEHAN

B.S. Physics, United States Air Force Academy, 1993
M.S. Applied Physics, Georgia Institute of Technology, 1994

DISSERTATION

Submitted in Partial Fulfillment of the
Requirements for the Degree of

**Doctor of Philosophy
Optical Sciences**

The University of New Mexico
Albuquerque, New Mexico

May, 2000

© 2000, Russell F. Teehan

Dedication

I would like to dedicate this thesis to my bride-to-be: Michelle Leigh Coffman. Her support over the past several years has made this endeavor a much more pleasant experience.

Acknowledgements

I have always been one to surround myself with individuals who challenge me in one aspect of life or another. Over the course of this research effort, I was fortunate to befriend two individuals who always challenged me to learn more: Mr. Joshua Bienfang and Mr. Nathan Brilliant. I would especially like to thank Josh, not only for encouraging me to obtain a full understanding of all the experiments we worked on together, but also for keeping me sane over the past few years by forcing me to take time out to “smell the roses” every now and then.

Also, I would like to thank Dr. Wolfgang Rudolph for taking on the role of my primary advisor. He constantly challenged me to think before I spoke.

Finally, I wish to acknowledge the support of Dr. Craig Denman and the USAF Research Laboratory.

**POWER SCALING AND FREQUENCY STABILIZATION
OF AN
INJECTION-LOCKED LASER**

BY

RUSSELL F. TEEHAN

ABSTRACT OF DISSERTATION

Submitted in Partial Fulfillment of the
Requirements for the Degree of

**Doctor of Philosophy
Optical Sciences**

The University of New Mexico
Albuquerque, New Mexico

May, 2000

**Power Scaling and Frequency Stabilization
of an
Injection-Locked Laser**

by

Russell F. Teehan

B.S. Physics, United States Air Force Academy, 1993

M.S. Applied Physics, Georgia Institute of Technology, 1994

Ph.D. Optical Sciences, University of New Mexico, 2000

ABSTRACT

The power scaling and frequency stabilization aspects of a high power, injection-locked, arc-lamp pumped Nd:YAG rod laser at 1.064 μm are considered. A complete theoretical analysis is performed on the Pound-Drever-Hall injection-locking technique used to lock the oscillation frequency of a high power laser to that of a low power frequency-stable laser. The explicit form of the injection-locking error signal is derived and an effective frequency noise control loop is established, which serves as a building block for describing more elaborate stabilization techniques. I achieve a 24-W, TEM₀₀, linearly-polarized (97:1) output with an M^2 of 1.07, using one such elaborate stabilization technique. I demonstrate the similarity between the frequency stability of the output field of an external cavity frequency-doubled laser and the injection-locked laser. I establish a frequency reference at 1 μm with a frequency stability of 10^{-13} at one second by locking the frequency-doubled NPRO to an electronic transition in I_2 .

Table of Contents

List of Figures.....	xi
List of Tables	xiv
CHAPTER 1. Introduction	1
1.1 Motivation	1
1.2 Achieving a High Power Frequency-Stable Output	2
1.3 Overview	5
CHAPTER 2. Power Scaling.....	10
2.1 Limitations.....	10
2.2 Thermo-Optical Model.....	13
2.3 Optimizing the Slave Resonator.....	15
2.4 Experiment	16
2.5 Results.....	19
2.6 Discussion	21
2.7 Summary	22
CHAPTER 3. Frequency Stabilization Theory	24
3.1 Phase and Frequency Noise.....	24
3.2 Frequency Control Theory (Time Domain Analysis).....	27
3.3 Control Loop Elements	30
3.3.1 Discriminator	30
3.3.2 Actuator	31
3.3.3 Servo	32
3.4 Frequency Control Theory (Frequency Domain Analysis).....	35

3.5 Summary	38
CHAPTER 4. Locking a Laser to a Fabry-Perot	40
4.1 Derivation of Error Signal.....	41
4.2 Frequency Control Theory	53
4.3 Measuring K_A , K_D , and δv_c	57
4.4 Common Measurements and Results.....	59
4.5 Summary	60
CHAPTER 5. Frequency Stabilization of an Injection-Locked Laser	61
5.1 Passive Injection Locking	61
5.2 Derivation of Error Signal.....	67
5.3 Frequency Control Theory	69
5.4 Measuring $K_{A,IL}$, $K_{D,IL}$, and v_{Lock}	75
5.5 Further Stabilization.....	76
5.6 Summary	82
CHAPTER 6. Injection-Locking Experiments.....	83
6.1 Measuring $K_{A,IL}$, $K_{D,IL}$, and v_{Lock} and determining PDH error signal is equally susceptible to master and slave laser frequency noise.....	84
6.2 Verifying master laser and slave resonator frequency noise transfer functions...	86
6.3 PDH Injection-Locking Stabilization Results	89
6.4 Comparing Techniques 1 and 2.....	90
6.5 Summary	94
CHAPTER 7. The Frequency-Doubler.....	96
7.1 Doubler Cavity Frequency Noise Transfer Functions	96

7.2 Verifying Frequency Noise Transfer Functions	103
7.3 Frequency-Doubler Stabilization Results	106
7.4 Summary	107
CHAPTER 8. Absolute Frequency Stabilization	108
8.1 Absolute Frequency References Near 1.064 μm	108
8.2 Overview	110
8.3 Characterizing the 1 μm In-Lab Reference	111
8.4 Absolute Frequency Stabilization Results.....	116
8.5 Summary	118
CHAPTER 9. Summary and Future Work.....	119
9.1 Primary Contributions.....	119
9.2 Future Work	122
9.3 Conclusion.....	123
REFERENCES	124
LIST OF VARIABLES (BY CHAPTER).....	129

List of Figures

Figure 2.1. Decomposition of linear polarization along r and ϕ axes.	11
Figure 2.2. Resonator containing arc-lamp pumped Nd:YAG rod.	14
Figure 2.3. Stability criteria and mode radius versus pump power for r and ϕ polarizations. (From Ref. 39).....	14
Figure 2.4. Injection-Locking schematic for power scaling experiments.	17
Figure 2.5. Coherent head experimental data.	19
Figure 2.6. Kigre head experimental data.....	20
Figure 2.7. Granit head experimental data.....	21
Figure 3.1. Frequency noise model.	25
Figure 3.2. Frequency noise control loop (time domain).	27
Figure 3.3. Servo design.	34
Figure 3.4. Gain and phase of open loop transfer function.	34
Figure 3.5. Frequency noise control loop (frequency domain).....	36
Figure 4.1. Optical schematic of locking laser to Fabry-Perot.	41
Figure 4.2. Steady state phase delay.....	46
Figure 4.3. Frequency noise transfer functions.....	48
Figure 4. 4. Frequency noise control loop (locking laser to Fabry-Perot).	53
Figure 4.5. Measuring K_A , K_D , and δv_c using PDH Error Signal.	58
Figure 5.1. Injection-Locking experimental set-up.....	61
Figure 5.2. Frequency noise transfer functions of master and slave onto injection-locked output.	66
Figure 5.3. Injection-Locking frequency noise transfer functions.	67

Figure 5.4. Frequency noise control loop (injection-locking).	69
Figure 5.5. Further stabilization.	76
Figure 5.6. Technique 1 frequency noise control loop.....	78
Figure 5.7. Technique 2 frequency noise control loop.....	79
Figure 5.8. Technique 3 frequency noise control loop.....	81
Figure 6.1. Optical schematic of injection-locking frequency stabilization experiments.	83
Figure 6.2. Verification of slave resonator frequency noise transfer function, $T_s(v_n)$	88
Figure 6.3. Relative frequency noise of the slave with respect to the master.....	90
Figure 6.4. Root Allan Variance comparison of Techniques 1 and 2.	92
Figure 6.5. Injection-locked spectral density of frequency noise (Technique 2).....	94
Figure 7.1. Frequency Doubler	96
Figure 7.2. Frequency noise transfer functions of the frequency-doubler.....	100
Figure 7.3. Frequency noise control loop (frequency-doubler).	101
Figure 7.4. Locking the Frequency-Doubled NPRO to a Fabry-Perot.....	103
Figure 7.5. Hansch-Coulliard error signal determination of $K_{D,D}$ and δv_c	104
Figure 7.6. Results of experiment to verify visible field frequency noise transfer functions.....	106
Figure 7.7. Relative frequency noise of doubler cavity with respect to incident NPRO.	106
Figure 8.1. In-Lab Iodine reference.....	111
Figure 8.2. Sample Iodine dispersion curve.	112
Figure 8.3. Frequency noise control loop (in-lab Iodine reference).....	113

Figure 8.4. Spectral density of frequency noise of the 1 μm reference..... 116

Figure 8.5. Root Allan Variance of the beatnote of our two identical 1 μm references. 117

List of Tables

Table 2.1. Model-predicted effects of varying various cavity parameters.	16
Table 2.2. Optimal slave resonator parameters for each of the pump heads used.	17
Table 6.1. Measurements of ν_{Lock} using error signal.....	86
Table 6.2. Comparison of beatnote linewidths.	92

CHAPTER 1. Introduction

1.1 Motivation

Since the invention of the laser, researchers have labored to improve its frequency stability and output power. High power, continuous-wave (cw), TEM₀₀, frequency-stabilized lasers serve as excellent pump sources for nonlinear optical processes, precision lasers for space-based measurements¹ and gravitational-wave detection,² and high-Q oscillators for coherent communication,³ high resolution spectroscopy,⁴ and the achievement of an optical clock. As an example of the stringent specifications of the lasers needed to support these fields, the space-based gravity-wave detector requires a cw, single-frequency laser of output power greater than 100 W and frequency stability less than 10^{-6} Hz/Hz^{1/2} at noise frequencies less than 1 kHz.^{5,6}

To create such a laser one generally first attempts to produce a high power, single-frequency source and then tries to improve the frequency stability of its output field. Several researchers have produced high power, cw, TEM₀₀ outputs with lasers containing one or more Nd:YAG rods side-pumped by individual diodes or diode arrays.⁷⁻⁹ The highest reported cw, TEM₀₀ output power of these transverse diode-pumped Nd:YAG lasers is 62 W.⁸ Next, one improves the frequency stability of the high power laser by either stabilizing its frequency to an external reference using somewhat complex frequency actuation schemes (Ref. 10) or injection-locking the high-power “slave” laser to a low-power frequency-stable “master” laser such as the NPRO (Non-Planar Ring Oscillator) laser created in 1985 by Kane and Byer.^{11,12} The injection-locked output displays both the high power of the slave laser and the frequency stability of the master laser. Since stabilization efforts of the NPRO have yielded frequency stabilities of

10^{-4} Hz/Hz^{1/2} at frequencies below 1 kHz,¹³ it is conceivable that a high power slave laser injection-locked to such a laser can achieve comparable stability. This makes injection-locking an appealing method of achieving a high-power frequency-stable output.

Several groups have injection-locked diode-pumped Nd:YAG rod lasers to NPRO lasers and then attempted to further stabilize the frequency of the injection-locked, TEM₀₀ output field by employing rather complex “global” stabilization schemes. The most noteworthy results of such efforts have been a 20 W output with a linewidth of 10 kHz,¹⁴ a 10 W output with a frequency stability of 50 Hz/Hz^{1/2} at 300 Hz,¹⁵ and a 2.2 W output with a frequency stability of 2×10^{-4} Hz/Hz^{1/2} at 1 kHz.¹⁶

In this thesis, I discuss my efforts to achieve a high power, linearly-polarized, TEM₀₀ output with an arc-lamp pumped Nd:YAG rod laser, injection-locked to an NPRO laser, and then characterize and improve its frequency stability. As a result of these efforts, I report obtaining a 24 W, TEM₀₀, $M^2 \sim 1.07$, linearly-polarized output with a linewidth of 1.5 Hz and a frequency stability of less than 1 Hz/Hz^{1/2} at 1 kHz.

Before giving an overview of the thesis by chapter, I review the general method of achieving a high power, frequency-stable, injection-locked output while pointing out the unanswered questions associated with this process that are addressed in this thesis.

1.2 Achieving a High Power Frequency-Stable Output

To meet the requirements of a particular application, one designs a stable slave laser cavity that can support the required output power. Although output powers of 10 W have been achieved with diode end-pumped Nd:YAG lasers,¹⁵ and output powers of nearly 18 W have been achieved with transverse lamp-pumped Nd:YAG rod lasers,¹⁷ it is generally agreed that transverse diode-pumping is required to achieve output powers

greater than 30 W.¹⁸ However, as the transverse pump power is increased, the thermal loading of the Nd:YAG rod increases, inducing both thermal lensing and birefringence.¹⁹

The thermo-optical model presented by Murdough accounts for the thermal lensing and birefringent aspects of the Nd:YAG rod and creates an optical 2x2 matrix for the rod as a function of transverse pump power.²⁰ The key assumption of the model is that the induced radial temperature distribution is azimuthally symmetric. To scale the output power of the slave laser, one can use this model to optimize the slave resonator length and intracavity elements to create a stable slave resonator at higher pump powers. But how accurately does the model predict the stable operating regime of the linearly-polarized, injection-locked laser? Also, in the absence of birefringent compensation, what limits the power-scaling efforts using an Nd:YAG rod: the bifocal property of the rod or the stress fracture limit of the rod?

After scaling the power of the slave laser, one sets out to improve the frequency stability of the injection-locked output. To optimally reduce the frequency noise of the high power output field, one must understand how the noise of the incident master laser and the unseeded slave laser contribute to the overall noise of the injection-locked output. Siegman has performed an extensive analysis in which he solved the damped, driven wave equation describing the circulating field of the slave laser to obtain two coupled amplitude and phase relations for the output injection-locked electric field.²¹ Two groups have since solved these coupled equations to show that the transfer function of the master laser frequency noise onto the injection-locked output is a low pass filter and that of the slave resonator noise is a high pass filter, both of corner frequency equal to the lock range frequency (ν_{Lock} , defined in Chapter 5).²²⁻²⁴ Thus, the problem of achieving a frequency-

stable output centers on reducing the low frequency noise of the master, and the high frequency noise of the slave. However, this assumes that the laser remains injection-locked, which is not the case when the original (unseeded) slave resonator frequency noise, or that of the master laser, exceeds the lock range frequency.

To insure the laser remains injection-locked, researchers use the Pound-Drever-Hall (PDH) FM sideband locking technique.²⁵ This technique is most-often used to stabilize the output frequency of low-power solid-state lasers, such as the NPRO, to the mHz level by locking the instantaneous frequency output to the resonant frequency of a high-finesse optical resonator.²⁶⁻²⁸ This same technique is used to lock the oscillation frequency of the slave laser to the instantaneous frequency input of the master laser. While much is known about the PDH locking of a laser to a Fabry-Perot, very little is known about the PDH injection-locking experiment. The explicit form of the error signal is needed to establish an effective control loop diagram and to determine the optimal experimental parameters yielding the minimum injection-locked spectral density of frequency noise. This control loop can be used to determine methods of measuring the relative frequency stability of the slave laser with respect to the master laser and the optimal method of further stabilizing the frequency of the injection-locked output.

To further suppress the noise of the injection-locked output field, one can either prestabilize the frequency of the master laser or detect the frequency noise of the injection-locked output and feed it back to the master laser. The latter option treats the master laser as a frequency actuator in the master/slave injection-locked system. Since the frequency noise transfer function of the master laser onto the injection-locked output is a low pass filter, the optimal loop detects the injection-locked noise and feeds the low

frequency noise negatively back to the master laser and the high frequency noise to a phase modulator placed in the path of the high power output beam.²⁴

By detecting and reducing the frequency noise of the injection-locked output field with respect to a frequency reference, the stability of the injection-locked output can at best duplicate the frequency stability of the reference. Spectroscopy and coherent communications hinge upon day to day repeatability and knowledge of the exact frequency of the laser. Repeatability is lost and long-term stability reduced when a laser is locked to a reference cavity since the drift of the reference cavity length over a period of time causes a consequent drift in the reference frequency. To reduce the drift of the reference cavity length, researchers have cleverly stabilized the length of the cavity by mixing down the heterodyne beatnote of two lasers locked to adjacent modes of the same cavity and using this signal to lock the Free Spectral Range (FSR) to an electronic oscillator.²⁹ This technique improves the long term stability of the beatnote frequency of the two lasers, but does not improve the absolute frequency stability of either of the lasers locked to this resonator since the absolute frequency of the resonance can still drift with time. To eliminate the frequency drift of the reference one compares the instantaneous laser frequency to the absorption frequency of an atomic or molecular transition. Since the frequency of such a transition is fixed, it serves as an absolute frequency reference, significantly improving the long-term stability of the laser.

1.3 Overview

In Chapter 2, I use the thermo-optical model of Mardough to optimize the slave laser cavities of three arc-lamp pumped heads to scale the injection-locked, TEM₀₀, linearly-polarized output power to 28.5 W, 26.5 W, and 25 W. In the process, I verify the

accuracy of the model in predicting the stable operating regime of a linearly-polarized field. I report that when the assumptions of the model are valid, in the absence of birefringence compensation techniques, the bifocal property of the rod is the key limiting factor in the power scaling effort. However, I find that when the induced temperature distribution created within the rod is asymmetric it becomes the chief limitation.

The remainder of the thesis addresses the various topics encountered in the effort to improve the frequency stability of the injection-locked laser. Note that these chapters are not arranged chronologically, but rather in the order in which I believe they complement each other most effectively. In actuality, most of the experiments described in Chapter 6 were used to develop the PDH injection-locking theory of Chapter 5. This theory was then used to augment the previous theory associated with the PDH locking of a laser to a Fabry-Perot (discussed in Chapter 4) which was later used to describe the frequency stabilization of the external cavity frequency-doubler (discussed in Chapter 7).

In Chapter 3, I introduce the control theory method of describing the problem of stabilizing the frequency of a laser to a reference. I introduce the particular elements of the feedback loop (the discriminator, servo, and actuator) which are common to all of the stabilization efforts of this thesis and analyze the effective frequency noise control loop created in both the time and frequency domains. The results of the time domain analysis reveal the explicit relationship between the magnitude and phase of the open and closed loop transfer functions of the feedback loop. This relationship was not present in the literature, and is needed to understand the trade-off between gain and loop efficiency when designing the servo element. I alter the frequency domain analysis of Ref. 30 to include the relative frequency stability of the reference and use the resulting frequency

noise control loop to derive explicit relationships between the voltage signals measured at two points in the control loop (labeled N_e and N_a) and the open and closed loop spectral density of frequency noise of the laser. This simple frequency noise control loop serves as the starting point in modeling the frequency stabilization experiments of this thesis.

In Chapter 4, I alter the well-documented theory of locking a laser to a Fabry-Perot by performing the PDH error signal derivation in a new manner (using the damped, driven wave equation describing the circulating field of the Fabry-Perot). This derivation is more beneficial than the previous derivation of Day (Ref. 30) since it not only reveals the contribution of the frequency noise of the laser, but also the frequency noise of the reference cavity. It also reveals the explicit relationship describing the coupling of the amplitude and frequency noise of the incident field and the circulating and reflected fields of the resonator. I use the results of this derivation to review the optimal incident laser parameters yielding the minimal achievable closed loop spectral density of frequency noise.³¹ Next, I alter the frequency noise control loop of Chapter 3 to display the parameters of this new PDH error signal derivation and then use the loop to determine the relations between the open and closed loop spectral density of frequency noise of the laser and the N_e and N_a point measurements. Although I find that the simple control loop of Chapter 3 yielded the exact same relations, I later show that this new derivation and its complex control loop are beneficial in describing the frequency stabilization of the external cavity frequency-doubler of Chapter 7.

In Chapter 5, I present the control theory that I developed to accurately model the various measurements I made to characterize the frequency stability of the injection-locked laser. The format of Chapter 5 is very similar to that of Chapter 4 so that straight-

forward comparisons can be made between the PDH locking of a laser to a Fabry-Perot and the PDH injection-locking experiment. I use the theory presented by Siegman and the frequency noise transfer functions of Barillet to derive the PDH error signal. I also derive an explicit expression for the lock range frequency, altered slightly from previously reported expressions to account for parameters particular to the PDH technique. I introduce an effective PDH injection-locking control loop block diagram and discuss how the N_e and N_a point measurements can be used to determine the open and closed loop relative spectral density of the frequency noise of the slave laser with respect to the master laser. The results suggest that the simple control loop of Chapter 3 can not adequately represent the entire injection-locking process, indicating this more complicated control loop diagram is necessary for modeling this experiment. Next, I review the global frequency noise suppression techniques presented in the literature (labeled Techniques 2, and 3)^{23,24} and compare them with another global suppression technique (prestabilization of the master laser, labeled Technique 1), which is generally assumed to be the worst stabilization scheme and thus ignored in the literature. I show that given the feedback loop bandwidth limitations and experimental parameters common to our experiments, Technique 1 should yield comparable results to Technique 2.

In Chapter 6, I list the results of various experiments I performed that led me to the theoretical description of injection-locking control theory presented in Chapter 5. I list the experimental results obtained when implementing Techniques 1 and 2 to improve the frequency stability of a high-power injection-locked laser. I report achieving a 24 W, TEM₀₀, $M^2 \sim 1.07$, linearly-polarized injection-locked output with a linewidth of 1.5 Hz

and a frequency stability of less than $1 \text{ Hz/Hz}^{1/2}$ at 1 kHz, using a “noisy” arc-lamp pumped head and the worst possible stabilization scheme (Technique 1).

The damped, driven wave equation analysis for the Fabry-Perot, in Chapter 4, and the slave laser resonator, in Chapter 5, produce similar expressions relating the frequency noise of the circulating field to the noise of the incident laser and the unseeded resonator. In Chapter 7, I use this same analysis to describe the frequency stabilization of an external cavity frequency-doubled laser. I also show that the optimal theoretical frequency stabilization technique for the injection-locked laser (Technique 3 of Chapter 5) is also the optimal technique for minimizing the frequency noise of the doubled field.

In Chapter 8, I discuss the absolute frequency stabilization of a $1.064 \text{ }\mu\text{m}$ laser. I introduce five known molecules with transitions neighboring this wavelength: C_2HD , C_2H_2 , CO_2 , Cs_2 , and I_2 ($\sim 532 \text{ nm}$). I characterize the frequency stability of one of the two frequency references we produced,³² using the well-documented modulation transfer scheme to lock the frequency-doubled NPRO to a hyperfine component of an electronic transition in I_2 .³³ I report achieving a spectral density of frequency noise of $0.3 \text{ Hz/Hz}^{1/2}$ for noise frequencies less than 400 Hz and a frequency stability of 10^{-13} for a time interval of one second. I also show, via comparison, that these results are comparable to the results of similar lasers presented in the literature.^{33,34} These frequency references will be used in the future to characterize the frequency stability of an injection-locked laser stabilized to an absolute frequency reference at $1.064 \text{ }\mu\text{m}$.

In Chapter 9, I review the key results of this dissertation and discuss the future experiments and theoretical analyses necessary to further improve the frequency stability of an injection-locked laser at $1.064 \text{ }\mu\text{m}$.

CHAPTER 2. Power Scaling

In this chapter, I review the limitations of scaling the linearly-polarized, TEM_{00} output power of a ring laser resonator containing a side-pumped Nd:YAG rod. I briefly review the thermo-optical model created by Murdough and Denman²⁰ to monitor the mode-size through the rod and laser resonator stability criteria as a function of transverse pump power. I discuss the methods used to optimize certain laser resonator parameters to shift the stable operating regime of the linearly-polarized mode, predicted by the model, to higher transverse pump powers.

Using these optimization techniques, I report achieving over 25 W, TEM_{00} , linearly-polarized output with three different arc-lamp pumped Nd:YAG rod lasers. The highest polarized, TEM_{00} output power previously reported with a laser containing a single arc-lamp pumped head was 18 W and containing two pump heads was 24 W.¹⁷

2.1 Limitations

Consider a constrained cylindrical Nd:YAG rod transversely pumped and cooled with perfect azimuthal symmetry. Solving the one dimensional heat equation reveals the temperature distribution in the rod varies quadratically along the radial axis.¹⁹ Since the index of refraction is linearly dependent on the temperature of the material, it too varies quadratically, and the rod acts as a quadratic lens duct.^{35,36} The temperature gradient created along the rod's radial axis induces thermal strains that alter the index of refraction at each point in the rod. This strain-induced change in the index of refraction varies linearly with the photoelastic coefficient, which differs along the r and ϕ axes of the Nd:YAG rod cross-section, defined in a traditional cylindrical coordinate system as shown in Figure 2.1. It is clear by inspection of Figure 2.1 that the polarization at each

point in the cross section of the linearly-polarized beam incident along the longitudinal axis of the rod can be decomposed into an r and ϕ component. Since the indices of refraction differ along these axes, the incident beam undergoes a birefringent effect.

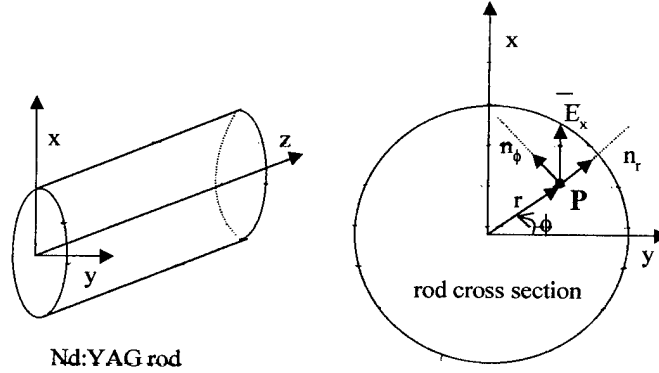


Figure 2.1. Decomposition of linear polarization along r and ϕ axes.

Koechner treated this problem extensively and obtained an expression similar to Equation 2.1 for the radial index of refraction dependence.¹⁹ The index of Equation 2.1 is the sum of the index at the rod center, the temperature-induced index variation, and the stress-induced variation.

$$n_{r,\phi}(r) = n_0 - \frac{1}{2} \cdot \left[\frac{\eta_T \cdot P_{in}}{\pi \cdot r_0^2 \cdot L_r \cdot K} \cdot \left(\frac{1}{2} \cdot \frac{dn}{dT} + n_0^3 \cdot \alpha \cdot C_{r,\phi} \right) \right] \cdot r^2 \quad (2.1)$$

Where n_0 is the index of refraction at the rod center, r_0 is the rod radius, L_r is the rod length, K is the thermal conductivity, α is the thermal coefficient of expansion, $C_{r,\phi}$ are the radial and tangential photoelastic coefficients, P_{in} is the transverse pump power, and η_T is the percentage of P_{in} absorbed by the rod as heat. The primary difference between arc-lamp pumped systems and transverse diode-pumped systems in the current discussion is the value of η_T . For diode-pumped systems η_T is much less than it's lamp-pumped counterpart due to the much higher efficiency in the diode-pumping process. Equation 2.1 can be simplified and compared with the equation of a lens. In so doing, it can be

shown that the rod acts as a bifocal lens whose focal lengths along the r and ϕ axes are inversely proportional to the transverse pump power but to varying degrees. For Nd:YAG, the ratio of the focal length of the ϕ polarization is 1.2 times greater than the focal length of the r polarization at any given pump power. To resonate a linearly-polarized mode one accounts for this bifocal effect and ensures that both the r and ϕ modes satisfy the stability criterion of the laser resonator.

Two methods of scaling the output power of the laser are to increase the transverse pump power or augment the TEM_{00} mode size through the rod to increase the gain volume employed. Each process has its limits. First, as the pump power is increased, the amount of pump power dissipated as heat in the rod increases, causing a consequent rise in the surface stresses of the rod. The stress fracture limit is reached when the surface stress exceeds the tensile strength of the rod. The efficiency of the pump irradiance sets the value of η_T and determines the actual achievable transverse pump power—making diode-pumped systems more appealing than their inefficient arc-lamp pumped counterparts. Second, as the spot size of the circulating field increases, the range of transverse pump powers for which the r and ϕ modes are both stable diminishes, due to the bifocussing effect of the rod.³⁷ Eventually, a point is reached at which the overlap of these modes is so small that perturbations of the rod's effective focal length cause one or both modes to become unstable and lasing to cease. The maximum TEM_{00} spot size was reported by Cerullo *et al.* to be nearly 1 mm³⁷ and later by Murdough and Denman to be on the order of 1.1 mm.²⁰

Another limitation to the power scaling effort is the azimuthal symmetry of the temperature distribution generated in the rod's cross section, resulting from either

asymmetric pumping or cooling. This non-uniformity causes optical distortion through the rod and increases the loss of the circulating field. It can also increase the gain of higher-order modes competing for gain with the TEM₀₀ mode.³⁸

2.2 Thermo-Optical Model

After a bit of manipulation and grouping of terms, Equation 2.1 can be rewritten as shown in Equation 2.2, in terms of the constant $\beta_{r,\phi}$ defined in Equation 2.3.^{20,39}

$$n_{r,\phi}(r) = n_0 - \frac{1}{2} \cdot \beta_{r,\phi} \cdot P_{in} \cdot r^2 \quad (2.2)$$

$$\beta_{r,\phi} = \frac{\eta_r}{\pi \cdot r_0^2 \cdot L_r \cdot K} \cdot \left(\frac{1}{2} \cdot \frac{dn}{dT} + n_0^3 \cdot \alpha \cdot C_{r,\phi} \right) \quad (2.3)$$

It is clear that $\beta_{r,\phi}$ is dependent on material parameters and the efficiency of the pumping scheme employed. A recently reported thermo-optical model uses Equation 2.2, treats the pumped portion of the Nd:YAG rod as a quadratic lens duct, and outputs an optical 2x2 matrix for each of the r and ϕ polarizations.³⁹ Multiplying this 2x2 matrix by the matrices determined for the unpumped portion of the rod and the rod endface curvatures yields a single matrix for the rod for each polarization as a function of $\beta_{r,\phi}$ and P_{in} . Since β_r and β_ϕ are constants for a given pump head and can be determined experimentally,³⁹ P_{in} is the only independent variable. Note that $\beta_{r,\phi}$ are the only parameters that change with Nd:YAG rod, pumping scheme, or pump orientation. Further, Equations 2.1-2.3 are valid for any pump scheme creating an azimuthally symmetric temperature distribution.

The side-pumped rod is placed into the resonator of Figure 2.2 (which later serves as the slave laser for the injection-locking experiments), and optical 2x2 matrices are established for the optical path lengths and intracavity elements encountered by the

circulating field. These matrices and the matrix for the rod are used to determine the stability criteria of the resonator and the spot size of the circulating field (at the entrance of the rod) as a function of P_{in} . Figure 2.3 displays a sample spot size and stability criteria versus transverse pump power for a particular arc-lamp pumped head.

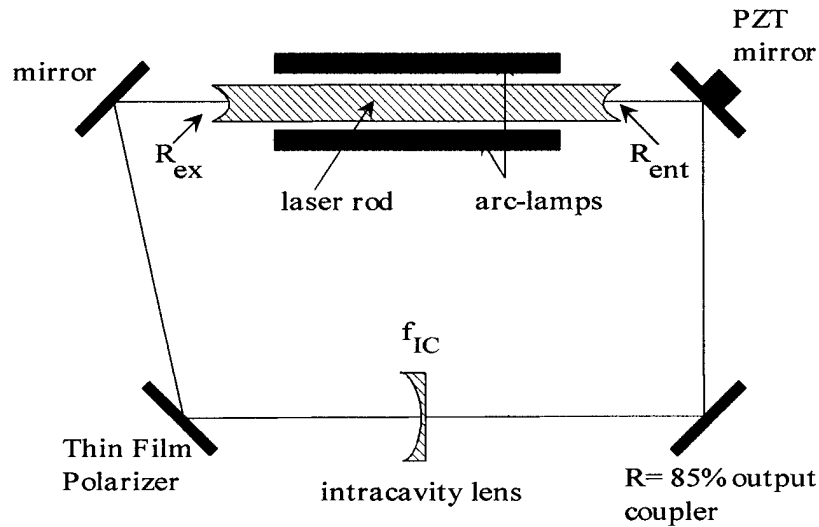


Figure 2.2. Resonator containing arc-lamp pumped Nd:YAG rod.

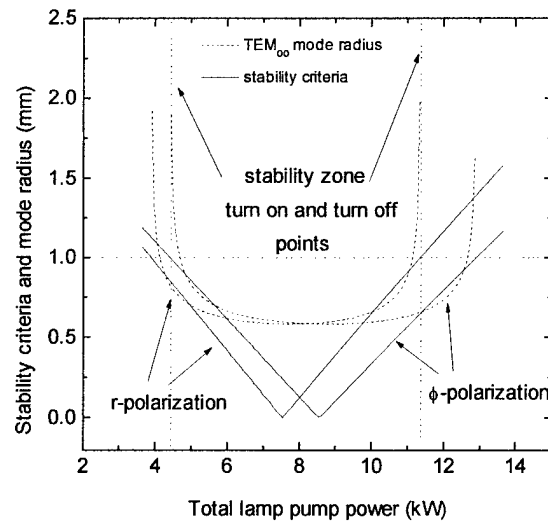


Figure 2.3. Stability criteria and mode radius versus pump power for r and ϕ polarizations. (From Ref. 39)

To produce a linearly polarized output, both the r and ϕ components must be stable (i.e. have stability criteria less than one). Therefore the overall stability zone of the

linearly polarized field is the range of pump powers for which both the r and ϕ components are independently stable. Figure 2.3 shows that as the radius of each component increases beyond approximately 1.1 mm, its corresponding stability criterion exceeds one--the limit of the stable operating regime. The edges of the overall stability zone, shown in Figure 2.3, consist of the pump power at which the ϕ polarization becomes stable, labeled as the turn-on point, and the pump power at which the r polarization becomes unstable, labeled as the turn-off point.

2.3 Optimizing the Slave Resonator

To scale the power of the TEM₀₀ linearly-polarized output, it is necessary to shift the overlap of the r and ϕ stability zones to higher pump powers and increase the spot size of the circulating field entering the Nd:YAG rod near the limit of 1.1 mm.

To shift the stability zones to higher pump powers, the rod endfaces are curved and the slave resonator length is reduced. Placing a concave curvature on the rod endfaces compensates for the thermal lensing of the rod and the lensing effects of the endface bulging that occurs as the thermal loading increases. Reducing the length of the resonator increases the focal power that the thermal lens may have while still creating a stable resonator. Reducing the resonator length also reduces the spot size in the rod. To correct this, an intracavity diverging lens is used to increase the spot size in the rod. Table 2.1 lists the model-predicted effects of varying the cavity length (L_c), rod endface curvatures (R_{end}), and focal length of the diverging lens (f_{lc}) on the mode size and stability criterion for each of the r and ϕ polarizations.

Parameter Alteration	Significant Effect on mode radius and stability zone
Decrease $ R_{\text{end}} $	Both r and ϕ stability zones shift to higher pump powers. Overlap of r and ϕ stability zones diminishes.
Decrease L_c	Pump power stability zone turn-off point increases. Mode size diminishes.
Decrease $ f_{\text{IC}} $	Pump power stability zone turn-on point increases. Mode size increases. Overlap of the r and ϕ stability zones diminishes.

Table 2.1. Model-predicted effects of varying different cavity parameters.

To decrease $|R_{\text{end}}|$, the rod manufacturer grinded concave surfaces into the end-faces of the rod. Decreasing $|R_{\text{end}}|$ and $|f_{\text{IC}}|$ refers to reducing the concave radius of curvature of the rod endface and the biconcave lenses, respectively (e.g. from $-\infty$ to -100 cm to -50 cm, etc.).

2.4 Experiment

Using the model, I optimized slave resonators containing three different arc-lamp pump heads, to scale their linearly-polarized, TEM_{00} , injection-locked output power to the highest levels ever achieved for a single arc-lamp pumped head. I used a Coherent Antarres head containing a 4 mm x 100 mm rod, and lamp-pumped heads from Kigre Inc. and Granit Inc., each with a 5 mm by 150 mm rod. All rods were 0.8 at. % Nd doped and operated with a coolant temperature of approximately 10°C . The Granit and Coherent heads both used a gold, dual-elliptical reflector housing, while the Kigre head had a BaSO_4 close-coupled reflector housing. Each head employed a slightly different pumping and/or cooling scheme and thus displayed a different $\beta_{r,\phi}$ value. For each head, $\beta_{r,\phi}$ was determined (using the procedure outlined in Ref. 39) and the parameters of Table 2.1 were adjusted. The upper limit of the pump power, $P_{\text{in,max}}$, was either set by previous experience or manufacturer recommendations and was chosen several kilowatts less than the stress fracture limit power. Table 2.2 lists the final optimized slave laser parameters

for each arc-lamp pumped head. Since all heads had nearly the same physical dimensions, the minimum cavity length obtainable was nearly 110 cm.

Pump Head	L_c (cm)	R_{end} (cm)	f_{ic} (cm)	TEM ₀₀ Power (W)	$P_{in,max}$ (kW)
Coherent	110	-80	-30	26.7	10.75
Kigre	110	-80	No Lens	22	7.15
Granit	110	-80	-50	25	15

Table 2.2. Optimal slave resonator parameters for each of the pump heads used.

For each head, a slave laser resonator was configured with the optimized parameters of Table 2.2 and injection-locked with a 500-mW Lightwave Electronics Series 122 NPRO (operating near $1.064\text{ }\mu\text{m}$), as shown in Figure 2.4.

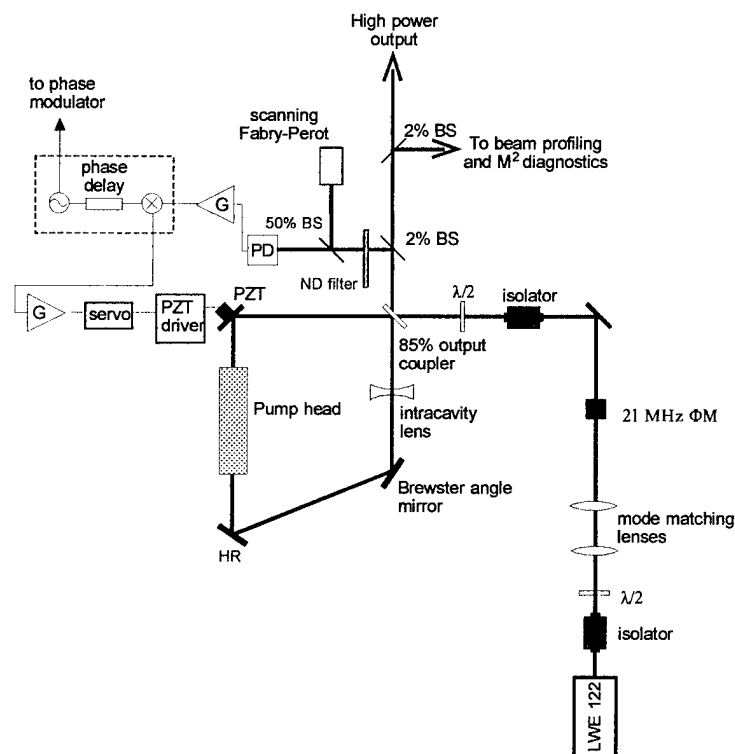


Figure 2.4. Injection-Locking schematic for power scaling experiments.

The frequency noise of the slave laser was sufficient to keep the laser from remaining injection-locked for any period of time. Thus, the frequency lock of the slave to the master was obtained using the PDH FM sideband-locking scheme, the details of

which will be discussed in Chapter 5. I did not optimize the output coupler of the slave resonator for each pump head by determining the round-trip cavity losses as discussed by Koechner.⁴⁰ Instead I chose the coupler that yielded the highest output power with the Coherent head, $R_{oc} = 85\%$, and assumed that the losses of each head were comparable. The injection-locked output was monitored using a Newport Supercavity optical spectrum analyzer (OSA), a Spiricon Laser Beam Analyzer, a power meter, and a Coherent Mode Master. The OSA monitored the ratio of the TEM_{00} power to any higher order modes, the Beam Analyzer monitored the output beam cross section, the power meter took all of the power scaling data (recorded as a function of electrical power supplied to the arc lamps), and the Mode Master measured the M^2 value. The high power output was typically better than 97% linearly polarized with an $M^2 \sim 1.07$.

To verify the model, the slave resonator was first constructed with a flat-endfaced rod and the injection-locked TEM_{00} output power was measured at discrete pump power intervals. These output power measurements were then plotted versus lamp pump power along with the model-predicted r and ϕ polarization stability criterion. A linear fit to the flat rod data was performed and extrapolated to the model-predicted stability zone turn-off power of the curved rod case (with identical mode size) to predict the maximum TEM_{00} output power. For all pump heads, the peak linearly-polarized output power was achieved at or near the predicted stability zone turn off point. The curved rod was then placed in the pump head and the TEM_{00} output power was again measured as a function of lamp pump power. The results of the flat rod data (its extrapolation to higher pump powers), the curved rod data, and the model-predicted r and ϕ mode stability zones and mode sizes for the curved rod case were all plotted on a single graph for analysis.

2.5 Results

Figures 2.5-2.7 show the experimental results obtained with the Coherent head, the Kigre head, and the Granit head, respectively.

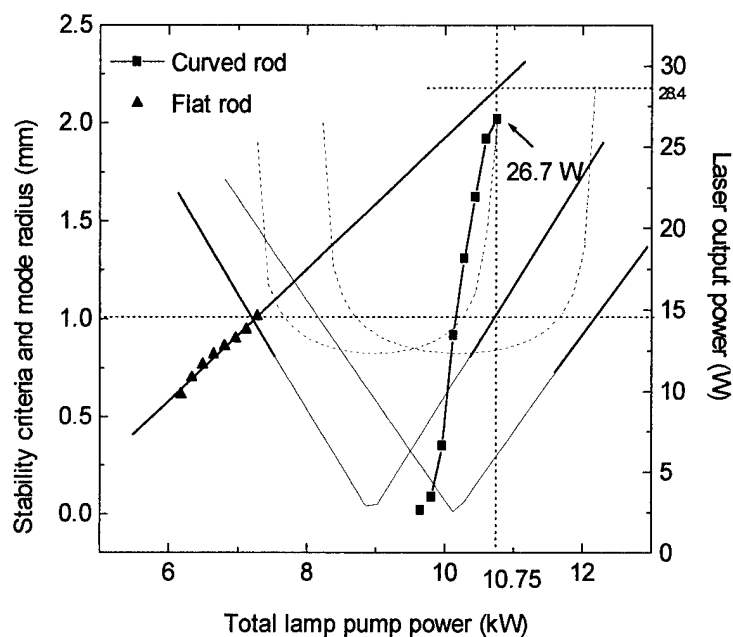


Figure 2.5. Coherent head experimental data.

In Figure 2.5, the maximum Coherent head curved rod output power obtained was approximately equal to the linear extrapolation of the flat rod data. The cavity was designed for a rod with 80-cm concave endface radii of curvature and used a -30-cm focal length intracavity lens placed opposite the pump head to ensure the stability zone turn-off power point equaled $P_{in,max}$ (10.75 kW). This configuration produced a 26.7 W, stable, TEM_{00} injection-locked output at the upper cut-off of the r-polarization stability zone. The output power obtained in this case was close to the predicted value of 28.4 W at the intersection between the extrapolated line from the flat rod data and the vertical line drawn at $P_{in,max}$. Another data set taken with this head yielded an output of 28.5 W at

a lamp power of 10.75 kW with an intracavity lens of $f_{IC} = -25$ cm. Without the lens, this design generally yielded an output power of 18 W at a pump power of nearly 7.75 kW.

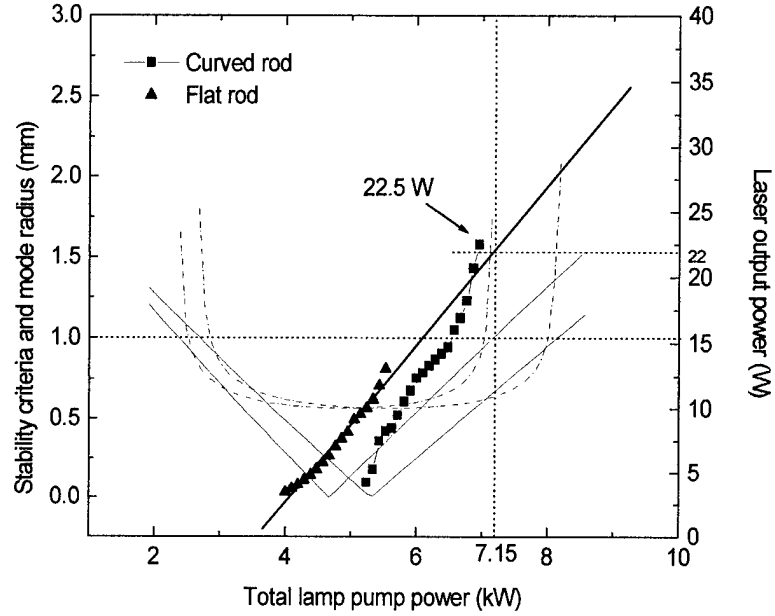


Figure 2.6. Kigre head experimental data.

Figure 2.6 displays the results of testing the Kigre head. Again, the curved rod output power data approaches the maximum value predicted by the extrapolation of the flat rod data to the head's maximum stable pump power point. For the 110-cm cavity, the highest output power obtained was 22.5 W at a pump power of 7.0 kW, which was very close to the 22 W predicted by the extrapolation of the flat rod data. At pump powers above 6.53 kW the output beam was increasingly multimodal. To diminish the off-axis modes, the beam was apertured at the entrance of the rod. Another data set taken with this head yielded 26.5 W TEM_{00} output with $f_{IC} = -50$ cm at a pump power of 6.67 kW.

The Granit head, shown in Figure 2.7, was operated up to 15 kW of pump power while performing the standing wave cavity experiments to determine the $\beta_{r,\phi}$ value. The ring cavity was designed to be stable up to this pump power, but the maximum TEM_{00}

injection-locked power was obtained at 9 kW. Beyond this point, the output laser power was increasingly multimodal and the beam required aperturing at the exit of the rod. While the multimodal output beam power always increased with increased lamp pump power, the TEM_{00} power obtained after aperturing the higher order modes either leveled off or even decreased beyond 9 kW of pump power. Hence, while the model predicted that the cavity would be stable out to 12.5 kW, the highest TEM_{00} injection-locked power obtained with the Granit head was 25 W at a lamp pump power of 9.0 kW.

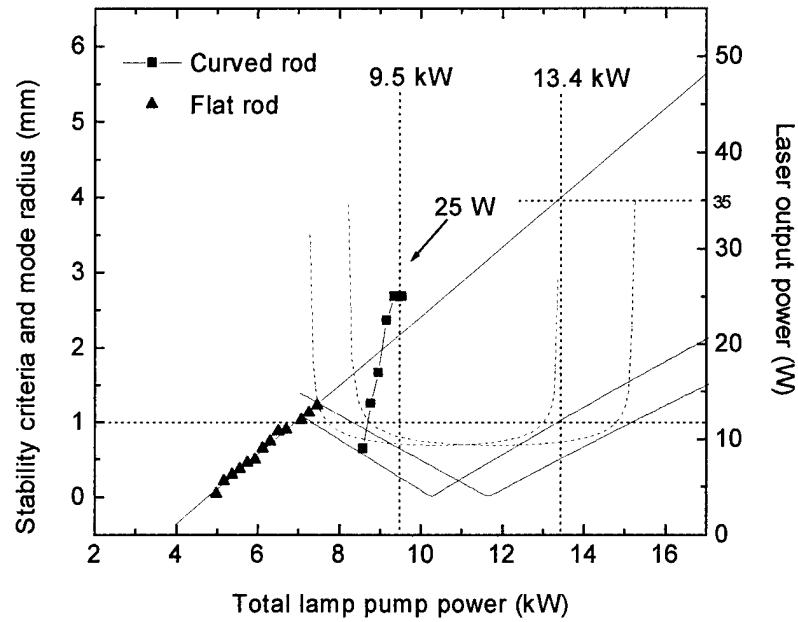


Figure 2.7. Granit head experimental data.

2.6 Discussion

Figures 2.5 and 2.6 display excellent agreement between the model's predicted stability zone overlap versus lamp pump power and that obtained experimentally. In these cases, the linearly-polarized, TEM_{00} output power increased with added pump power until the r- polarization mode became unstable. The losses of the injected, linearly-polarized, TEM_{00} field continued to increase until the circulating field arising

from the injected master laser field no longer exceeded the amplitude of other slave laser modes and injection-locking ceased.

On the other hand, the Granit head data of Figure 2.7 showed mixed agreement with the model. The lowest injection-locked output power data point was obtained at the predicted stability zone turn-on power point, 8.5 kW. At this point, both the r and ϕ components of the linearly-polarized circulating field are stable and the losses of the injected master laser are small enough to obtain lock. However, the maximum TEM_{00} output power obtained with this head was found at a pump power of 9.5 kW; much lower than the expected $P_{in,max}$ of 13.4 kW. The discrepancy between the model and the experimental data was likely caused by an asymmetric temperature distribution within the rod. Such an asymmetric distribution invalidated the uniformity assumptions of the model and induced optical aberrations resulting in increased losses for the TEM_{00} mode. As the losses increased, the laser became increasingly multimodal as the pump power was increased beyond 9.5 kW. By aperturing the circulating field at the entrance to the Nd:YAG rod, I increased the losses of the higher order modes to ensure the laser oscillated in the TEM_{00} mode, but at a reduced power due to the losses of the aperture.

2.7 Summary

Based on these experiments it is clear that the thermo-optical model can be used to optimize parameters of a laser resonator containing a side-pumped Nd:YAG rod. However, care must be taken to ensure a symmetric temperature distribution is maintained at higher pump powers to reduce the losses of the linearly-polarized TEM_{00} mode. Note that no attempt was made to compensate for the birefringence of the rod. Recently reported compensation techniques could be used in conjunction with this model

to increase the overlap of the r and ϕ stability zones and increase the pump power limit, beyond the bifocussing limit, to the stress fracture limit of the rod.⁴¹

Using the optimization procedures outlined in Section 2.3, I achieved a linearly polarized, TEM₀₀ output power of 28.5 W, with an M^2 of 1.07, using a Coherent Antarres arc-lamp pumped head. This is the highest TEM₀₀ power of an injection-locked laser containing a single or even two lamp-pumped heads.

CHAPTER 3. Frequency Stabilization Theory

In this chapter, I discuss the problem of improving the frequency stability of a laser by comparing its frequency to that of a frequency reference and establishing a negative feedback loop to eliminate the erroneous frequency fluctuations. I introduce two of the feedback loop elements, the actuator and the servo, which are common to all of the experiments presented in the remainder of the thesis. Also, I introduce and augment the control loop diagram of Ref. 30, since this simple representation serves as the starting point in modeling the various complex stabilization experiments discussed in this thesis. The scope of the discussion will remain broad to ensure a proper introduction is made of the various terms and concepts used throughout this thesis.

3.1 Phase and Frequency Noise

Consider a laser whose output electric field frequency oscillates about a carrier frequency, ν_0 . A common method of representing the instantaneous frequency splits the total frequency into the sum of the carrier frequency and various Fourier noise components oscillating at frequency ν_n .⁴² This representation is shown in Equation 3.1 in terms of the carrier and noise radial frequencies, ω_0 and ω_n , respectively. Throughout the thesis, I interchange between frequency, ν_x in Hz, and radial frequency, ω_x in Rad/sec, where $\omega_x = 2\pi \nu_x$.

$$\tilde{E}_{Laser}(t) = E_0(t) \cdot e^{[i(\omega_0 t + \phi_{Laser}(t))]} = E_0(t) \cdot e^{i(\omega_0 t + \sum_n S_{\phi, Laser}(\nu_n) \sin(\omega_n t))} \quad (3.1)$$

Where E_{Laser} is the complex electric field, E_0 is the real field amplitude, $\phi_{Laser}(t)$ is the instantaneous phase noise of the field, and $S_{\phi, Laser}(\nu_n)$ is the amplitude (in Rad) of the phase noise term oscillating at frequency ν_n . In this thesis, I consider the contributions of

a single noise frequency, ν_n , assuming that this analysis holds equally true for each individual noise frequency. The instantaneous frequency of the field, $\nu_{\text{Laser}}(t)$, is the time derivative of the instantaneous phase term of Equation 3.1 as shown in Equation 3.2.

$$\begin{aligned}\nu_{\text{Laser}}(t) &= \frac{1}{2\pi} \cdot \frac{d}{dt} [\omega_0 t + \phi_{\text{Laser}}(t)] = \nu_0 + S_{\phi, \text{Laser}}(\nu_n) \cdot \nu_n \cdot \cos(\omega_n t) \\ &= \nu_0 + S_{f, \text{Laser}}(\nu_n) \cdot \cos(\omega_n t)\end{aligned}\quad (3.2)$$

The frequency of the laser oscillates about the center frequency, ν_0 , at the oscillation frequency, ν_n , with peak frequency deviation of $S_{f, \text{Laser}}(\nu_n)$, in Hz. The relation between $S_{\phi, \text{Laser}}(\nu_n)$ and $S_{f, \text{Laser}}(\nu_n)$ is shown in Equation 3.3.

$$S_{f, \text{Laser}}(\nu_n) = S_{\phi, \text{Laser}}(\nu_n) \cdot \nu_n \quad (3.3)$$

As an example, assume we eliminate or filter all of the frequency noise of the laser except the component oscillating at ν_n . Equation 3.2 suggests that the instantaneous frequency of the laser, $\nu_{\text{Laser}}(t)$, oscillates about ν_0 . The peak frequency deviation is $S_{f, \text{Laser}}(\nu_n)$ and the period of the oscillation is equal to $1/\nu_n$ as shown in Figure 3.1.

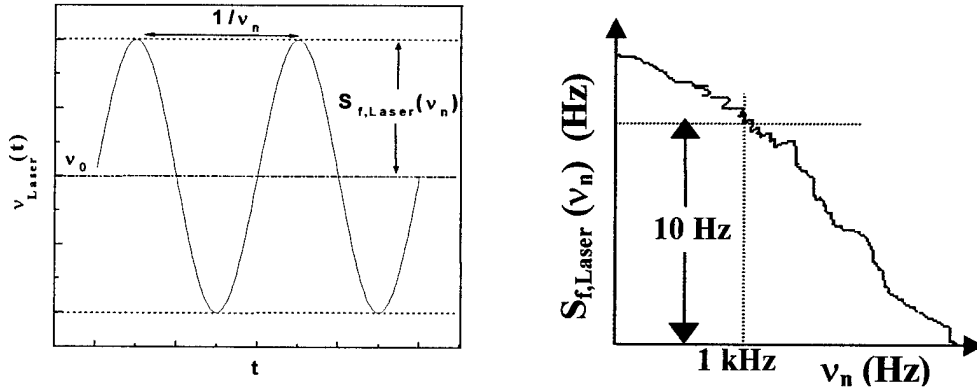


Figure 3.1. Frequency noise model.

In actuality, we can not isolate a particular noise frequency. Instead, there are methods of detecting the instantaneous frequency of the laser and performing a Fourier analysis to

yield a plot of the spectral density of frequency noise, as shown in the second plot of Figure 3.1. Ideally such a graph would plot the peak frequency excursion occurring at a given noise frequency, $S_{f,Laser}(v_n)$ in Hz, as a function of the noise frequency, v_n in Hz. I have shown this ideal case in Figure 3.1, and drawn dotted lines to the point in the plot depicting a frequency noise, $S_{f,Laser}(1\text{kHz}) = 10 \text{ Hz}$, surrounded by the rest of the noise spectrum of the laser. However, due to the finite resolution of our measuring devices, we can not isolate noise terms at discrete frequencies, v_n . Instead, we measure the total power (proportional to $S_{f,Laser}^2$) in a frequency bin of width, Δv , neighboring v_n .^{43,44} The ratio of the power per bin to the width of the bin yields the average power detected per one Hz bandwidth. The square root of this average power yields the spectral density of frequency noise, in $\text{Hz}/\text{Hz}^{1/2}$, as shown in Equation 3.4.

$$S_{f,Laser}(v_n) \text{ in } \frac{\text{Hz}}{\sqrt{\text{Hz}}} = \sqrt{\frac{\sum_{v'_n=v_n-\Delta v/2}^{v_n+\Delta v/2} (S_{f,Laser}(v'_n) \text{ in Hz})^2}{\Delta v \text{ in Hz}}} \quad (3.4)$$

The spectral density of frequency noise can be thought of as the average frequency noise occurring in a 1 Hz bandwidth neighboring v_n . Throughout this thesis, I consider discrete noise signals, $S_{f,Laser}(v_n)$ in Hz, when discussing theoretical relations, but discuss actual noise measurements using the spectral density of frequency noise, $S_{f,Laser}(v_n)$ in $\text{Hz}/\text{Hz}^{1/2}$.

Similarly, the spectral density of phase noise, $S_{\phi,Laser}$, spectral density of voltage noise, S_V , and spectral density of amplitude noise, $S_{A,Laser}$, are related to their discrete noise amplitudes through relations like Equation 3.4 and measured in units of $\text{Rad}/\text{Hz}^{1/2}$, $\text{V}/\text{Hz}^{1/2}$, and $1/\text{Hz}^{1/2}$, respectively. The spectral density of voltage and amplitude noise will be introduced later in the thesis.

3.2 Frequency Control Theory (Time Domain Analysis)

Laser frequency stabilization compares the instantaneous frequency output of the laser, $v_{\text{Laser}}(t)$, with a frequency reference, ideally of frequency $v_{\text{REF}}(t) = v_0$, to detect the noise frequency oscillations, $S_{f,\text{Laser}}(v_n)$ of Equation 3.2. This noise is amplified and fed back negatively to either the laser resonator or a phase modulator placed in the output path of the laser, to cancel the original noise of the laser, $S_{f,\text{Laser}}(v_n)$. The steady-state control loop established can be represented as shown in Figure 3.2.

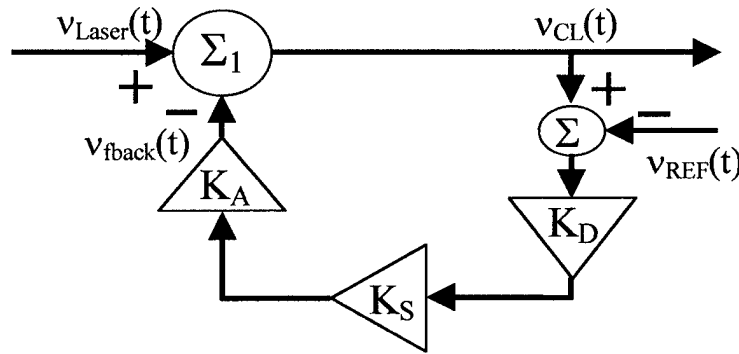


Figure 3.2. Frequency noise control loop (time domain).

The feedback noise signal, $v_{\text{fb}}(t)$ is subtracted from the original frequency output of the laser, $v_{\text{Laser}}(t)$, in the optical frequency summer, Σ_1 (the laser resonator or a phase modulator placed in the output beam path), to yield the instantaneous closed loop output frequency, $v_{\text{CL}}(t)$. The feedback noise signal is obtained by optically subtracting $v_{\text{REF}}(t)$ from $v_{\text{CL}}(t)$, and converting the resulting optical error signal, $S_{f,\text{Laser}}(v_n)$, to a voltage signal in the discriminator with transfer function $K_D(v_n)$, of units V/Hz. This voltage signal is amplified in the servo with transfer function $K_S(v_n)$, of units V/V, and sent to the frequency actuator which converts the signal back to an optical signal, $v_{\text{fb}}(t)$, with transfer function $K_A(v_n)$, of units Hz/V.

To obtain a better understanding of the control loop, I will trace the loop clockwise beginning with the unstabilized frequency of the laser, $\nu_{\text{Laser}}(t)$. Assume $S_{f,\text{Laser}}(\nu_n)$ of Equation 3.2 is real and that the complex instantaneous frequency of the electric field output of the laser can be represented as shown in Equation 3.5.

$$\nu_{\text{Laser}}(t) = \nu_0 + S_{f,\text{Laser}}(\nu_n) \cdot e^{i\omega_n t} \quad (3.5)$$

The frequency of the electric field output of the first frequency summer, Σ_1 , is equal to $\nu_{\text{CL}}(t)$, shown in Equation 3.6.

$$\nu_{\text{CL}}(t) = \nu_{\text{Laser}}(t) - \nu_{\text{fback}}(t) \quad (3.6)$$

To determine the relationship between $\nu_{\text{fback}}(t)$ and the original noise signal we assume the form of the complex feedback signal to be that of Equation 3.7.

$$\nu_{\text{fback}}(t) = S_{f,\text{fback}}(\nu_n) \cdot e^{i\omega_n t} \quad (3.7)$$

The complex amplitude of the feedback error signal is $S_{f,\text{fback}}(\nu_n)$, in Hz. Substitution of Equations 3.5 and 3.7 into 3.6 yields the explicit expression for $\nu_{\text{CL}}(t)$, which is sent to the discriminator. The discriminator compares $\nu_{\text{CL}}(t)$ to $\nu_{\text{REF}}(t)$ and converts the error signal to a voltage signal. Assume $\nu_{\text{REF}}(t)$ is constant and equal to ν_0 . The output of the discriminator is amplified in the servo and transferred back to an optical signal, $\nu_{\text{fback}}(t)$, by the actuator. Substituting Equations 3.5 and 3.7 into 3.6, and tracing the feedback signal back to the negative input terminal of Σ_1 yields the following expression.

$$\begin{aligned} S_{f,\text{fback}} \cdot e^{i\omega_n t} &= K_D(\nu_n) \cdot K_A(\nu_n) \cdot K_S(\nu_n) \cdot [S_{f,\text{Laser}} - S_{f,\text{fback}}] \cdot e^{i\omega_n t} \\ &= G_{OL}(\nu_n) \cdot [S_{f,\text{Laser}} - S_{f,\text{fback}}] \cdot e^{i\omega_n t} \end{aligned} \quad (3.8)$$

The product of the complex transfer functions of the actuator, servo and discriminator are grouped into a single complex open loop transfer function, $G_{OL}(\nu_n)$. Solving Equation 3.8 reveals the following relation between $S_{f,back}$ and $S_{f,Laser}$.

$$S_{f,back} = \left(\frac{G_{OL}(\nu_n)}{1 + G_{OL}(\nu_n)} \right) \cdot S_{f,Laser} = G_{CL}(\nu_n) \cdot S_{f,Laser} \quad (3.9)$$

$G_{CL}(\nu_n)$ is the complex closed loop transfer function and is equal to the fraction in parentheses in the first expression of Equation 3.9. By representing $G_{OL}(\nu_n)$ as shown in Equation 3.10, in terms of a magnitude and a phase, $\phi_{OL}(\nu_n)$, we can determine the magnitude and phase of $G_{CL}(\nu_n)$ as shown in Equation 3.11.

$$G_{OL}(\nu_n) = K_D(\nu_n) \cdot K_A(\nu_n) \cdot K_S(\nu_n) = |G_{OL}(\nu_n)| \cdot e^{i\phi_{OL}(\nu_n)} \quad (3.10)$$

$$G_{CL}(\nu_n) = \frac{G_{OL}(\nu_n)}{1 + G_{OL}(\nu_n)} = \frac{|G_{OL}(\nu_n)| \cdot e^{i\phi_{OL}(\nu_n)}}{1 + |G_{OL}(\nu_n)| \cdot e^{i\phi_{OL}(\nu_n)}} = |G_{CL}(\nu_n)| \cdot e^{i\phi_{CL}(\nu_n)} \quad (3.11)$$

Note that $\phi_{OL}(\nu_n)$ is the sum of the individual phase delays of the discriminator, servo, and actuator elements. After substituting Equation 3.11 and 3.9 into 3.7, and then Equations 3.7 and 3.5 into 3.6, the real portion of $v_{CL}(t)$ is found to equal Equation 3.12.

$$\text{Re}[v_{CL}(t)] = v_0 + S_{f,Laser}(\nu_n) \cdot [\cos(\omega_n t) - |G_{CL}(\nu_n)| \cdot \cos(\omega_n t + \phi_{CL}(\nu_n))] \quad (3.12)$$

Solving the second and third expressions of Equation 3.11 reveals the following relation between $\phi_{OL}(\nu_n)$ and $\phi_{CL}(\nu_n)$.

$$\phi_{CL}(\nu_n) = \arctan\left(\frac{\sin(\phi_{OL}(\nu_n))}{|G_{OL}(\nu_n)| + \cos(\phi_{OL}(\nu_n))}\right) \quad (3.13)$$

Equation 3.13 is very interesting since it suggests that $\phi_{CL}(\nu_n)$ is zero regardless of the value of $\phi_{OL}(\nu_n)$ at frequencies where $G_{OL}(\nu_n) \gg 1$. Of course, this entire derivation

assumes a steady-state loop is established and thus $\phi_{OL}(v_n)$ must remain between $\pm 180^\circ$ to avoid positive feedback. I will revisit this point later when discussing servo design.

According to Equations 3.11-3.13, the feedback signal exactly cancels the error signal at frequencies where $G_{OL}(v_n) \gg 1$, since $G_{CL}(v_n) \sim 1$ and $\phi_{CL}(v_n) \sim 0$. This is generally true at very low noise frequencies, well within the feedback loop bandwidth. However, when $G_{OL}(v_n) \ll 1$ and thus $G_{CL}(v_n) \ll 1$, Equation 3.9 suggests that $S_{f,fbck}(v_n) \ll S_{f,Laser}(v_n)$. Consequently, well outside the open loop gain bandwidth the noise remains on the output laser field, unchecked by the feedback loop.

The above analysis exhibits the goals of the loop elements. The discriminator converts the optical frequency noise signal to a voltage signal. The servo provides as much gain as possible over the chosen bandwidth of the feedback loop. Since it is usually the actuator that is the limiting factor in the loop bandwidth, the actuator must create a flat frequency response to applied voltages for as wide a bandwidth as possible.

3.3 Control Loop Elements

3.3.1 Discriminator

The control loop must discern between the correct phase and the erroneous phase output of the laser. Though there are several techniques of accomplishing this task,^{25,45} most of the stabilization experiments of this thesis employ the Pound-Drever-Hall (PDH) FM sideband-locking technique.²⁵ The discriminator is arguably the most important element of the feedback loop since its frequency stability and sensitivity set the limit to which the laser's frequency can be stabilized. Since the frequency discriminator is the chief difference between all of the stabilization experiments of this thesis, it will be discussed in detail in later chapters for each of the individual experiments.

For now we need only understand that the discriminator compares the instantaneous frequency of the output laser field to a reference frequency and outputs a voltage signal, in an external circuit, proportional to their difference. This process generates a spectral density of voltage noise, $S_{V,D}(v_n)$, in units of $V/Hz^{1/2}$. The largest noise source of the discriminator is usually the shot noise of the photodetector used in the PDH technique, as will be discussed for two particular cases in Chapters 4 and 5.

The voltage signal leaving the discriminator is amplified by the servo and sent to the frequency actuator. Since the servo is much more complex than the actuator I will discuss the actuator now and leave the servo for last.

3.3.2 Actuator

The voltage output of the servo passes to the actuator to be converted back into an optical phase oscillation and summed with the original laser output. To do this, the actuator compensates for the frequency noise by adding (negatively) a frequency signal of equal amplitude and oscillation frequency as the noise. Sample actuators are Piezo-electric Transducers (PZTs), Electro-optic modulators (EOMs), Acousto-optic modulators (AOMs), temperature controllers, and any other device used to vary the phase of the circulating field of the laser resonator or the output field. Since PZTs, EOMs, and AOMs have the fastest responses, they are most-often used for fast frequency corrections.

When placed in the beam path, an EOM can be used to modulate the output phase of the electric field. The modulation of the applied voltage creates a modulation of the transverse electric field applied to the EOM's crystal. This causes a modulation of the index of refraction encountered by the incident field and hence a modulation of the output phase of the field. The output phase of the electric field is the sum of the incident phase

and the EOM-induced phase as depicted by Σ_1 of Figure 3.2. Advantages of using an EOM include a large feedback bandwidth and added versatility, since it can be placed within the laser resonator or in the path of the laser output, assuming the circulating or output powers are less than the damage threshold of the EOM. Consequently, the EOM is usually used for the stabilization of low power lasers (less than 5 W output) and placed outside the laser cavity in the path of the output beam.

On the other hand, a PZT can be used in high power laser applications since it is not an intracavity element. It is mounted behind a cavity mirror and is used to sweep, or “dither,” the mirror position and thus the cavity length about its equilibrium position. The disadvantage of using a PZT is the low bandwidth. While an EOM bandwidth can be as large as several MHz, a PZT has resonances that limit its bandwidth to 10’s of kHz. These resonances cause a nonlinear response and hence need to be avoided by our linear feedback loop. Thus, for high power applications, the bandwidth of the feedback loop is limited by the bandwidth of the actuator, which is limited by the resonances of the PZT.

3.3.3 Servo

The servo amplifies the voltage signal produced by the frequency discriminator over as wide a range of frequencies as possible so that $G_{CL}(v_n) \sim 1$ and $\phi_{CL}(v_n) \sim 0$ in Equation 3.12. Usually the servo is the final loop element to be optimized. At this point the discriminator and actuator have been chosen and their complex transfer functions, $K_D(v_n)$ and $K_A(v_n)$, are known. The key considerations in designing the servo to produce a stable feedback loop are the Unity-Gain-Bandwidth (UGBW), and the phase margin of $G_{OL}(v_n)$. The UGBW is defined as the range of frequencies up to and including v_{UG} , the highest frequency encountering an open loop gain of one (i.e. $|G_{OL}(v_{UG})| = 1$). The phase

margin is defined as the difference between the phase delay of the open loop transfer function occurring at ν_{UG} (i.e. $\phi_{OL}(\nu_{UG})$) and -180° . To see the importance of these parameters we analyze the relationship between $G_{CL}(\nu_n)$ and $G_{OL}(\nu_n)$, of Equations 3.11 and 3.13. The denominator of the second relation shown in Equation 3.11 approaches zero if $\phi_{OL}(\nu_{UG})$ equals -180° (corresponding to zero phase margin). Such a case causes a spiking of the feedback signal to a magnitude much greater than the original noise signal and forces the frequency of the laser to oscillate without bound. The laser output frequency is unable to remain locked to the reference frequency and the system is labeled unstable. To achieve a stable lock we monitor the phase margin at ν_{UG} to insure we avoid the undesirable oscillation described above. Most electronics texts suggest that a phase margin of 45° is required for unconditional stability of the overall loop.⁴⁶ Added to this stability criterion, we must avoid positive feedback for all noise frequencies encountering an open loop gain greater than one. I have derived the loop equations using a minus sign in front of the feedback signal, $\nu_{f,back}(t)$, to account for the negative feedback. Thus, to insure stability, $\phi_{CL}(\nu_n)$ must be between zero and $\pm 180^\circ$ through ν_{UG} . Equation 3.13 suggests that at noise frequencies where $|G_{OL}(\nu_n)| \gg 1$, the argument of the arc tangent is very small and $\phi_{CL}(\nu_n)$ remains near zero regardless of the value of $\phi_{OL}(\nu_n)$. As $|G_{OL}(\nu_n)|$ approaches one, $\phi_{CL}(\nu_n)$ approaches $\phi_{OL}(\nu_n)$. This causes an added reduction in the effectiveness of the feedback loops of this thesis at frequencies near ν_{UG} since the open loop gain is small and the feedback signal is out of phase with the original noise signal.

To optimize the noise suppression capabilities of the feedback loop while maintaining loop stability, we want $|G_{OL}(\nu_n)| \gg 1$ over the pre-determined bandwidth of

the loop, usually limited by the actuator bandwidth or the presence of actuator resonances, as is the case for high power applications using PZT's. To create a stable loop, we measure $K_D(v_n)$ and $K_A(v_n)$ and design a servo with as much gain as possible out to v_{UG} , while avoiding positive feedback and producing a phase margin of at least 45° .

The servos constructed to supplement the work of this thesis consisted of a series of operational amplifiers configured as integrators. Figure 3.3 displays the servo design with input and feedback resistors ($R1$, $R2$, $R3$) and capacitors ($C1$, $C2$, $C3$). Stages 2 and 3 are configured as integrators and Stage 1 is used to provide DC gain adjustment.

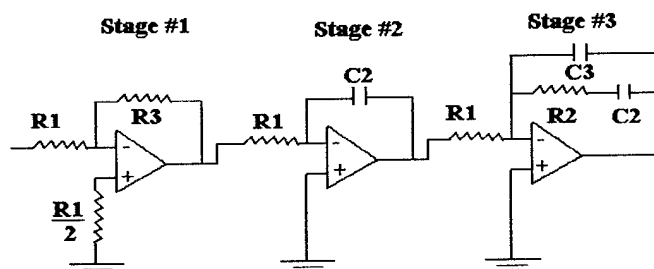


Figure 3.3. Servo design.

The corner frequency of one stage is set at or just below v_{UG} to insure at least a 45° phase margin.⁴⁶ Figure 3.4 displays sample gain (in dB) and phase (in degrees) versus frequency plots when incorporating the servo design of Figure 3.3 into the feedback loop.

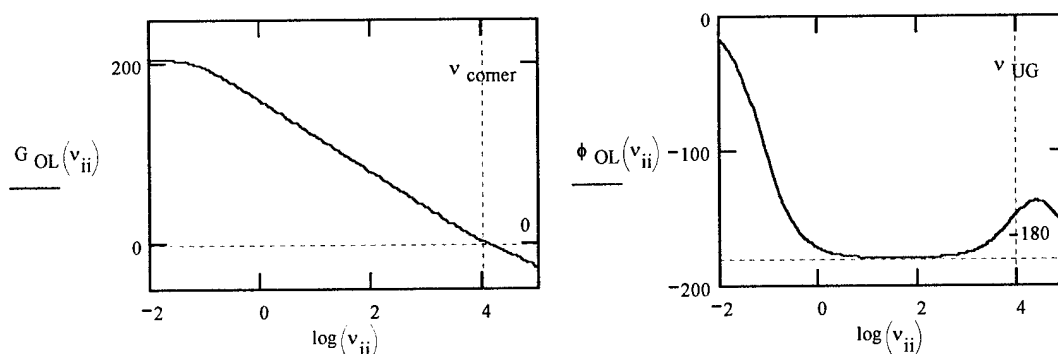


Figure 3.4. Gain and phase of open loop transfer function.

Where v_{ii} is a dummy variable equal to v_n , and v_{corner} is set to be $\sim v_{UG}$. Figure 3.4 shows that the DC gain is nearly 208 dB. The two integrators yield a gain versus frequency slope of -12 dB/Octave which “rolls out” to -6 dB/Octave at the corner frequency, v_{corner} . At this point, the phase plot shows that the phase increases with respect to frequency, creating a phase margin of nearly 45° . The phase plot also shows that the use of two integrators yields an open loop phase delay, $\phi_{OL}(v_n)$, that ranges from 0° to nearly -180° over a large portion of the unity gain bandwidth of the servo. This originally concerned me. However, as I have pointed out, Equation 3.13 shows that this phase error is only critical at noise frequencies near the open loop unity gain frequency, v_{UG} . Thus, the servo design of Figure 3.3 creates a large DC gain at the expense of a reduced feedback efficiency near v_{UG} .

Using plots similar to Figure 3.4, one can account for the measured values of $K_A(v_n)$, $K_D(v_n)$, and the desired v_{UG} , and optimize the integrators of the servo to create a stable feedback loop. The DC voltage gain of Stage 1 is used to fine-tune v_{UG} after the loop has established a stable frequency lock between the laser and reference.

As one might expect, the voltage noise of this servo, $S_{v,s}(v_n)$, is primarily caused by the Johnson noise of the various resistors.

3.4 Frequency Control Theory (Frequency Domain Analysis)

To predict the performance of the feedback loop in eliminating the frequency noise of the laser one can determine the closed loop spectral density of frequency noise of the laser, $S_{f,CL}$, by analyzing the frequency noise control loop in the frequency domain. Before doing so, assume now that the instantaneous frequency of the reference varies

about the desired center frequency, ν_0 , with a spectral density of frequency noise

$S_{f,REF}(\nu_n)$, as shown in Equation 3.14.

$$\nu_{REF}(t) = \nu_0 + S_{f,REF}(\nu_n) \cdot e^{i\omega_n t} \quad (3.14)$$

Figure 3.5 displays a model of the frequency noise control loop, similar to that proposed by Day,³⁰ but with the addition of the frequency noise of the reference, $S_{f,REF}(\nu_n)$.

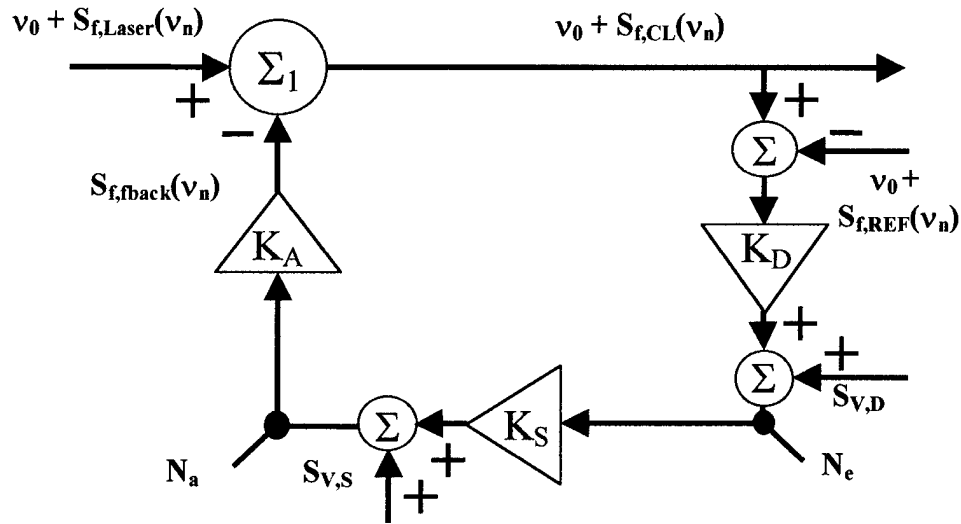


Figure 3.5. Frequency noise control loop (frequency domain).

Again, K_D , K_S , and K_A represent the transfer functions of the discriminator, servo and actuator. Also, $S_{f,Laser}$ and $S_{f,CL}$ are the spectral density of frequency noise of the original laser (open loop) and the stabilized laser (closed loop), respectively. $S_{v,D}$ is the voltage noise of the discriminator and $S_{v,S}$ is the voltage noise of the servo. I have removed their frequency dependence since they are generally dominated by white noise. N_e (error point) and N_a (actuator point) refer to the voltage signals measured at the entrance and exit of the servo, respectively. To determine the usefulness of the N_e and N_a point measurements in determining $S_{f,Laser}$ and $S_{f,CL}$ we must trace the signal clockwise through

the loop (as done by Day in Ref. 30 for the case without $S_{f,REF}$). Equation 3.15 displays the resulting closed loop spectral density of noise of the laser.

$$S_{f,CL}(\nu_n) = \left\{ \frac{\sqrt{(S_{f,Laser}(\nu_n))^2 + (K_A(\nu_n) \cdot K_S(\nu_n) \cdot S_{V,D})^2 + (K_A(\nu_n) \cdot S_{V,S})^2}}{|1 + G_{OL}(\nu_n)|} + S_{f,REF}(\nu_n) \cdot G_{CL}(\nu_n) \right\} \quad (3.15)$$

Well within the feedback loop bandwidth, where $K_S(\nu_n) \gg 1$, $G_{OL}(\nu_n) \gg 1$, and thus $G_{CL}(\nu_n) \sim 1$, Equation 3.15 simplifies to Equation 3.16.

$$S_{f,CL}(\nu_n) \approx \frac{S_{V,D}}{K_D(\nu_n)} + S_{f,REF}(\nu_n) \quad (3.16)$$

Equation 3.16 shows that the stability of the frequency reference sets a lower limit on the achievable frequency stability of the laser. This limit distinguishes the results of relative and absolute frequency stabilization (in which $S_{f,REF}(\nu_n)$ is equal to zero). In addition to the noise of the frequency reference, the voltage noise of the discriminator, $S_{V,D}$, determines the minimal closed loop spectral density of frequency noise of the laser, $S_{f,CL}$. Also, in this regime, the N_e point signal is given by Equation 3.17.

$$N_e(\nu_n) = K_D(\nu_n) \cdot (S_{f,CL}(\nu_n) - S_{f,REF}(\nu_n)) \approx S_{V,D} \quad (3.17)$$

Equation 3.17 shows that well within the loop bandwidth the added frequency noise of the reference is not visible at $N_e(\nu_n)$. Comparison of Equations 3.17 and 3.16 reveals that $S_{f,CL}$ can be determined from $N_e(\nu_n)$ as shown in Equation 3.18.

$$S_{f,CL}(\nu_n) \approx \frac{N_e(\nu_n)}{K_D(\nu_n)} + S_{f,REF}(\nu_n) \quad \nu_n < \nu_{UG} \quad (3.18)$$

By solving for $N_a(\nu_n)$ in this regime one finds the following relation.

$$N_a(\nu_n) \approx \frac{S_{f,Laser}(\nu_n) - S_{f,REF}(\nu_n)}{K_A(\nu_n)} \quad \nu_n < \nu_{UG} \quad (3.19)$$

Thus, the frequency noise of the reference is present at the N_a point and unless $S_{f,REF}(\nu_n) \ll S_{f,Laser}(\nu_n)$, the use of Equation 3.19 may give an erroneous value of $S_{f,Laser}$.

Outside the loop bandwidth (where $G_{OL}(\nu_n) \ll 1$ and $G_{CL}(\nu_n) \sim 0$) the frequency noise of the reference is not added to the laser (in Equation 3.15), but is still present in the frequency discriminator.

$$N_e(\nu_n) \approx K_D(\nu_n) \cdot [S_{f,Laser}(\nu_n) - S_{f,REF}(\nu_n)] \quad \nu_n > \nu_{UG} \quad (3.20)$$

The use of Equation 3.20 yields an erroneous value for $S_{f,Laser}$ (and $S_{f,CL}$ since they are nearly equal in this regime), due to the presence of the frequency noise of the reference.

Taken together, the results of Equations 3.18-3.20 can be grouped into the following expressions relating the voltage signals measured at N_e and N_a to the open loop relative spectral density of frequency noise between the laser and the reference, $S_{f,Laser} - S_{f,REF}$, and the closed loop relative spectral density of frequency noise between the laser and the reference, $S_{f,CL} - S_{f,REF}$.

$$S_{f,Laser}(\nu_n) - S_{f,REF}(\nu_n) \approx \begin{cases} K_A(\nu_n) \cdot N_a(\nu_n) & \nu_n < \nu_{UG} \\ \frac{N_e(\nu_n)}{K_D(\nu_n)} & \nu_n > \nu_{UG} \end{cases} \quad (3.21)$$

$$S_{f,CL}(\nu_n) - S_{f,REF}(\nu_n) \approx \begin{cases} \frac{N_e(\nu_n)}{K_D(\nu_n)} & \text{All } \nu_n \end{cases} \quad (3.22)$$

3.5 Summary

In this chapter, I reviewed the definition of the spectral density of frequency noise of a laser and introduced the frequency noise control loop (in the time domain and the frequency domain) established in the stabilization efforts to eliminate this noise.

I introduced two of the feedback control loop elements – the actuator and the servo – since these elements are nearly identical for all of the experiments that I will discuss in the following chapters. I used the results of the time domain control loop analysis to explain the trade-off between low frequency open loop gain and reduced feedback efficiency at noise frequencies near the open loop unity gain point, for the servos used in this thesis.

I altered the frequency domain noise control loop of Day to include the relative frequency stability of the reference. I used this control loop to determine the explicit relationship between the voltage signals measured at the entrance (N_e) and exit (N_a) of the servo and the open and closed loop relative spectral density of frequency noise between the laser and the reference. Although this simple control loop does not provide a complete description of the frequency stabilization experiments of this thesis, it serves as a good starting point in establishing the more complex control loops which do accurately model these experiments.

The control loop analysis suggests that other than the relative frequency stability of the reference, the voltage noise of the discriminator is the chief limiting factor in the frequency stabilization effort (see Equation 3.16). Since the discriminator is the chief difference between all of the experiments of this research effort, and arguably the most important feedback loop element, I will discuss it separately for each of the particular experiments considered in this thesis.

CHAPTER 4. Locking a Laser to a Fabry-Perot

In this chapter, I review the theory of stabilizing the frequency of a laser to the resonant frequency of a Fabry-Perot using the PDH technique. The previous derivation, by Day, split the incident laser field into discrete components (the carrier, the noise sideband, and the two modulation sidebands) and multiplied them by the reflection coefficient of the Fabry-Perot to obtain an explicit expression for the reflected field and then the error signal.³⁰ To account for the length (and hence frequency) fluctuations of the Fabry-Perot one can expand the effective control loop presented by Day to account for the noise of the Fabry-Perot (as I have done in Figure 3.5). To actually prove Figure 3.5 is correct one must derive the PDH error signal while accounting for the Fabry-Perot length fluctuations. I attempted to expand the derivation of Day to include the Fabry-Perot noise contributions, but the resulting equations were too complex to solve.

Below, I derive the PDH error signal in a new manner, using the damped, driven wave equation to describe the circulating field of the Fabry-Perot. This derivation yields the same results as Day and various additional terms. I then alter the frequency noise control loop of Figure 3.5 to account for the parameters of this new derivation. In so doing, I set the stage for simple comparisons to be made with the complex injection-locking control loop presented in the next chapter. I briefly review the methods of achieving the minimal closed loop spectral density of noise and the usefulness of the N_e and N_a points of the control loop in determining the open and closed loop relative spectral density of frequency noise between the laser and the Fabry-Perot. I compare the results of this control loop analysis to those of Chapter 3 to determine the usefulness of Figure 3.5 in describing this process.

4.1 Derivation of Error Signal

Figure 4.1 shows a typical PDH frequency stabilization experiment used to stabilize the output frequency of an NPRO, the master laser of the injection-locking experiments.

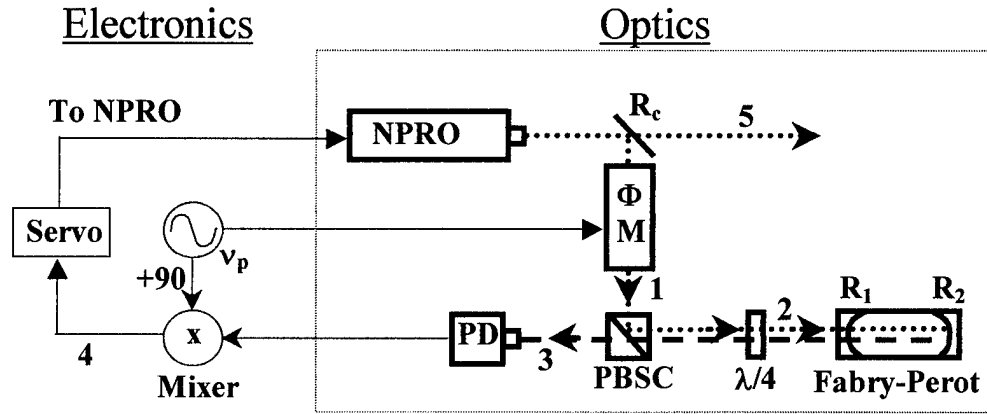


Figure 4.1. Optical Schematic of locking laser to Fabry-Perot.

A portion of the vertically polarized field from the master laser of carrier frequency ν_m is reflected by a mirror of power reflectivity R_c , and phase modulated, at a frequency ν_p and modulation index β , to yield the field at position 1. This field, shown as a dotted line, is reflected by the polarizing beam-splitter cube, PBSC, and transformed by a quarter wave plate, $\lambda/4$, into the circularly polarized field incident on the Fabry-Perot resonator at position 2. The reflected field, shown as a dashed line, is converted into a horizontally polarized field by the $\lambda/4$ plate, passes through the PBSC, and is incident on the photodiode, PD, at position 3.

If we consider the master laser phase noise, $S_{\phi,m}$, at a particular noise frequency, ν_n , the complex field incident on the resonator at position 2, E_{inc} , is shown in Equation 4.1. Note that this equation is nearly identical to Equation 3.1 (with the addition of phase

modulation sidebands at ω_p), but I have changed from the generic symbols ω_0 , E_0 , and $S_{\phi, \text{Laser}}$ to symbols with subscripts m (ω_m , E_m , and $S_{\phi, m}$) referring to the master laser.

$$\tilde{E}_{inc} = \sqrt{R_c} \cdot E_m \cdot e^{i\omega_m t} \cdot e^{iS_{\phi, m}(\nu_n)\sin(\omega_n t)} \cdot e^{i\beta \sin(\omega_p t)} \quad (4.1)$$

The last exponential term in this expression can be simplified by expanding the sine term as shown in Equation 4.2, using the Bessel function expansion shown in Equation 4.3 and using the identity shown in Equation 4.4 to the expression shown in Equation 4.5. Also, β is assumed to be small enough that only zero and first order terms are non-negligible.

$$\sin(\omega_p t) = \frac{e^{i\omega_p t} - e^{-i\omega_p t}}{2i} \quad (4.2)$$

$$e^{(x/2)^{(t-1/t)}} = \sum_{k=-\infty}^{+\infty} J_k(x) \cdot t^k \quad (4.3)$$

$$J_{-k}(x) = (-1)^k \cdot J_k(x) \quad (4.4)$$

$$\begin{aligned} \tilde{E}_{inc} &= \sqrt{R_c} \cdot E_m \cdot e^{i\omega_m t} \cdot e^{iS_{\phi, m}(\nu_n)\sin(\omega_n t)} \cdot [J_0(\beta) + 2iJ_1(\beta) \cdot \sin(\omega_p t)] \\ &= \tilde{E}_{inc}(\omega_m) + \tilde{E}_{inc}(\omega_m \pm \omega_p) \end{aligned} \quad (4.5)$$

The last expression of Equation 4.5 splits the incident field into the spectral fraction neighboring the carrier frequency, ω_m , and the fraction near the sidebands at $\omega_m \pm \omega_p$.

The Fabry-Perot consists of two mirrors with power reflectivities R_1 and R_2 , shown in Figure 4.1, and a medium of length L and absorption coefficient α_0 , in units of cm^{-1} . The nearest longitudinal resonant frequency to the carrier frequency of the incident laser is ν_c . The circulating field of the Fabry-Perot experiences a total energy decay rate, γ_c , equal to the sum of the decay rates due to absorption, γ_0 , and transmission through the

input/output coupler (mirror R_1), γ_e , and mirror R_2 , γ_2 . These decay rates are defined below in terms of the circulating field round trip time, T , and the speed of light, c .²¹

$$\gamma_c = \gamma_0 + \gamma_e + \gamma_2 \quad (4.6)$$

$$\gamma_0 = 2\alpha_0 c \quad (4.7)$$

$$\gamma_e = \frac{1}{T} \cdot \ln\left(\frac{1}{R_1}\right) \quad (4.8)$$

$$\gamma_2 = \frac{1}{T} \cdot \ln\left(\frac{1}{R_2}\right) \quad (4.9)$$

$$T = \frac{2L}{c} = \frac{1}{FSR} \quad (4.10)$$

Assume the incident field is mode matched to a longitudinal mode of the cavity, and the resonator is impedance matched (i.e. $\gamma_e = \gamma_0 + \gamma_2$). The carrier portion of the incident field, $E_{inc}(\omega_m)$ of Equation 4.5, is perfectly coupled into the resonator while the sidebands, $E_{inc}(\omega_m \pm \omega_p)$, are well outside the cavity passband and are fully reflected.

Based on the discussion of Siegman, one can compare the damped, driven wave equation for the circulating field of the Fabry-Perot resonator to a similar expression obtained when analyzing an equivalent RLC circuit, to derive the following expression for the circulating field, E_c .²¹

$$\frac{d^2 \tilde{E}_c}{dt^2} + \gamma_c \cdot \frac{d \tilde{E}_c}{dt} + (\omega_c)^2 \cdot \tilde{E}_c = \sqrt{\frac{8 \cdot \gamma_e}{\epsilon \cdot V_c}} \cdot \frac{d}{dt} \left[\tilde{E}_{inc}(\omega_m) \right] \quad (4.11)$$

Where ϵ is the permittivity of free space and V_c is the total spatial volume of the circulating field. This expression assumes that, in the steady state, all of the carrier

portion of the field is coupled into the resonator and thus the reflection coefficient of the carrier field is equal to zero.

The incident field is represented as the product of a real field amplitude, E_{inc} , a phase term oscillating at ω_m , and a time dependent phase noise term $\phi_m(t)$, shown in Equation 4.12. A similar assumed dependence for the circulating field is shown in Equation 4.13 with a phase term oscillating at ω_m and time-dependent phase term, $\phi_c(t)$.

$$\tilde{E}_{inc}(\omega_m) = \sqrt{R_c} \cdot J_0(\beta) \cdot E_m \cdot e^{i\omega_m t} \cdot e^{iS_{\phi,m}(v_n)\sin(\omega_m t)} = E_{inc} \cdot e^{i\omega_m t} \cdot e^{i\phi_m(t)} \quad (4.12)$$

$$\tilde{E}_c = E_c \cdot e^{i\omega_m t} \cdot e^{i\phi_c(t)} \quad (4.13)$$

By substituting Equations 4.12 and 4.13 into Equation 4.11, making the slowly varying envelope approximation, and equating the real and imaginary portions of the resulting equation, we obtain the following expressions.

$$\frac{dE_c}{dt} + \frac{\gamma_c}{2} \cdot E_c = \sqrt{\frac{2 \cdot \gamma_e}{\epsilon \cdot V_c}} \cdot E_{inc} \cdot \cos[\phi_c - \phi_m] \quad (4.14)$$

$$\frac{d\phi_c}{dt} + \omega_m - \omega_c = -\sqrt{\frac{2 \cdot \gamma_e}{\epsilon \cdot V_c}} \cdot \frac{E_{inc}}{E_c} \cdot \sin[\phi_c - \phi_m] \quad (4.15)$$

To determine the reflected field amplitude and phase we note that the energy of the circulating field, U_c , is given by Equation 4.16.²¹

$$U_c = \frac{\epsilon \cdot V_c}{2} \cdot E_c^2 \quad (4.16)$$

Equation 4.17 relates the energy lost by the circulating field in transmission through mirror R_1 to the leakage field intensity, I_r .

$$\gamma_e \cdot U_c = I_r = E_r^2 \quad (4.17)$$

Substitution of Equations 4.16 and 4.17 yields an expression relating E_r and E_c .

Substitution of this expression into Equations 4.14 and 4.15 yields the following expression for the leakage field amplitude, E_r , and phase, ϕ_r , just outside the mirror R_1 traveling to the left (the dashed line in Figure 4.1). Assume $\phi_r = \phi_c$.

$$\frac{dE_r}{dt} + \frac{\gamma_c}{2} \cdot E_r = \gamma_e \cdot E_{inc} \cdot \cos[\phi_r - \phi_m] \quad (4.18)$$

$$\frac{d\phi_r}{dt} + \omega_m - \omega_c = -\gamma_e \cdot \frac{E_{inc}}{E_r} \cdot \sin[\phi_r - \phi_m] \quad (4.19)$$

To solve these expressions at a given noise frequency, ν_n , assume that E_{inc} , E_r , ϕ_m , ϕ_r , and ω_c oscillate with small perturbations about their steady state values (represented with subscript zero) as shown below.⁴⁷

$$E_{inc} = E_{inc,0} + \delta E_{inc} \cdot e^{i\omega_n t} = E_{inc,0} \cdot (1 + S_{A,m}(\nu_n) \cdot e^{i\omega_n t}) \quad (4.20)$$

$$E_r = E_{r,0} + \delta E_r \cdot e^{i\omega_n t} = E_{r,0} \cdot (1 + S_{A,r}(\nu_n) \cdot e^{i\omega_n t}) \quad (4.21)$$

$$\phi_m = \phi_{m,0} + \delta \phi_m \cdot e^{i\omega_n t} = \phi_{m,0} + S_{\phi,m}(\nu_n) \cdot e^{i\omega_n t} \quad (4.22)$$

$$\phi_r = \phi_{r,0} + \delta \phi_r \cdot e^{i\omega_n t} = \phi_{r,0} + S_{\phi,r}(\nu_n) \cdot e^{i\omega_n t} \quad (4.23)$$

$$\omega_c = \omega_{c,0} + \delta \omega_c \cdot e^{i\omega_n t} = \omega_{c,0} + i \cdot \omega_n \cdot S_{\phi,c}(\nu_n) \cdot e^{i\omega_n t} \quad (4.24)$$

Let $S_{\phi,m}$ and $S_{\phi,r}$ represent the spectral density of phase noise of the incident field and the leakage field and $S_{A,m}$ and $S_{A,r}$ represent their spectral density of amplitude noise, respectively. The inclusion of the amplitude modulation (AM) noise terms, $S_{A,m}$ and $S_{A,r}$, is necessary to reveal the various AM to FM (frequency modulation) coupling terms. The phase noise of the resonant frequency of the cavity, $S_{\phi,c}$, has been introduced in Equation 4.24. Below, the product $i\omega_n$ is simplified as the variable: s .

By combining the steady state solutions of Equations 4.18 and 4.19 we obtain the single expression for the steady state phase delay of the reflected field with respect to the incident field, $\Delta\phi_{ss}$, shown in Equation 4.25. I converted ω_m , ω_c , and γ_c to their respective frequencies ν_m , ν_c , and $\delta\nu_c$, in Hz, by dividing by 2π , to obtain the last expression.

$$\Delta\phi_{ss} = \phi_{r,0} - \phi_{m,0} = \arctan\left[\frac{\omega_m - \omega_c}{\gamma_c/2}\right] = \arctan\left[\frac{\nu_m - \nu_c}{\delta\nu_c/2}\right] \quad (4.25)$$

Note that the photon lifetime of the cavity, τ_p , is defined as shown in Equation 4.26.⁴⁸

$$\tau_p = \frac{1}{\gamma_c/2} = \frac{1}{2 \cdot \pi \cdot (\delta\nu_c/2)} \quad (4.26)$$

Thus, the phase delay of Equation 4.25 is simply the product of the discrete radial frequency difference between ω_m and ω_c and the time the field circulates in the cavity, τ_p .

This phase delay, plotted in Figure 4.2, is the source of the PDH error signal.

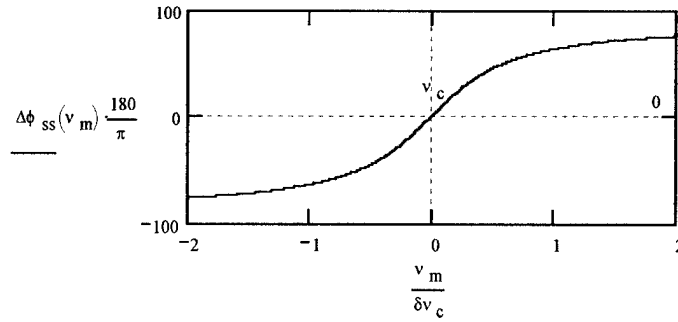


Figure 4.2. Steady state phase delay.

By substituting the perturbations shown in the first expressions of Equations 4.20-4.24 into Equations 4.18 and 4.19, performing a Taylor series expansion of cosine and sine terms about their steady state arguments, and keeping only terms of zero and first order in the perturbation we obtain the following equations. The second expressions of

Equations 4.20-4.24 have been used to simplify these equations in terms of spectral densities of amplitude and phase noise. The common denominator, D , is defined below.

$$D = \left(s + \frac{\gamma_c}{2} \right)^2 + (\omega_m - \omega_c)^2 \quad (4.27)$$

$$S_{\phi,r} = \left[\frac{s \cdot \left(s + \frac{\gamma_c}{2} \right)}{D} \right] \cdot S_{\phi,c} + \left[\frac{\left(\frac{\gamma_c}{2} \right) \cdot \left(s + \frac{\gamma_c}{2} \right) + (\omega_m - \omega_c)^2}{D} \right] \cdot S_{\phi,m} + \left[\frac{s \cdot (\omega_m - \omega_c)}{D} \right] \cdot S_{A,m} \quad (4.28)$$

$$S_{A,r} = \left[\frac{s \cdot (\omega_m - \omega_c)}{D} \right] \cdot (S_{\phi,c} - S_{\phi,m}) + \left[\frac{\left(\frac{\gamma_c}{2} \right) \cdot \left(s + \frac{\gamma_c}{2} \right) + (\omega_m - \omega_c)^2}{D} \right] \cdot S_{A,m} \quad (4.29)$$

These equations yield much information about the AM to FM coupling between the incident and reflected fields and will be discussed in Section 4.2. At present we are interested in the PDH error signal obtained in the experiment shown in Figure 4.1. By assuming $\omega_m = \omega_c$ and the AM of the incident field ($S_{A,m}$) is negligible, Equation 4.28 simplifies to Equation 4.30 which is simplified in terms of the variable κ , defined in Equation 4.31.

$$S_{\phi,r} = \frac{s}{\left(s + \frac{\gamma_c}{2} \right)} \cdot S_{\phi,c} + \frac{\frac{\gamma_c}{2}}{\left(s + \frac{\gamma_c}{2} \right)} \cdot S_{\phi,m} = \left[\frac{i \cdot \kappa}{1 + i \cdot \kappa} \right] \cdot S_{\phi,c} + \left[\frac{1}{1 + i \cdot \kappa} \right] \cdot S_{\phi,m} \quad (4.30)$$

$$\kappa = \frac{\omega_n}{\frac{\gamma_c}{2}} = \frac{\nu_n}{\frac{\delta \nu_c}{2}} \quad (4.31)$$

Equation 4.30 can be rewritten in terms of frequency noise by multiplying both sides by ν_n and switching from phase noise terms to frequency noise terms using Equation 3.3.

$$S_{f,r} = \left[\frac{i \cdot \kappa}{1 + i \cdot \kappa} \right] \cdot S_{f,c} + \left[\frac{1}{1 + i \cdot \kappa} \right] \cdot S_{f,m} = T_C(v_n) \cdot S_{f,c} + T_L(v_n) \cdot S_{f,m} \quad (4.32)$$

I have grouped the bracketed terms into the frequency noise transfer functions of the cavity length fluctuations, $T_C(v_n)$, and the incident laser field, $T_L(v_n)$, onto the circulating field and hence leakage field from the resonator. Note that the transfer function of a high pass filter of corner frequency, v_{corner} , defined as $T_{HIGH}(v_n, v_{corner})$, is shown in Equation 4.33 and that of a low pass filter of corner frequency, v_{corner} , defined as $T_{LOW}(v_n, v_{corner})$ is shown in Equation 4.34.

$$T_{HIGH}(v_n, v_{corner}) = \left(\frac{i \cdot \frac{v_n}{v_{corner}}}{1 + i \cdot \frac{v_n}{v_{corner}}} \right) \quad (4.33)$$

$$T_{LOW}(v_n, v_{corner}) = \left(\frac{1}{1 + i \cdot \frac{v_n}{v_{corner}}} \right) \quad (4.34)$$

Comparison of Equation 4.32 with 4.33 and 4.34 reveals that $T_C(v_n)$ is a high pass filter of corner frequency $\delta v_c/2$ (i.e. $T_C(v_n) = T_{HIGH}(v_n, \delta v_c/2)$), and $T_L(v_n)$ is a low pass filter of corner frequency $\delta v_c/2$ (i.e. $T_L(v_n) = T_{LOW}(v_n, \delta v_c/2)$), as shown in Figure 4.3.

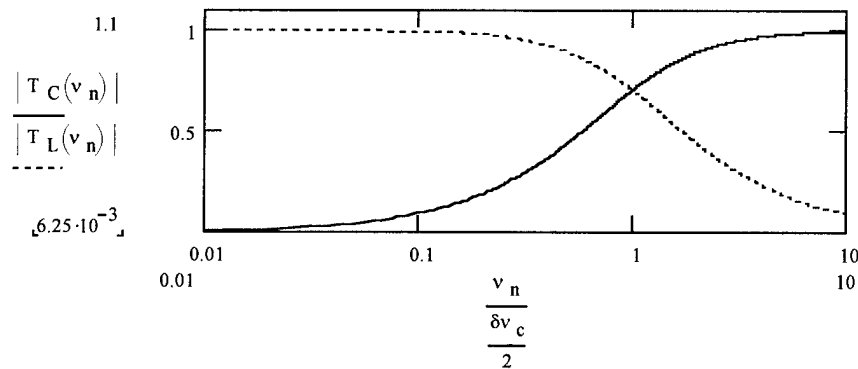


Figure 4.3. Frequency noise transfer functions.

To understand these transfer functions, we begin by noting that the incident field circulates within the resonator for a time interval equal to τ_p . The phase fluctuations of the incident field are transferred directly onto the circulating field for low ν_n , but as ν_n increases, a point is reached at which the field oscillates too fast for the circulating field to follow these fluctuations instantaneously. The high frequency phase fluctuations are thus averaged (or integrated) over the time interval τ_p , yielding the low pass transfer function, $T_{\text{LOW}}(\nu_n, \delta\nu_c/2)$, with corner frequency $\delta\nu_c/2$. On the other hand, the cavity fluctuations are not on the incident field and only influence the field for the time interval τ_p . Only when ν_n is sufficiently high, such that the circulating field is present through the entire phase fluctuation of the cavity, does the field pick-up this phase noise. This results in the high pass filter, $T_{\text{HIGH}}(\nu_n, \delta\nu_c/2)$, of corner frequency $\delta\nu_c/2$.

The leakage field portion of the reflected field is shown in Equation 4.35.

$$\tilde{E}_r(\omega_m) = E_{r,0} \cdot e^{i\omega_m t} \cdot e^{i\text{Re}(-iS_{\phi,r} \cdot e^{i\omega_n t})} = \sqrt{R_c} \cdot J_0(\beta) \cdot E_m \cdot e^{i\omega_m t} \cdot e^{i\text{Re}(-iS_{\phi,r} \cdot e^{i\omega_n t})} \quad (4.35)$$

The second expression equates $E_{r,0}$ to $E_{\text{inc},0}$ (from the steady-state solution of Equation 4.18 for the impedance matched case with $\omega_m = \omega_c$), which is equal to the arguments of Equation 4.12. However, the resonator is only perfectly impedance matched on resonance when $\omega_m = \omega_c$ and the phase delay of the circulating field with respect to the incident field, $\Delta\phi(\nu_n)$ (defined in Equation 4.36), is zero.

$$\Delta\phi(\nu_n) = \text{Re}\left[-i \cdot (S_{\phi,r} - S_{\phi,m}) \cdot e^{i\omega_n t}\right] = \text{Re}\left[\left[\frac{\kappa}{1 + i \cdot \kappa}\right] \cdot (S_{\phi,c} - S_{\phi,m}) \cdot e^{i\omega_n t}\right] \quad (4.36)$$

The second expression is obtained by substituting Equation 4.30 in for $S_{\phi,r}$. It is interesting to note that Figure 4.2 showed that the phase noise transfer functions of the

Fabry-Perot and incident field differed, primarily because the incident phase noise was already present on the field before it interacted with the cavity. The subtraction of the incident phase noise, $S_{\phi,m}$, yields the phase delay, $\Delta\phi(\nu_n)$, of the circulating field with respect to the incident field. Equation 4.36 shows that this phase delay is equally susceptible to $S_{\phi,m}$ and $S_{\phi,c}$. Note that this is the same conclusion drawn when considering the phase delay, $\Delta\phi_{ss}$ of Equation 4.25, when considering the discrete frequency error case.

The assumption that the total reflected field be zero, suggests that the leakage field perfectly destructively interferes with the portion of the incident field originally reflected from the input coupler of the cavity. To insure this assumption holds true, I define the reflected carrier field as shown in Equation 4.37.

$$\tilde{E}_r(\omega_m) = \sqrt{R_c} \cdot J_0(\beta) \cdot E_m \cdot e^{i\omega_m t} \cdot e^{i \operatorname{Re}(-iS_{\phi,m} \cdot e^{i\omega_n t})} \cdot (1 - e^{i\Delta\phi(\nu_n)}) \quad (4.37)$$

The second term in parenthesis represents the leakage field of Equation 4.35, with the phase noise term, $S_{\phi,r}$, split into the sum of the incident phase noise, $S_{\phi,m}$, and the added phase delay, $\Delta\phi$. I also included a minus sign picked up with respect to the incident field due to transmission twice through the input/output coupler.²¹ The first term in parenthesis represents the portion of the field that does not enter the resonator, but instead is reflected from the input coupler with the original phase noise of the field, $S_{\phi,m}$. Inspection of Equation 4.37 shows that the total reflected carrier field is zero when $\Delta\phi(\nu_n)$ is zero. I attempted to derive the explicit relation between the cavity leakage field amplitude and the original reflected field amplitude using the equivalent circuit analysis,²¹ as I'm sure it is a bit more complicated than that shown in Equation 4.37, but

was unable to do so. Equation 4.37 is adequate since it does lead to the same solution as previously found by Day for the PDH error signal (Ref. 30) and yields the same shot noise terms found by Siegman. The present technique is actually better suited to determining the transmitted fields of resonators, as shown in the next chapter.

The total reflected field, at position 3 in Figure 4.1, is the sum of the carrier field of Equation 4.37 and the reflected sidebands of Equation 4.5.

$$\tilde{E}_3 = \sqrt{R_c} \cdot E_m \cdot e^{i\omega_m t} \cdot e^{i \operatorname{Re} \left(-i \cdot S_{\phi, m} \cdot e^{i\omega_n t} \right)} \cdot \left[J_0(\beta) \cdot (1 - e^{i\Delta\phi(v_n)}) + 2i \cdot J_1(\beta) \cdot \sin \omega_p t \right] \quad (4.38)$$

Note that the phase noise of the sidebands is still $S_{\phi, m}$ since they did not couple into the resonator. The output voltage of the photodiode is proportional to the incident field power, the responsivity of the photodiode, R_{esp} (Amp/Watt), and the current to voltage gain of the photodetector circuitry, G_v (in V/Amp), as shown in Equation 4.39.

$$V_{\text{Det}} \propto R_{\text{esp}} \cdot G_v \cdot \left| \tilde{E}_3 \right|^2 \quad (4.39)$$

Substitution of Equation 4.38 into 4.39 yields the following detector voltage.

$$V_{\text{Det}} \propto R_{\text{esp}} \cdot G_v \cdot R_c \cdot |E_m|^2 \cdot \left\{ \left[2 \cdot (J_0(\beta))^2 \cdot (1 - \cos(\Delta\phi(v_n))) \right] + 4 \cdot (J_1(\beta))^2 \cdot \sin^2 \omega_p t + \right. \\ \left. - 4 \cdot J_0(\beta) \cdot J_1(\beta) \cdot \sin(\Delta\phi(v_n)) \cdot \sin(\omega_p t) \right\} \quad (4.40)$$

The third term of Equation 4.40 is the signal of interest at the modulation frequency. If we assume that the phase noise is small (i.e. $\Delta\phi(v_n) \ll 1$) then we can assume that $\sin \Delta\phi(v_n) \sim \Delta\phi(v_n)$ and the signal reduces to that shown in Equation 4.41.

$$V_{\text{Sig}} \propto -4 \cdot R_{\text{esp}} \cdot G_v \cdot R_c \cdot |E_m|^2 \cdot J_0(\beta) \cdot J_1(\beta) \cdot \Delta\phi(v_n) \cdot \sin \omega_p t \quad (4.41)$$

By substituting Equation 4.36 into this expression and defining the phase delay of Equation 4.42, the signal can be simplified to Equation 4.43.

$$\hat{\phi} = -\arctan(\kappa) \quad (4.42)$$

$$V_{Sig} \propto 4 \cdot R_{esp} \cdot G_v \cdot R_c \cdot |E_m|^2 \cdot J_0(\beta) \cdot J_1(\beta) \cdot \left(\frac{\kappa}{\sqrt{1+\kappa^2}} \right) \cdot (S_{\phi,c} - S_{\phi,m}) \cdot \cos(\omega_n t + \hat{\phi}) \cdot \sin(\omega_p t) \quad (4.43)$$

The signal of Equation 4.40 is mixed down (in quadrature) to DC as shown at position 4 of Figure 4.1. By substituting κ back into Equation 4.42 we arrive at the familiar form of the error signal, shown in Equation 4.44 in terms of the spectral density of frequency noise of the incident master laser, $S_{f,m}$, and cavity resonant frequency, $S_{f,c}$, the total incident optical power on the Fabry-Perot, P_{inc} (proportional to $R_c |E_m|^2$), and the halfwidth of the cavity reflection coefficient, $\delta\nu_c/2$.³⁰

$$V_{Sig} = 4 \cdot R_{esp} \cdot G_v \cdot P_{inc} \cdot J_0(\beta) \cdot J_1(\beta) \cdot \frac{1}{\sqrt{1 + \left(\frac{\nu_n}{\frac{\delta\nu_c}{2}} \right)^2}} \cdot \frac{(S_{f,c} - S_{f,m})}{\frac{\delta\nu_c}{2}} \cdot \cos(\omega_n t + \hat{\phi}) \quad (4.44)$$

Equation 4.44 can be simplified, as shown in Equation 4.45, in terms of the complex discriminator coefficient, $K_D(\nu_n)$, in units of V/Hz, and a variable η , in units of V/Hz.

$$V_{Sig} = \text{Re} \left(K_D(\nu_n) \cdot (S_{f,c} - S_{f,m}) \cdot e^{i\omega_n t} \right) \quad (4.45)$$

$$K_D(\nu_n) = \eta \cdot \frac{i \cdot \kappa}{1 + i \cdot \kappa} \quad (4.46)$$

$$\eta = \frac{4 \cdot R_{esp} \cdot G_v \cdot P_{inc} \cdot J_0(\beta) \cdot J_1(\beta)}{\nu_n} \quad (4.47)$$

Note that in the regime where $\nu_n \ll \delta\nu_c/2$, the discriminator coefficient, $K_D(\nu_n)$, is nearly linear, with slope equal to $\eta(\nu_n = \delta\nu_c/2)$ in V/Hz.

4.2 Frequency Control Theory

The total voltage output of the discriminator is equal to the sum of the signal of Equation 4.44 and the voltage noise of the discriminator, $S_{V,D}$. This signal is sent to the servo and actuator and then fed back to the laser, as discussed in Chapter 3. In Figure 4.4, I alter the noise control loop of Figure 3.5 to account for some of the new parameters of the derivation of the discriminator output of Section 4.1 and to represent the control loop in a manner analogous to the injection-locking control loop of the next chapter.

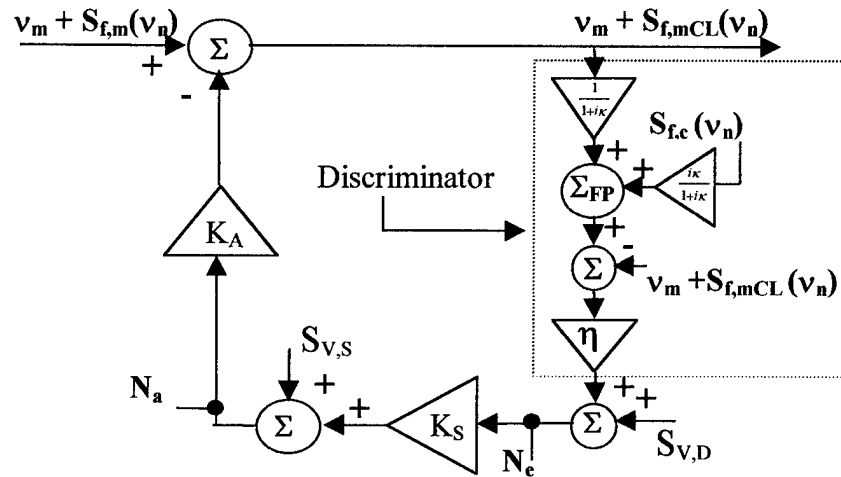


Figure 4.4. Frequency noise control loop (locking laser to Fabry-Perot).

The error signal derivation of the previous section is represented, in block diagram form, entirely within the dotted box. The frequency noise of the laser and the resonator are multiplied by their respective transfer functions and then summed onto the circulating field (and hence reflected field) of the Fabry-Perot, represented as Σ_{FP} . The frequency noise of the laser is then subtracted from the output of the Fabry-Perot, multiplied by η , and summed with $S_{V,D}$ to yield the discriminator output of Equations 4.45-4.47. The N_a point of Figure 4.4 corresponds to the output of the servo of Figure 4.1 and the $S_{f,mCL}$

represents the closed loop spectral density of frequency noise of the master laser at position 5 in Figure 4.1.

Tracing the signal clockwise through the loop as done in Chapter 3, yields the following expression for $S_{f,mCL}$.

$$S_{f,mCL}(\nu_n) = \left\{ \frac{\sqrt{(S_{f,m}(\nu_n))^2 + (K_A(\nu_n) \cdot K_S(\nu_n) \cdot S_{V,D})^2 + (K_A(\nu_n) \cdot S_{V,S})^2}}{|1 + G_{OL}(\nu_n)|} + S_{f,c}(\nu_n) \cdot G_{CL}(\nu_n) \right\} \quad (4.48)$$

Well within the feedback loop bandwidth (where $K_S(\nu_n) \gg 1$ and thus $G_{OL}(\nu_n) \gg 1$ and $G_{CL}(\nu_n) \sim 1$), Equation 4.48 simplifies to Equation 4.49.

$$S_{f,mCL}(\nu_n) \approx \frac{S_{V,D}}{K_D(\nu_n)} + S_{f,c}(\nu_n) \quad (4.49)$$

Equation 4.49 shows that $S_{f,mCL}$ is limited by the frequency noise of the reference cavity, $S_{f,c}$, and the voltage noise of the discriminator, $S_{V,D}$. Note that these expression are identical to Equations 3.15 and 3.16, (with $S_{f,CL}$ and $S_{f,Laser}$ replaced by $S_{f,mCL}$ and $S_{f,m}$) suggesting that the simplified control loop of Figure 3.5 is adequate for describing the locking of a laser to a Fabry-Perot.

For the PDH technique the three greatest discriminator noise sources are the amplitude noise floor of the incident laser at the modulation frequency $S_{A,m}(\nu_p)$, the shot noise of the photodetector output (assumed to be proportional to the incident DC signal), and the amplitude noise of the incident laser, $S_{A,m}(\nu_n)$. Generally, ν_p is placed at a high enough frequency that the amplitude noise is below the shot noise level of the detected signal. Further, the NPROs used in this thesis contained AM noise suppression feedback loops and displayed $S_{A,m}$ of -110 dB at ν_n of 1 Hz and above.¹²

The shot noise floor of the signal is proportional to the DC voltage output of the photodiode, found by isolating the DC terms of Equation 4.40. If we assume that $\Delta\phi(v_n) \ll 1$ and thus that the DC term due to the carrier field is zero, then the shot noise (in $V/Hz^{1/2}$) is primarily caused by the sideband signal strength as shown in Equation 4.50.

$$S_{V,D,SN}(v_n) = \sqrt{2 \cdot e \cdot I_{DC}} \cdot G_v = \sqrt{2 \cdot e \cdot R_{esp} \cdot P_{inc} \cdot 2 \cdot J_1^2(\beta)} \cdot G_v \quad (4.50)$$

Where I_{DC} is the DC current in Amps and e is the charge of an electron in Coulombs.

The amplitude noise of the incident field induces a phase noise in the reflected field when ω_m does not equal ω_c . Solution of the error signal, given the full expression of Equation 4.28, yields the following discriminator signal. The phase of the two cosine terms have been defined as the arc tangent of the ratio of the imaginary to real portions of the complex terms in the brackets in front of them. The last term of Equation 4.51 is the AM noise term shown alone in Equation 4.52.

$$V_{Sig} = 4 \cdot R_{esp} \cdot G_v \cdot P_{inc} \cdot J_0(\beta) \cdot J_1(\beta) \cdot \left\{ \begin{aligned} &\left| \frac{\omega_n \cdot \left(s + \frac{\gamma_c}{2} \right)}{D} \right|_a \cdot (S_{\phi,c} - S_{\phi,m}) \cdot \cos(\omega_n t + \hat{\phi}_a) \\ &- \left| \frac{\omega_n \cdot (\omega_m - \omega_c)}{D} \right|_b \cdot S_{A,m} \cdot \cos(\omega_n t + \hat{\phi}_b) \end{aligned} \right\} \quad (4.51)$$

$$S_{V,D,AM}(v_n) = 4 \cdot R_{esp} \cdot G_v \cdot P_{inc} \cdot J_0(\beta) \cdot J_1(\beta) \cdot \left| \frac{v_n \cdot (v_m - v_c)}{D(v_n)} \right| \cdot S_{A,m}(v_n) \quad (4.52)$$

Comparison of Equations 4.50 and 4.52 for a given experiment reveal which of these noise sources are greater at a given v_n . To ensure the AM induced noise is negligible with respect to the shot noise floor we must ensure that $\omega_c = \omega_m$. When the laser is locked, ω_c does not equal ω_m if there is a DC offset in the servo. To correct this, one can

inject a frequency noise onto the laser while it is locked to the resonance, at a dither frequency, ν_n , well above ν_{UG} to ensure it is not attenuated by the feedback loop. By monitoring the DC signal on the photodiode one can monitor the AM induced on the reflected field, $S_{A,r}(\nu_n)$. According to Equation 4.29, $S_{A,r}(\nu_n)$ is minimized when the DC offset of the servo zeroed, ensuring that $\omega_c = \omega_m$, and the FM induced by $S_{A,m}$ is eliminated in Equation 4.28. With the AM term reduced, the shot noise becomes the largest noise source of the discriminator.

By substituting Equations 4.50 and 4.47 into 4.49, one obtains the following minimum closed loop spectral density of frequency noise of laser (in the frequency regime where $G_{OL}(\nu_n) \gg 1$).

$$S_{f,mCL}(\nu_n) = S_{f,c}(\nu_n) + \sqrt{\frac{e}{4 \cdot R_{esp} \cdot P_{inc} \cdot (J_0(\beta))^2} \cdot \left[(\nu_n)^2 + \left(\frac{\delta\nu_c}{2} \right)^2 \right]} \quad (4.53)$$

Since e is a universal constant and R_{esp} is set by the photodiode used, our best options for achieving the minimal $S_{f,mCL}$ are to increase the optical power incident on the Fabry-Perot, and increase the finesse of the cavity, thus decreasing $\delta\nu_c$. Also, we can increase $J_0(\beta)$ by placing more power in the carrier portion of the incident field. This is done at the expense of the sideband power (proportional to $J_1(\beta)$), and eventually at the expense of the discriminator signal power (proportional to the product of $J_0(\beta)$ and $J_1(\beta)$). Since this analysis neglects the noise of the feedback electronics of the photodetector (which is generally within 10 dBV of the shot noise level) and other noise sources present in the discriminator, I generally avoided maximizing $J_0(\beta)$ and usually adjusted β for maximum signal strength ($\beta \sim 1.08$ as discussed in Ref. 30).

Since the control theory model of Chapter 3 is very similar to that of Figure 4.4, the discussion of the N_e and N_a point data and their relation to the open ($S_{f,m}(v_n)$) and closed loop ($S_{f,mCL}(v_n)$) spectral density of frequency noise is equally valid for this loop. After measuring the actuator and discriminator coefficients, one can use the N_e and N_a point data to predict $S_{f,m}(v_n)$ and $S_{f,mCL}(v_n)$ as shown in Equations 4.54 and 4.55.

$$S_{f,m}(v_n) - S_{f,c}(v_n) = \left\{ \begin{array}{ll} N_a(v_n) K_A(v_n) & \text{DC} < v_n < v_{UG} \\ \frac{N_e(v_n)}{K_D(v_n)} & v_n > v_{UG} \end{array} \right\} \quad (4.54)$$

$$S_{f,mCL}(v_n) - S_{f,c}(v_n) = \left\{ \begin{array}{ll} \frac{N_e(v_n)}{K_D(v_n)} & \text{All } v_n \end{array} \right\} \quad (4.55)$$

It is interesting to note that the frequency noise of the Fabry-Perot is present at N_e even outside the feedback loop bandwidth.

Note that Equations 4.54 and 4.55 are identical to Equations 3.21 and 3.22, suggesting that the simple control loop diagram of Figure 3.5 is adequate in describing this experiment.

4.3 Measuring K_A , K_D , and δv_c

By monitoring the PDH error signal (obtained by mixing in quadrature) while sweeping the carrier frequency and two modulation sidebands of the laser through v_c , one can measure K_A , K_D , and δv_c . A sample of the resulting error signal obtained when triggering the oscilloscope on the voltage ramp applied to the Fast PZT of the NPRO is shown in Figure 4.5. By deriving the PDH error signal given a frequency sweep of the laser frequency (while still modulated at a frequency v_p), one finds the exact dependence shown in the first plot, with the x-axis in units of frequency, v_m .

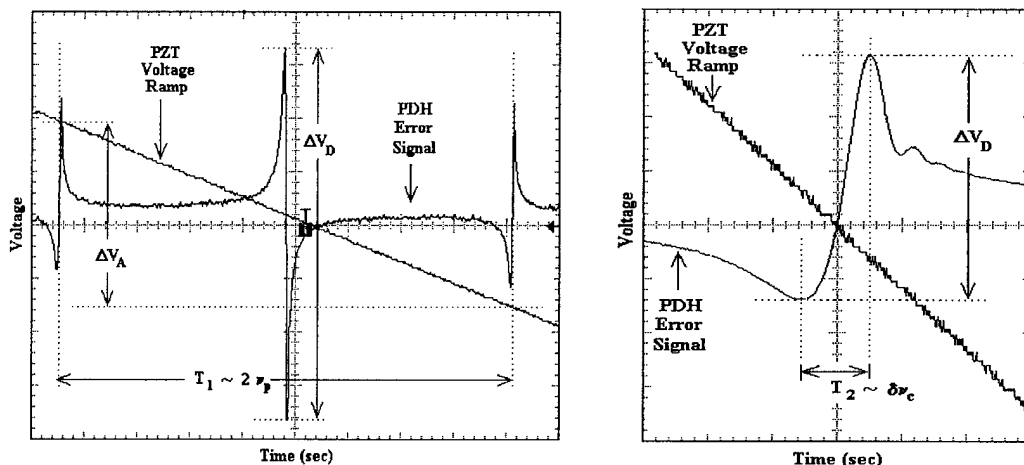


Figure 4.5. Measuring K_A , K_D , and $\delta\nu_c$ using PDH Error Signal.

The centers of the three dispersive regions occur when the laser and its two sidebands sweep through the resonance. Thus, ν_m is equal to $\nu_c + \nu_p$, ν_c , and $\nu_c - \nu_p$ at the centers of the three peaks from left to right in the first plot. To convert the oscilloscope x-axis from a time scale to the frequency output of the laser, ν_0 , assume a linear PZT excursion, in $\mu\text{m}/\text{sec}$, and a consequent linear frequency excursion, in Hz/sec . The ratio of the frequency deviation of ν_0 between the first and third peaks (equal to $2\nu_p$) to the voltage applied to the laser, ΔV_A , to cause this deviation, is equal to K_A , in Hz/V . The derivation of the quadrature error signal also reveals that the width of the central peak, expanded in the second plot, is equal to $\delta\nu_c$. Since the ratio of T_2 to T_1 is equal to the ratio of $\delta\nu_c$ to $2\nu_p$, measurement of T_1 and T_2 and knowledge of ν_p yields the value of $\delta\nu_c$. Next, the ratio of the peak-to-peak voltage of the PDH signal, ΔV_D , to the frequency spread of the central dispersion curve, $\delta\nu_c$, is approximately equal to the slope of the central dispersion curve, K_D in V/Hz . For a more accurate determination of K_D at low frequencies, one can zoom in further on the linear portion of the PDH signal of the second plot.

4.4 Common Measurements and Results

Several NPRO lasers were stabilized to Fabry-Perot resonators over the course of this thesis.⁴⁹ The PZT and temperature controller of these lasers served as the fast and slow frequency actuator elements, respectively, of the overall feedback loop. The Fast PZT of the Lightwave Electronics Model 122 NPRO displayed a strong resonance near 30 kHz, limiting ν_{UG} to 15-20 kHz. A NewFocus model 1611 low noise 1 GHz detector was used as the photodetector, with a R_{esp} of 0.6 A/W, a G_v of 250 V/A, and a maximum incident power of 10 mW. The Fabry-Perot used was a Newport Supercavity Model 150c. I measured $\delta\nu_c$ of a particular Fabry-Perot using the technique described in Section 4.3 and using the cavity ring down technique.⁵⁰ I found that the measured $\delta\nu_c$ for both techniques varied by as much as 25 kHz between measurements but the ring down technique was much more complex and required much more time (10 minutes compared to 30 seconds). The average measurement of both techniques was nearly 160 kHz. Common values of K_A and K_D were found to be 5 MHz/V and 1.5 V/MHz, respectively.

Substitution of R_{esp} , P_{inc} , and $\delta\nu_c$ in Equation 4.54 suggests that the minimum $S_{f,mCL}$ achievable by locking an NPRO to this Fabry-Perot would be nearly 4×10^{-4} Hz/Hz^{1/2}, which would produce a linewidth of less than 1 μ Hz, if we assumed $S_{f,mCL}$ was white with respect to ν_n , and neglect S_{fc} . However, the best linewidth achieved by stabilizing the master laser NPRO of this thesis was on the order of 600 mHz.⁴⁹ The discrepancy between experiment and theory is caused by the following facts: $S_{f,mCL}$ is dependent on ν_n , S_{fc} is not negligible, and other noise sources (such as line noise at 60 Hz in the various power supplies employed) are present in such experiments.

4.5 Summary

I have derived the PDH error signal obtained when locking a laser to a resonant frequency of a Fabry-Perot beginning with the damped, driven wave equation describing the circulating field of the Fabry-Perot.

I have shown the various benefits of this analysis. First, it reveals the frequency noise transfer functions of the incident laser frequency noise and the frequency noise of the Fabry-Perot's resonant frequency onto the circulating field of the cavity. It also predicts the AM to FM coupling between the incident and circulating fields and reveals that by adjusting the servo DC offset one can eliminate this AM to FM conversion to optimize the signal to noise ratio of the PDH error signal.

I have shown that while the laser's frequency noise transfer function is a low pass filter and the resonator's frequency noise transfer function is a high pass filter (both of corner frequency $\delta\nu_c/2$), the PDH error signal is equally susceptible to each. Also, I have altered the frequency noise control loop of Figure 3.5 to account for the parameters of this derivation and found that the analysis of this loop revealed the same results as the simple analysis of Chapter 3. However, the frequency noise transfer functions and the complex control loop of Figure 4.4 will simplify the comparison of this experiment with that of PDH injection-locking technique of Chapter 5, and create a basis for establishing a complete description of the frequency stabilization of the frequency-doubler of Chapter 7.

Finally, I discussed the fact that the determination of the cavity bandwidth ($\delta\nu_c$) using the PDH quadrature error signal was nearly as accurate as the cavity ring down technique and much simpler and faster to perform.

CHAPTER 5. Frequency Stabilization of an Injection-Locked Laser

In this chapter, I present the control theory that I developed to model the frequency stabilization aspect of the injection-locking process based on the results of the various experiments discussed in Chapter 6. I review the derivation of the frequency noise transfer functions of the master laser and slave resonator onto the injection-locked output.²³ I use these transfer functions to derive, for the first time in the literature, the error signal obtained when using the PDH technique to lock the oscillation frequency of the slave laser to the master laser. I determine the experimental parameters yielding the minimal achievable injection-locked spectral density of frequency noise and compare them to the optimal parameters derived for the case of locking a laser to a Fabry-Perot. Finally, I compare the theoretical results of three additional “global” stabilization schemes complementing the original PDH injection-locking loop.

5.1 Passive Injection Locking

Consider a slave ring laser cavity seeded by a master laser as shown in Figure 5.1.

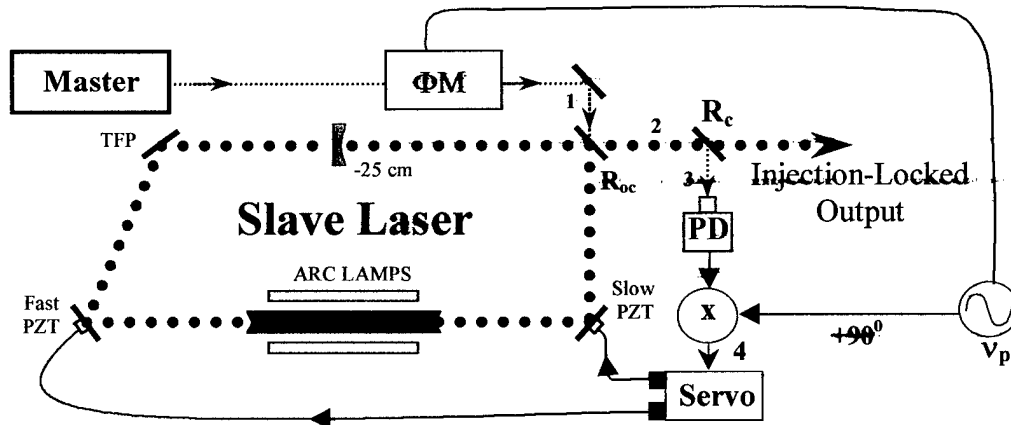


Figure 5.1. Injection-Locking experimental set-up.

If a beam block is placed in the path of the master field just after point 1 in the figure to isolate the two lasers, the electric fields of the master and slave lasers at points 1 and 2,

respectively, are shown in Equations 5.1 and 5.2. The amplitude, E_s , and carrier radial frequency, ω_s , of the electric field of the slave laser are independent of the amplitude, E_m , and carrier frequency, ω_m , of the master laser. Equation 5.1 also lists the amplitude, β , and frequency, ω_p , of the modulation sidebands placed on the master laser. The phase noise of the master, $\phi_m(t)$, and slave, $\phi_s(t)$, are defined in Equations 5.3 and 5.4.

$$\tilde{E}_1 = E_m \cdot e^{i\omega_m t} \cdot e^{i\phi_m(t)} \cdot e^{i\beta \sin(\omega_p t)} = E_m \cdot e^{i\omega_m t} \cdot e^{i\phi_m(t)} \cdot [J_0(\beta) + 2i \cdot J_1(\beta) \cdot \sin(\omega_p t)] \quad (5.1)$$

$$\tilde{E}_2 = E_s(t) \cdot e^{i\omega_s t} \cdot e^{i\phi_s(t)} \quad (5.2)$$

$$\phi_m(t) = S_{\phi,m}(\omega_n) \cdot \sin(\omega_n t) = \text{Re}(-i \cdot S_{\phi,m}(\omega_n) \cdot e^{j\omega_n t}) \quad (5.3)$$

$$\phi_s(t) = S_{\phi,s}(\omega_n) \cdot \sin(\omega_n t) = \text{Re}(-i \cdot S_{\phi,s}(\omega_n) \cdot e^{j\omega_n t}) \quad (5.4)$$

When the beam block is removed, a portion of the incident field of the master laser seeds the slave resonator and competes with the existing circulating field for gain in the Nd:YAG rod. For a range of master laser frequencies, centered at the unseeded slave cavity resonant frequency, ω_s , the circulating field created by the amplified master laser field exceeds the original circulating field of the slave laser. The incident field saturates the gain of the Nd:YAG rod at the expense of the gain of the original mode(s) of the slave laser. In this range of frequencies, known as the lock range (equal to $2 \omega_{\text{Lock}}$ and defined below), the frequency output of the slave laser is “locked” to the frequency of the master laser electric field.

The damped, driven wave equation for the circulating field of the slave resonator is shown in Equation 5.5.²¹ This equation is similar to the expression obtained for the empty Fabry-Perot (Equation 4.11) with the addition of a polarization driving term arising from the slave laser gain medium. As in Equation 4.11, only the spectral portion

of the incident master field neighboring ω_m , shown in Equation 5.6, couples into the resonator and seeds this process. Assume the incident field is perfectly mode-matched to the slave resonator.

$$\frac{d^2 \tilde{E}_c}{dt^2} + \gamma_c \cdot \frac{d \tilde{E}_c}{dt} + (\omega_s)^2 \cdot \tilde{E}_c = \sqrt{\frac{8 \cdot \gamma_e}{\epsilon \cdot V_c}} \cdot \frac{d}{dt} \left[\tilde{E}_{inc}(\omega_m) \right] - \frac{1}{\epsilon} \cdot \frac{d^2 \tilde{P}}{dt^2} \quad (5.5)$$

$$\tilde{E}_{inc}(\omega_m) = J_0(\beta) \cdot E_m \cdot e^{i\omega_m t} \cdot e^{i\phi_m(t)} = E_{inc} \cdot e^{i\omega_m t} \cdot e^{i\phi_m(t)} \quad (5.6)$$

The total cavity energy decay rate, γ_c , the decay rate due to internal slave cavity losses, γ_0 , and the decay rate due to external coupling, γ_e , are defined in Equation 5.7 in terms of the speed of light, c , the length of the slave resonator, L , the power reflectivity of the output coupler, R_{oc} , and the absorption coefficient of the slave resonator medium, α_0 .

$$\gamma_c = \gamma_0 + \gamma_e = 2 \cdot \alpha_0 \cdot c + \frac{c}{L} \cdot \ln \left(\frac{1}{R_{oc}} \right) \quad (5.7)$$

The circulating field oscillates at the same carrier frequency as the master field but has a phase noise term, $\phi_c(t)$, as shown in Equation 5.8. The polarization term is defined with a term driving in phase with the circulating field, χ' , and a term driving out of phase, χ'' , as shown in Equation 5.9.²¹

$$\tilde{E}_c = E_c \cdot e^{i\omega_m t} \cdot e^{i\phi_c(t)} \quad (5.8)$$

$$\tilde{P} = (\chi' + i\chi'') \cdot \epsilon \cdot E_c \cdot e^{i\omega_m t} \cdot e^{i\phi_c(t)} \quad (5.9)$$

By substituting Equations 5.6, 5.8, and 5.9 into Equation 5.5, making a slowly varying envelope approximation, and equating the real and imaginary portions of the resulting equations, Siegman obtains two coupled expressions for E_c and ϕ_c . After coupling these expressions out of the slave resonator (to point 2 in Figure 5.1), as done in Equations 4.16

and 4.17 for the Fabry-Perot case, he obtains the following coupled expressions for the injection locked field amplitude, E_{IL} , and phase, ϕ_{IL} . Assume $\phi_c = \phi_{IL}$.²¹

$$\frac{dE_{IL}}{dt} + \frac{\gamma_c - \gamma_m}{2} \cdot E_{IL} = \gamma_e \cdot E_{inc} \cdot \cos[\phi_{IL} - \phi_m] \quad (5.10)$$

$$\frac{d\phi_{IL}}{dt} + \omega_m - \omega_{pull} = -\gamma_e \cdot \frac{E_{inc}}{E_{IL}} \cdot \sin[\phi_{IL} - \phi_m] \quad (5.11)$$

Equations 5.10 and 5.11 are nearly identical to Equations 4.18 and 4.19 obtained for the vacant Fabry-Perot case with two additional terms defined in Equations 5.12 and 5.13.

$$\gamma_m = \omega_m \cdot \chi'' \quad (5.12)$$

$$\omega_{pull} = \omega_s - \omega_m \cdot \frac{\chi'}{2} \quad (5.13)$$

Where γ_m is the field growth rate and ω_{pull} is the pulled resonant frequency of the slave cavity. To solve Equations 5.10 and 5.11 at a given noise frequency, ν_n , assume E_{inc} , E_{IL} , ϕ_m , ϕ_{IL} , and ω_{pull} oscillate with small perturbations about their steady state values (represented with subscript zero) just as done for E_{inc} , E_r , ϕ_m , ϕ_r and ω_c in Equations 4.20-4.24. The steady state solutions of Equations 5.10 and 5.11 yield the following expressions for the steady state phase delay, $\Delta\phi_{ss}$, of the injection-locked output field with respect to the incident master laser field and the lock range frequency, ω_{Lock} .

$$\Delta\phi_{ss} = \phi_{IL} - \phi_m = \arctan\left(\frac{\omega_m - \omega_{pull}}{\omega_{lock}}\right) \quad (5.14)$$

$$\omega_{lock} = \gamma_e \cdot \frac{E_{inc,0}}{E_{IL,0}} = \gamma_e \cdot \frac{\eta_c \cdot J_0(\beta) \cdot E_m}{E_{IL}} \approx \eta_c \cdot T_{oc} \cdot FSR \cdot J_0(\beta) \cdot \sqrt{\frac{P_m}{P_{IL}}} \quad (5.15)$$

Where η_c is the percentage of the incident master laser mode coupled into the slave resonator's spatial and polarization mode.^{21,51} Assuming perfect mode matching, $\eta_c = 1$.

The second expression of Equation 5.15 is obtained by substituting the amplitude of Equation 5.6 into the first expression, and the final expression is obtained by noting that the Free Spectral Range (FSR) of a ring cavity is equal to c/L and by assuming that $\ln(1/R_{oc}) \sim 1 - R_{oc} = T_{oc}$ (the power transmission coefficient of the output coupler). Also, P_m and P_{IL} are the total optical powers of the incident master laser and the injection-locked laser. Comparison of Equation 5.14 and 4.25 suggests that the photon lifetime of the circulating field is equal to $1/\omega_{Lock}$. Plotting Equation 5.14 yields a figure identical to Figure 4.2 with ν_c and $\delta\nu_c/2$ replaced by ν_{pull} and ν_{Lock} . This phase delay serves as the basis for the PDH error signal used to lock ω_{pull} to ω_m .

Equations 5.10 and 5.11 are solved by introducing into them the perturbations of E_{inc} , E_{IL} , ϕ_m , ϕ_{IL} , and ω_{pull} and making the same assumptions used to solve Equations 4.18 and 4.19 (as done in Ref. 23). The injection-locked output at position 2 in Figure 5.1 is given by Equation 5.16 where the spectral density of phase noise, $S_{\phi,IL}$, and amplitude noise, $S_{A,IL}$, of Equations 5.17 and 5.18 have a common denominator, D_{IL} , defined in Equation 5.19.

$$\tilde{E}_{IL} = E_{IL} \cdot (1 + S_{A,IL} \cdot e^{i\omega_n t}) \cdot e^{i\omega_m t} \cdot e^{i \text{Re}(-iS_{\phi,IL} \cdot e^{i\omega_n t})} \quad (5.16)$$

$$S_{\phi,IL} = \left\{ \begin{aligned} & \left[\frac{s \cdot (s + \omega_{Lock})}{D_{IL}} \right] \cdot S_{\phi,s} + \left[\frac{(\omega_{Lock}) \cdot (s + \omega_{Lock}) + (\omega_m - \omega_{pull})^2}{D_{IL}} \right] \cdot S_{\phi,m} \\ & + \left[\frac{s \cdot (\omega_m - \omega_{pull})}{D_{IL}} \right] \cdot S_{A,m} \end{aligned} \right\} \quad (5.17)$$

$$S_{A,IL} = \left[\frac{s \cdot (\omega_m - \omega_{pull})}{D_{IL}} \right] \cdot (S_{\phi,IL} - S_{\phi,m}) \quad (5.18)$$

$$D_{IL} = (s + \omega_{Lock})^2 + (\omega_m - \omega_{pull})^2 \quad (5.19)$$

As in Chapter 4, the variable s is equal to $i\omega_n$. The second term of Equation 4.29 which coupled $S_{A,m}$ to $S_{A,r}$ has been eliminated in Equation 5.18 since a proper discussion of the coupling of $S_{A,m}$ to $S_{A,IL}$ in the presence of the gain medium must account for the saturation of the population inversion.²²

If we assume that ω_m equals ω_{pull} , neglect $S_{A,m}$, multiply both sides of Equation 5.17 by v_n , and convert phase noise terms, S_ϕ , into frequency noise terms, S_f , then we arrive at the following expression in terms of the variable κ_{IL} , defined in Equation 5.21.

$$S_{f,IL} = \left[\frac{i \cdot \kappa_{IL}}{1 + i \cdot \kappa_{IL}} \right] \cdot S_{f,s} + \left[\frac{1}{1 + i \cdot \kappa_{IL}} \right] \cdot S_{f,m} = T_S(v_n) \cdot S_{f,s} + T_M(v_n) \cdot S_{f,m} \quad (5.20)$$

$$\kappa_{IL} = \frac{\omega_n}{\omega_{Lock}} = \frac{v_n}{v_{Lock}} \quad (5.21)$$

The bracketed terms in front of $S_{f,s}$ and $S_{f,m}$ are the frequency noise transfer functions of the slave resonator frequency noise, $T_S(v_n)$, and the master laser frequency noise, $T_M(v_n)$, onto the injection-locked output, respectively. Comparison of Equation 5.20 with Equations 4.33 and 4.34 reveals that $T_S(v_n)$ is a high pass filter of corner frequency v_{Lock} (i.e. $T_S(v_n) = T_{HIGH}(v_n, v_{Lock})$), and $T_M(v_n)$ is a low pass filter of corner frequency v_{Lock} (i.e. $T_M(v_n) = T_{LOW}(v_n, v_{Lock})$), as shown in Figure 5.2.

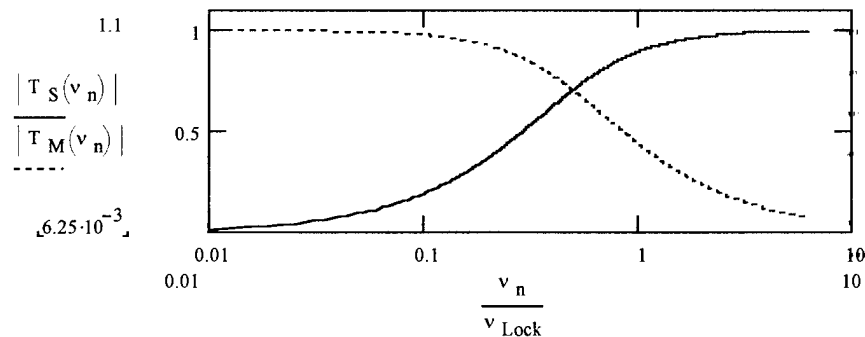


Figure 5.2. Frequency noise transfer functions of master and slave onto injection-locked output.

The only difference between T_C and T_L of Figure 4.3 and T_S and T_M of Figure 5.2 is that the corner frequency changes from $\delta\nu_c/2$ to ν_{Lock} . This suggests that the only difference between this simplified model of injection-locking and the analysis of the Fabry-Perot is the photon lifetime of the circulating field. According to Equation 5.20 and Figure 5.2, at $\nu_n \ll \nu_{\text{Lock}}$, $S_{f,IL}$ is the sum of $S_{f,m}$ and a much attenuated $S_{f,s}$. Figure 5.3 displays the block diagram schematic of the injection-locking results of Equation 5.20 and will serve as the building block for the control theory discussions below.

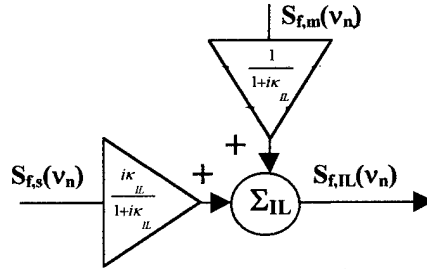


Figure 5.3. Injection-Locking frequency noise transfer functions.

5.2 Derivation of Error Signal

To improve the frequency stability of the injection-locked output we implement a PDH locking scheme to further reduce the slave resonator frequency noise contributions. The total field at position 2 of Figure 5.1 is the sum of the injection-locked output of Equation 5.16, and the reflected modulation sidebands of Equation 5.1.

$$\tilde{E}_2 = e^{i\omega_m t} \cdot \left[E_{IL} \cdot e^{i\text{Re}(-iS_{\phi,IL} \cdot e^{i\omega_n t})} + 2i \cdot J_1(\beta) \cdot E_m \cdot e^{i\text{Re}(-iS_{\phi,m} \cdot e^{i\omega_n t})} \sin(\omega_p t) \right] \quad (5.22)$$

A portion of this field is directed to the photodiode at position 3 in Figure 5.1 with a mirror of power reflectivity R_c . The voltage output of the photodiode is proportional to the incident optical power at position 3, the responsivity of the photodiode, R_{esp} , and the current to voltage gain of the photodetector circuitry, G_v , as shown in Equation 5.23.

$$V_{Det} \propto R_{esp} \cdot G_v \cdot \left| \tilde{E}_3 \right|^2 = R_{esp} \cdot G_v \cdot R_c \cdot \left| \tilde{E}_2 \right|^2 \quad (5.23)$$

Substitution of Equation 5.22 into 5.23 yields the following detector voltage.

$$V_{Det} \propto R_{esp} \cdot G_v \cdot R_c \cdot \left(\left| E_{IL} \right|^2 + 4 \cdot (J_1(\beta))^2 \cdot \left| E_m(t) \right|^2 \cdot \sin^2 \omega_p t \right. \\ \left. + E_{IL} \cdot E_m \cdot J_1(\beta) \cdot 2i \cdot \sin(\omega_p t) \cdot \left\{ e^{i \left(\text{Re}[-i S_{\phi,m} \cdot e^{i\omega_n t}] - \text{Re}[-i S_{\phi,IL} \cdot e^{i\omega_p t}] \right)} - c.c \right\} \right) \quad (5.24)$$

The third expression of Equation 5.24 is the signal of interest at ω_p . This signal is mixed down in quadrature and simplified just as done in Chapter 4 from Equations 4.41 to 4.44 to yield the following discriminator output at position 4 of Figure 5.1.

$$V_{Sig} \propto 4 \cdot R_{esp} \cdot G_v \cdot R_c \cdot J_1(\beta) \cdot E_m \cdot E_{IL} \cdot \frac{\kappa_{IL}}{|1 + i\kappa_{IL}|} \cdot (S_{\phi,s} - S_{\phi,m}) \cdot \cos(\omega_n t + \hat{\phi}_{IL}) \quad (5.25)$$

The added phase of the cosine term is defined as shown in Equation 5.26.

$$\hat{\phi}_{IL} = -\arctan\left(\frac{v_n}{v_{Lock}}\right) \quad (5.26)$$

Equation 5.25 is simplified to Equation 5.27 by grouping terms into a PDH injection-locking feedback loop discriminator constant, $K_{D,IL}(v_n)$, shown in Equation 5.28 of units V/Hz, and the variable, η_{IL} shown in Equation 5.29 of units V/Hz.

$$V_{Sig} = \text{Re}\left(K_{D,IL}(v_n) \cdot (S_{f,s} - S_{f,m}) \cdot e^{i\omega_n t}\right) \quad (5.27)$$

$$K_{D,IL}(v_n) = \eta_{IL} \cdot \frac{i\kappa_{IL}}{1 + i\kappa_{IL}} \quad (5.28)$$

$$\eta_{IL} = \frac{4 \cdot R_c \cdot R_{esp} \cdot G_v \cdot J_1(\beta) \cdot \sqrt{P_m} \cdot \sqrt{P_{IL}}}{v_n} \approx \frac{4 \cdot R_{esp} \cdot G_v \cdot J_0(\beta) \cdot J_1(\beta) \cdot P_m}{v_n} \cdot \left[\frac{R_c \cdot T_{OC} \cdot FSR}{2 \cdot \pi \cdot v_{Lock}} \right] \quad (5.29)$$

Although the frequency noise of the injection-locked output of Equation 5.20 is more susceptible to master laser noise at $v_n \ll v_{Lock}$, Equation 5.27 shows that the PDH error

signal is equally susceptible to master laser and slave resonator frequency noise. Also, Equation 5.29 shows that the value of η_{IL} is very similar to η for the Fabry-Perot (Equation 4.47), but with the added term in brackets in Equation 5.29. In the regime where $\nu_n \ll \nu_{Lock}$, it can be shown that the discriminator slope is equal to $\eta_{IL}(\nu_n = \nu_{Lock})$. When substituting the experimental values of the terms in the brackets of Equation 5.29 into this expression, the bracketed term approximately equals 0.09. This suggests that the discriminator slope of the PDH injection-locking loop was generally a factor of 10 lower than the Fabry-Perot case in the experiments of this thesis, primarily due to the near factor of 10 difference between $\delta\nu/2$ (~ 80 kHz) and ν_{Lock} (~ 750 kHz).

5.3 Frequency Control Theory

The discriminator error signal of Equation 5.27 is amplified by a servo of transfer function $K_{S,IL}$, and sent to the actuator of transfer function $K_{A,IL}$. The actuator in this case is a PZT mounted behind a slave resonator mirror of Figure 5.1. Figure 5.4 shows the effective control loop created.

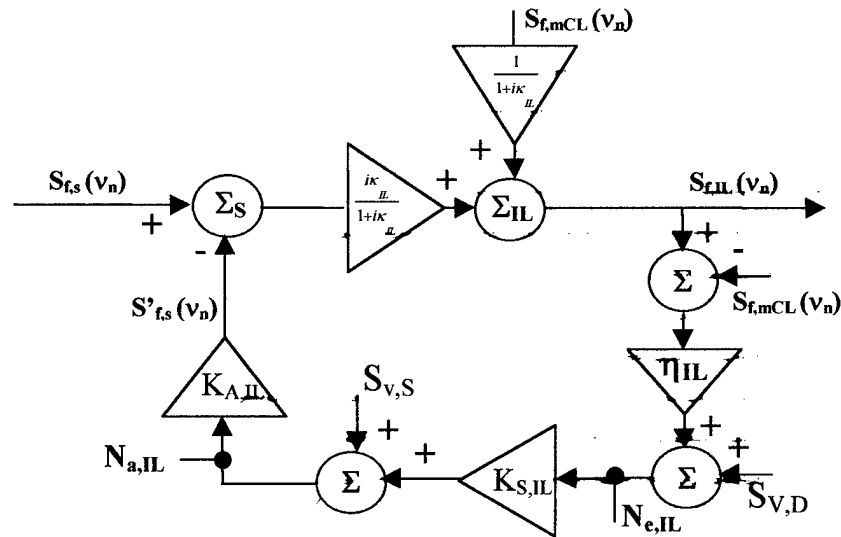


Figure 5.4. Frequency noise control loop (injection-locking).

The slave resonator is considered to be a frequency summer, Σ_s , with its original noise, $S_{f,s}$, added to the feedback noise signal, S'_{fs} . The frequency noise of the master laser, $S_{f,mCL}$, (with subscript CL for closed loop in case it has its own feedback loop) and slave resonator are summed, in Σ_{IL} , onto the injection-locked output after being multiplied by their respective transfer functions. The error signal of Equation 5.27 is obtained at the $N_{e,IL}$ point of Figure 5.4, along with the noise contributions of the discriminator, $S_{v,D}$, primarily arising from the shot noise of the photodiode. Also, the voltage noise of the servo, $S_{v,S}$, is caused by the Johnson noise of its resistors as discussed in Chapter 3.

By tracing the loop in the clockwise direction we obtain the following closed loop spectral density of frequency noise, $S_{f,IL}$, shown in Equation 5.30:

$$S_{f,IL}(\nu_n) = \left\{ \frac{\sqrt{(S_{f,s}(\nu_n))^2 + (K_{A,IL}(\nu_n) \cdot K_{S,IL}(\nu_n) \cdot S_{v,D})^2 + (K_{A,IL}(\nu_n) \cdot S_{v,S})^2}}{|1 + G_{OL,IL}(\nu_n)|} \cdot T_{S,CL}(\nu_n) \right\} + S_{f,mCL}(\nu_n) \cdot T_{M,CL}(\nu_n) \quad (5.30)$$

I have grouped a few terms into an injection-locking open loop transfer function, $G_{OL,IL}(\nu_n)$, defined in Equation 5.31, and the closed loop master and slave frequency noise transfer functions, $T_{M,CL}(\nu_n)$ and $T_{S,CL}(\nu_n)$, defined in Equations 5.32 and 5.33.

$$G_{OL,IL}(\nu_n) = K_{A,IL}(\nu_n) \cdot K_{S,IL}(\nu_n) \cdot K_{D,IL}(\nu_n) \quad (5.31)$$

$$T_{S,CL}(\nu_n) = \left\{ \frac{i \cdot \kappa_{IL}}{1 + i \cdot \kappa_{IL}} \right\} = T_S(\nu_n) \quad (5.32)$$

$$T_{M,CL}(\nu_n) = \left\{ \frac{1 + i \cdot \kappa_{IL} \cdot \frac{G_{OL,IL}(\nu_n)}{1 + G_{OL,IL}(\nu_n)}}{1 + i \cdot \kappa_{IL}} \right\} = T_M(\nu_n) + \frac{i \cdot \kappa_{IL}}{1 + i \cdot \kappa_{IL}} \cdot \frac{G_{OL,IL}(\nu_n)}{1 + G_{OL,IL}(\nu_n)} \quad (5.33)$$

Equations 5.32 and 5.33 show that the presence of the PDH injection-locking feedback loop alters the frequency noise transfer functions of the master and slave laser onto the

injection-locked output. Outside the loop bandwidth (where $G_{OL,IL}(\nu_n) \ll 1$), $T_{M,CL}$ approaches its open loop value, T_M , and $S_{f,IL}$ approaches its open loop value given in Equation 5.20. Inside the loop bandwidth (where $G_{OL,IL}(\nu_n) \gg 1$), the frequency noise contributions of the slave resonator are greatly reduced, but the master laser frequency noise is transferred directly onto the injection locked output (i.e. $T_{M,CL}(\nu_n) \sim 1$). In fact, Equation 5.33 suggests that the PDH loop can shift the corner frequency of the master laser frequency noise transfer function out beyond ν_{Lock} if the bandwidth of the injection-locking feedback loop, $G_{OL,IL}$, is made larger than ν_{Lock} .

In the limiting case, where $K_{S,IL}(\nu_n) \gg 1$, the minimal closed loop spectral density of frequency noise of the injection-locked output is given by Equation 5.34.

$$S_{f,IL}(\nu_n) \approx \frac{S_{V,D}}{K_{D,IL}(\nu_n)} \cdot T_{S,CL}(\nu_n) + S_{f,mCL}(\nu_n) \cdot T_{M,CL}(\nu_n) \approx \frac{S_{V,D}}{\eta_{IL}} + S_{f,mCL}(\nu_n) \quad (5.34)$$

The last expression is obtained by substituting the explicit forms of $K_{D,IL}$ and $T_{S,CL}$, from Equations 5.28 and 5.32, into the first relation and assuming that $T_{M,CL} \sim 1$. Note that the second expression is different from the similar relation obtained for the Fabry-Perot case (Equation 4.49), due to the presence of the master and slave frequency noise transfer functions in the first expression.

As in Chapter 4, the three primary discriminator noise sources are the residual AM noise of the master laser or injection-locked output at ν_p , the coupling of $S_{A,m}(\nu_n)$ to the error signal if ω_m does not equal ω_{pull} in Equation 5.17, and the shot noise of the photodiode signal. Generally $S_{A,m}(\nu_p)$ is negligible for the NPROs used as the master lasers in this thesis and $S_{A,IL}(\nu_p)$ is greatly reduced by the injection-locking process to a negligible value with a proper selection of the ratio of P_m to P_{IL} .²² Also, as discussed in

Chapter 4, a frequency noise is placed on the master laser and $S_{A,IL}(\nu_n)$ (of Equation 5.18) is minimized by fine tuning the servo DC offset. This ensures $\omega_m = \omega_{pull}$ and thus eliminates the AM to FM conversion predicted in Equation 5.17. The largest remaining noise source is the shot noise of Equation 5.35, assumed to be proportional to the largest DC signal on the photodiode (the first term of Equation 5.24).

$$S_{V,D,SN}(\nu_n) = \sqrt{2 \cdot e \cdot R_{esp} \cdot R_c \cdot P_{IL}} \cdot G_v \quad (5.35)$$

By introducing Equations 5.35 and 5.29 into Equation 5.34 we obtain the following expression for $S_{f,IL}$ in $\text{Hz/Hz}^{1/2}$.

$$S_{f,IL}(\nu_n) = S_{f,mCL}(\nu_n) + \sqrt{\frac{e \cdot (\nu_n)^2}{8 \cdot R_{esp} \cdot R_c \cdot P_m \cdot (J_1(\beta))^2}} \quad (5.36)$$

A key similarity between the minimum injection-locked spectral density of frequency noise (of Equation 5.36) and that of the laser locked to a Fabry-Perot (of Equation 4.53) is that they are both inversely proportional to the incident laser power on either the slave cavity or the Fabry-Perot.

The first key difference between Equation 5.36 and Equation 4.53 is that the relative noise of $S_{f,IL}$ with respect to its reference (the master laser) is nearly zero at low frequencies, increases without bound at higher noise frequencies, and is not a function of ν_{Lock} . On the other hand, the relative noise of the laser locked to the Fabry-Perot is non zero at low noise frequencies and resembles a low pass filter of corner frequency $\delta\nu_c/2$. Second, the minimum $S_{f,IL}$ is achieved by increasing the total master laser power incident on the slave cavity (including sidebands). Note that Equation 5.36 suggests that maximizing the power in the sidebands (increasing $J_1(\beta)$) yields a minimal relative frequency noise. This is opposite to what we found for the PDH locking a laser to a

Fabry-Perot which suggested that maximizing the power in the carrier portion of the signal (by increasing $J_0(\beta)$) yielded the best signal to noise ratio. This is not surprising since the detector signal of the Fabry-Perot field obtained in reflection has a negligible carrier field contribution and a large sideband signal, while the injection-locking detector signal has a very large carrier signal and a small sideband field. Thus, when only considering shot noise, it stands to reason that the two cases would be different.

However, as I doubted the maximizing of $J_0(\beta)$ at the expense of $J_1(\beta)$ in Chapter 4, doing the opposite here seems to be equally questionable. After all, placing more power in the sidebands reduces the portion of the incident master field coupled into the resonator, which reduces the output power, P_{IL} , and ν_{Lock} . To understand the exact effect of increasing $J_1(\beta)$ a future analysis must obtain an explicit relation between the coupled portion of the master laser power into the slave resonator and P_{IL} . I was unable to obtain such an expression though I thought such an expression should have presented itself from the solution of Equation 5.10 in the steady state regime, assuming perfect impedance matching and zero phase delay between the circulating and incident fields. I generally set $\beta \sim 1.08$ since, as in Chapter 4, this analysis neglects the contributions of other discriminator noise sources, such as the electronics noise of the photodetector.

Finally, it was unclear in the literature exactly what information could be obtained from the error and actuator points of the injection-locking loop ($N_{e,IL}$ and $N_{a,IL}$ of Figure 5.4). I showed that the simple addition of $S_{f,REF}$ in Figure 3.5 accurately modeled the Fabry-Perot control loop in Chapter 4, but the injection-locking control loop of Figure 5.4 is somewhat more complicated than that of the Fabry-Perot (Figure 4.4). By tracing the

signal clockwise through the control loop one can solve for the signal obtained at the error and actuator points.

$$N_{e,IL}(\nu_n) = K_{D,IL}(\nu_n)(S_{f,s}(\nu_n) - S_{f,mCL}(\nu_n)) \quad \nu_n \gg \nu_{UG} \quad (5.37)$$

$$N_{a,IL}(\nu_n) = \frac{(S_{f,s}(\nu_n) - S_{f,mCL}(\nu_n))}{K_{A,IL}(\nu_n)} \quad \nu_n \ll \nu_{UG} \quad (5.38)$$

To determine the exact regimes in which Equation 5.37 and 5.38 were true, I placed known frequency noise signals on the master laser and monitored the error and actuator point signals. I found that Equation 5.37 was accurate at $\nu_n > \nu_{UG}$ and that Equation 5.38 was accurate for $\nu_n < \nu_{UG}$. Therefore these expressions can be rearranged into the same format as Equations 4.54 and 4.55 for the Fabry-Perot case.

$$[S_{f,s}(\nu_n) - S_{f,mCL}(\nu_n)]_{OpenLoop} = \begin{cases} N_{a,IL}(\nu_n) \cdot K_{A,IL}(\nu_n) & DC < \nu_n < \nu_{UG} \\ \frac{N_{e,IL}(\nu_n)}{K_{D,IL}(\nu_n)} & \nu_n > \nu_{UG} \end{cases} \quad (5.39)$$

$$[S_{f,s}(\nu_n) - S_{f,mCL}(\nu_n)]_{ClosedLoop} = \begin{cases} \frac{N_{e,IL}(\nu_n)}{K_{D,IL}(\nu_n)} & \nu_n \gg \nu_{UG}, \nu_n \ll \nu_{Lock} \end{cases} \quad (5.40)$$

Equations 5.39 and 5.40 are identical to Equations 3.21 and 3.22 (with $S_{f,Laser}$ and $S_{f,REF}$ replaced by $S_{f,s}$ and $S_{f,mCL}$ respectively). This suggests that the simple control loop of Figure 3.5 is adequate in describing the relative frequency stabilization of the slave laser with respect to the master laser. However, this simple control loop does not describe the closed loop spectral density of frequency noise of the injection-locked output, $S_{f,IL}$. The added complexity of Figure 5.4 is thus necessary to describe the entire injection-locking process. Using this control loop, one can solve for the relative frequency noise of the injection-locked output with respect to the master laser input, $S_{f,IL} - S_{f,mCL}$, well within the bandwidth of the control loop (where $K_{S,IL} \gg 1$), as shown in Equation 5.41.

$$S_{f,IL}(\nu_n) - S_{f,mCL}(\nu_n) = \left\{ \frac{N_{e,IL}(\nu_n)}{K_{D,IL}(\nu_n)} \cdot T_S(\nu_n) \quad \nu_n \ll \nu_{UG}, \nu_n \ll \nu_{Lock} \right\} \quad (5.41)$$

No further information can be obtained about the spectral density of frequency noise of the injection-locked output (with certainty) based only on the error and actuator point measurements of the PDH injection-locking experiment.

5.4 Measuring $K_{A,IL}$, $K_{D,IL}$, and ν_{Lock}

To measure the actuator and discriminator constants and the value of the lock range frequency we can sweep the resonant frequency of the slave resonator through the frequency of the master laser and its two sidebands by applying a voltage ramp to the Fast PZT of Figure 5.1. Derivation of the error signal for a discrete frequency sweep of the slave resonator reveals the exact same error signal dependence as that obtained for the master laser swept through the Fabry-Perot resonance of Figure 4.5. This time the x-axis can be converted to units of slave resonator pulled frequency, ν_{pull} , with the three peaks occurring at $\nu_m - \nu_p$, ν_m , and $\nu_m + \nu_p$. The same techniques and reasoning for the determination of K_A , K_D , and $\delta\nu/2$ in Section 4.3 can be used to determine $K_{A,IL}$, $K_{D,IL}$, and ν_{Lock} . Note that the full width of the central dispersive regime equals $2 \times \nu_{Lock}$.

Another method of determining ν_{Lock} is to measure K_A for the master or $K_{A,IL}$ for the slave resonator and place a known frequency noise ($S_{f,m}(\nu_n)$) on the master laser or slave resonator ($S_{f,s}(\nu_n)$) at a dither frequency, ν_n , outside the bandwidth of G_{OLIL} , while the slave laser is locked to the master laser. According to the discussion of Section 5.1, ν_{Lock} equals the maximum $S_{f,m}$ or $S_{f,s}$ placed on the laser without the slave losing lock.

According to the above analysis, the injection-locking frequency control loop only suppresses the noise contribution of the slave resonator. The limit of the spectral density of frequency noise of the injection-locked output is that of the master laser. To further improve the frequency stability of the high power injection-locked output we can implement one of three “global” feedback loops depicted in Figure 5.5. Two of the techniques, labeled Techniques 2 and 3 have been analyzed in the literature.²⁴



Technique 1 reduces the frequency noise of the incident master laser by prestabilizing its frequency to a reference. In Figure 5.5, a small portion of the master laser is reflected by mirror R_1 , passed through a phase modulator, $\phi M2$, and sent to the

Fabry-Perot resonator. The PDH error signal is detected in reflection at photodiode 2 (PD2), demodulated, amplified in the servo, and fed back to the master laser PZT (for “High” ν_n , i.e. $1 \text{ kHz} < \nu_n < \nu_{UG}$) and temperature controller (for “Low” ν_n , i.e. $DC < \nu_n < 1 \text{ kHz}$), as discussed in Chapter 3. This technique creates two independent control loops to eliminate the master laser and slave resonator frequency noise separately.

Technique 2 directs a portion of the injection-locked output to a frequency reference and sends the error frequency fluctuations back to the master laser. In Figure 5.5, a portion of the injection-locked field is directed by mirror, R_2 , through $\phi M2$ (after flipping the “Flip-up mirror” up into the beam path), to the Fabry-Perot. Again, the PDH error signal is obtained in reflection, demodulated, amplified in the servo and fed back to the master laser PZT (for “High” ν_n) and temperature controller (for “Low” ν_n). This technique detects the residual injection-locked frequency noise, $S_{f,IL}$ of Equation 5.30, and uses the master laser as the frequency actuator to eliminate both the incident master laser frequency noise and the residual frequency noise of the slave resonator.

A third option, denoted as Technique 3, is identical to Technique 2 in its detection of $S_{f,IL}$. However, the frequency noise in the regime $DC < \nu_n < \nu_{Lock}$ is fed back to the master laser and the noise in the regime $\nu_{Lock} < \nu_n < \nu_{UG}$ to an EOM in the path of the injection-locked output beam, $\phi M3$.

To compare the three techniques, I expand the injection-locking control loop of Figure 5.4 to establish effective control loops which accurately model the effects of the various optical and electronic components depicted in Figure 5.5. All of the control loops contain the injection-locking loop of Figure 5.4. Also, I designated a single master laser actuator transfer function, K_A , and a single servo transfer function K_S for Techniques 1

and 2. In actuality there may be several actuators (PZT, temperature controller, EOM, etc.) with different transfer functions and bandwidths, requiring one servo per actuator. I have also assumed comparable $S_{V,D}$ and $S_{V,S}$ for all detection schemes and servos.

The control loop of Technique 1 is established by sending the stabilized output of the master laser, $S_{f,mCL}$ of Figure 4.4, into the injection-locking control loop of Figure 5.5 and is shown in Figure 5.6.

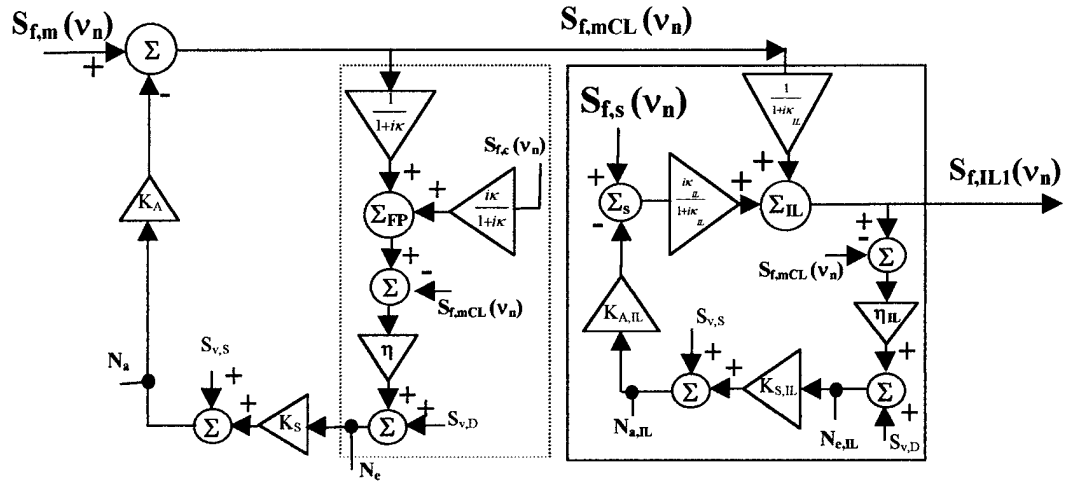


Figure 5.6. Technique 1 frequency noise control loop.

The resulting injection-locked closed loop spectral density of frequency noise of Technique 1, $S_{f,IL1}(v_n)$, is shown in Equation 5.42.

$$S_{f,IL1}(v_n) = \left\{ \begin{aligned} & \frac{\sqrt{(S_{f,s}(v_n))^2 - (K_{A,IL}(v_n) \cdot K_{S,IL}(v_n) \cdot S_{V,D})^2 - (K_{A,IL}(v_n) \cdot S_{V,S})^2}}{|1 + G_{OL,IL}(v_n)|} \cdot T_{S,CL}(v_n) \\ & + \frac{\sqrt{(S_{f,m}(v_n))^2 - (K_A(v_n) \cdot K_S(v_n) \cdot S_{V,D})^2 - (K_A(v_n) \cdot S_{V,S})^2}}{|1 + G_{OL}(v_n)|} \cdot T_{M,CL}(v_n) \\ & + S_{f,c}(v_n) \cdot \left| \frac{G_{OL}(v_n)}{1 + G_{OL}(v_n)} \right| \cdot T_{M,CL}(v_n) \end{aligned} \right\} \quad (5.42)$$

Figure 5.7 shows that, in Technique 2, the output of the PDH injection-locking control loop of Figure 5.4, given by Equation 5.30, is passed to the Fabry-Perot discriminator and the detected noise is sent back to the master laser.

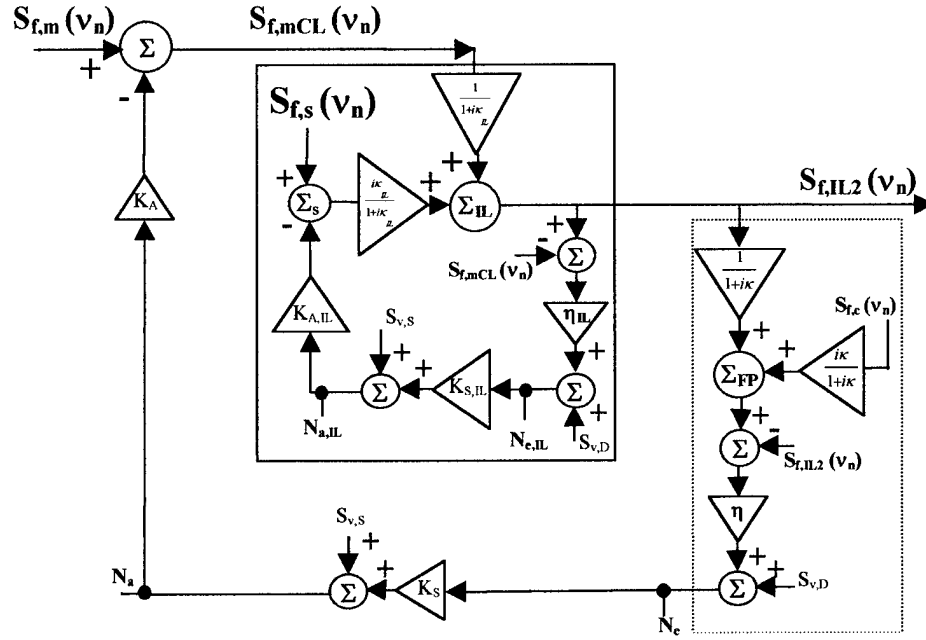


Figure 5.7. Technique 2 frequency noise control loop.

The closed loop spectral density of frequency noise of the injection-locked output of Technique 2, $S_{f,IL2}(v_n)$, is shown in Equation 5.43.

$$S_{f,IL2}(v_n) = \left\{ \begin{aligned} & \frac{\sqrt{(S_{f,s}(v_n))^2 - (K_{A,IL}(v_n) \cdot K_{S,IL}(v_n) \cdot S_{V,D})^2 - (K_{A,IL}(v_n) \cdot S_{V,S})^2}}{|1 + G_{OL,IL}(v_n)| \cdot |1 + G_{OL}(v_n) \cdot T_{M,CL}(v_n)|} \cdot T_{S,CL}(v_n) \\ & + \frac{\sqrt{(S_{f,m}(v_n))^2 - (K_A(v_n) \cdot K_S(v_n) \cdot S_{V,D})^2 - (K_A(v_n) \cdot S_{V,S})^2}}{|1 + G_{OL}(v_n) \cdot T_{M,CL}(v_n)|} \cdot T_{M,CL}(v_n) \\ & + S_{f,c}(v_n) \cdot \left| \frac{G_{OL}(v_n) \cdot T_{M,CL}(v_n)}{1 + G_{OL}(v_n) \cdot T_{M,CL}(v_n)} \right| \end{aligned} \right\} \quad (5.43)$$

Before introducing Technique 3, I will compare the results of Techniques 1 and 2. Recall that $T_{S,CL}(v_n)$ is a high pass filter of cut-off frequency, v_{Lock} , and that $T_{M,CL}(v_n)$ is equal to one where $G_{OL,IL}(v_n) \gg 1$ and is a low pass filter of cut-off frequency, v_{Lock} ,

where $G_{OL,IL}(v_n) \ll 1$. According to Equation 5.43, at v_n well within the bandwidth of G_{OL} and $G_{OL,IL}$, the noise contributions of the slave resonator are further reduced by a factor of $G_{OL}(v_n)$ in Technique 2 with respect to Technique 1. Outside the bandwidth of $G_{OL,IL}(v_n)$, the master laser transfer function $T_{M,CL}(v_n)$ reduces the effectiveness of Technique 2 in eliminating the noise contribution of the master laser noise for $v_n > v_{Lock}$, but this is in the regime where the slave resonator noise contributions are the dominant noise source anyway. Also, even the reduced open loop gain of Technique 2 always exceeds that of Technique 1 in reducing the slave resonator phase noise.

In the work of this thesis, the bandwidths of $G_{OL,IL}(v_n)$ and $G_{OL}(v_n)$ were limited by PZT resonances (to be nearly 25 kHz) and thus were both much less than v_{Lock} (~ 750 kHz). In this limiting case, the added noise reduction of the slave laser noise in Technique 2 with respect to Technique 1 occurs in the regime $v_n \ll v_{Lock}$ where the slave noise contributions are already reduced by the PDH injection-locking control loop, $G_{OL,IL}$, and the high pass filter, $T_{S,CL}$. In this situation, one would expect comparable closed loop injection-locked spectral density of frequency noise with the two techniques.

As discussed above, the open loop transfer function of Technique 2 is reduced in the regime $v_n \gg v_{Lock}$, by the low pass frequency noise transfer function of the master laser onto the injection-locked output ($T_{M,CL}(v_n)$). Therefore feeding back any high frequency signals ($v_n > v_{Lock}$) to the master laser does not make sense.

To improve the effectiveness of Technique 2, one splits the feedback loop into high ($v_n > v_{Lock}$) and low ($v_n < v_{Lock}$) frequency regimes, as done in Technique 3 of Figure 5.8.

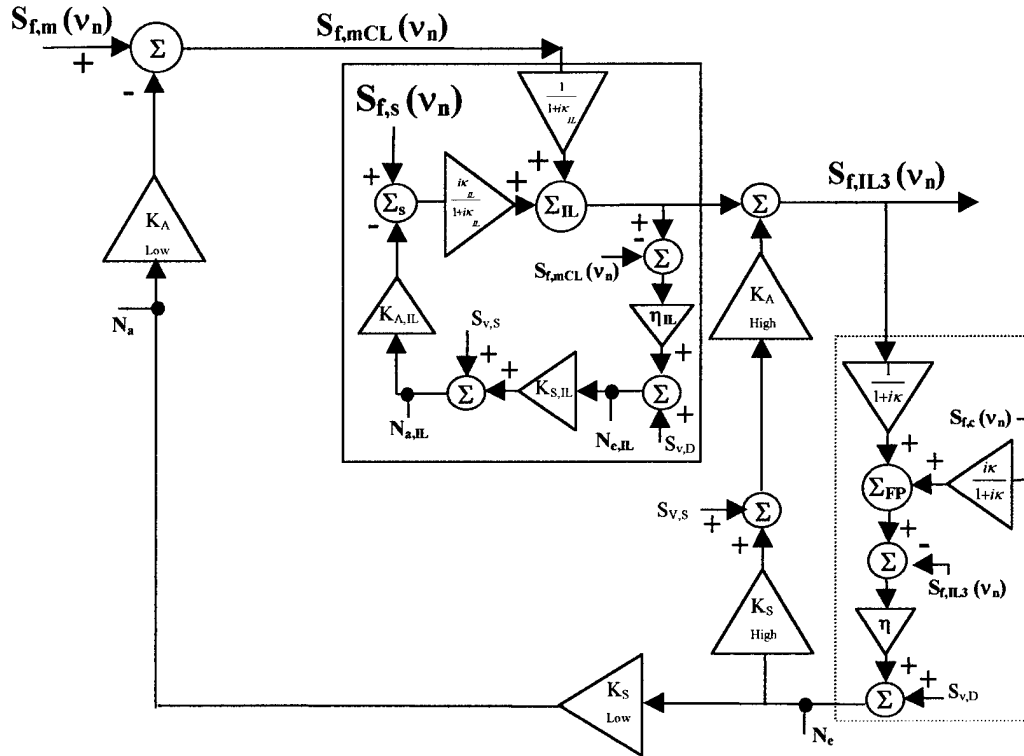


Figure 5.8. Technique 3 frequency noise control loop.

The low frequency noise is fed back to the master laser as in Technique 2, but the high frequency noise is fed back directly to the injection-locked output through the use of a phase modulator, $\phi M3$, with actuator response, $K_{A,High}$. As a result, the closed loop injection-locked spectral density of frequency noise, $S_{f,IL3}$, at $v_n < v_{Lock}$ is identical to that of Technique 2 (Equation 5.43 with G_{OL} replaced by $G_{OL,Low}$ defined in Equation 5.44).

$$G_{OL,Low}(v_n) = K_{A,Low}(v_n) \cdot K_{S,Low}(v_n) \cdot K_D(v_n) \quad (5.44)$$

At $v_n > v_{Lock}$, $S_{f,IL3}$ is given by Equation 5.45 in terms $G_{OL,High}$, defined in Equation 5.46.

$$S_{f,IL3}(v_n) = \left\{ \frac{\sqrt{(S_{f,s}(v_n))^2 + (K_{A,IL}(v_n) \cdot K_{S,IL}(v_n) \cdot S_{V,D})^2 + (K_{A,IL}(v_n) \cdot S_{V,S})^2}}{|1 + G_{OL,IL}(v_n)| \cdot |1 + G_{OL,High}(v_n)|} \cdot T_{S,CL}(v_n) + S_{f,c}(v_n) \cdot \left| \frac{G_{OL,High}(v_n)}{1 + G_{OL,High}(v_n)} \right| + \frac{S_{f,m}(v_n)}{|1 + G_{OL,High}(v_n) \cdot T_{M,CL}(v_n)|} \cdot T_{M,CL}(v_n) + \frac{\sqrt{(K_{A,High}(v_n) \cdot K_{S,High}(v_n) \cdot S_{V,D})^2 + (K_{A,High}(v_n) \cdot S_{V,S})^2}}{|1 + G_{OL,High}(v_n) \cdot T_{M,CL}(v_n)|} \right\} \quad (5.45)$$

$$G_{OL,High}(v_n) = K_{A,High}(v_n) \cdot K_{S,High}(v_n) \cdot K_D(v_n) \quad (5.46)$$

Note that both the master and slave noise contributions are reduced by a factor of $G_{OL,High}$, which is not attenuated by the factor of $T_{M,CL}(v_n)$ as it was in Technique 2.

5.6 Summary

In this chapter, I derived an explicit expression for the lock range frequency, accounting for the reduced power in the central carrier portion of the incident master laser field when using the PDH locking technique. This expression was not present in the literature and may have led to erroneous theoretical predictions of v_{Lock} in the literature.²⁴ Next, I derived, for the first time in the literature, the PDH injection-locking error signal, and showed that it was equally susceptible to master laser and slave resonator frequency noise. Comparison of the injection-locking analysis and that of the Fabry-Perot, of Chapter 4, revealed an apparent equivalence between $\delta v/2$ and v_{Lock} for these two seemingly unrelated processes. I also showed that the minimum spectral density of frequency noise of the injection-locked output is achieved by maximizing the power in the master laser PDH modulation sidebands, which is opposite to the case of locking a laser to a Fabry-Perot. I established a control loop describing the injection-locking process and showed it to necessarily be more complicated than Figure 3.5 to accurately model the entire injection-locking process. I expanded the loop to determine the closed loop spectral density of frequency noise of three global frequency stabilization schemes. Techniques 2 and 3 had been introduced in the literature, with slightly different noise control loop models, but only the open loop transfer functions were listed.²⁴ I also showed that while Technique 3 clearly yields the best theoretical results, there are circumstances in which Technique 2 yields only slightly better results than Technique 1, even though it is generally referred to in the literature as being the worst technique.

CHAPTER 6. Injection-Locking Experiments

In Chapter 5, I derived the PDH error signal and oriented the frequency noise control loop in such a manner that they accurately modeled the various measurements that I performed over the course of this effort. In this chapter, I review these measurements and then compare the experimental results obtained when implementing Techniques 1 and 2 to reduce the frequency noise of a particular injection-locked laser.

Figure 6.1 displays the elaborate optical set-up remaining after all of the experiments were performed, including the experiment to compare the results of two global stabilization schemes (Techniques 1 and 2 of Chapter 5). I refer to this figure, throughout this chapter as I discuss the various measurements that led up to the final experimental comparison of Techniques 1 and 2. Since the set-up was quite elaborate, employing several control loops and various pieces of equipment, I worked with Mr. Joshua Bienfang on several of the experiments described below.⁴⁹

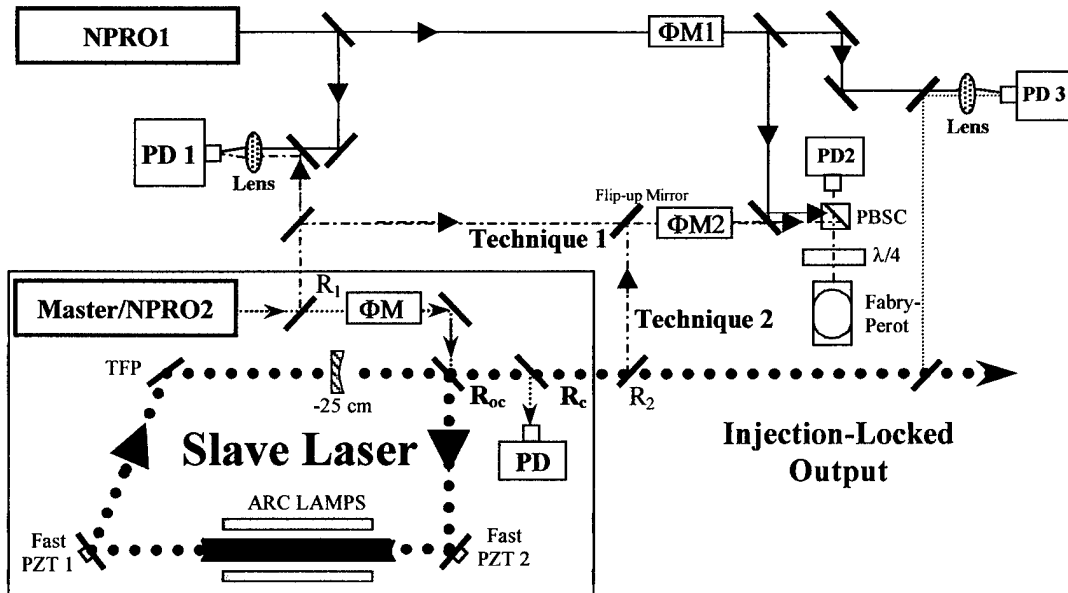


Figure 6.1. Optical schematic of injection-locking frequency stabilization experiments.

The Coherent Head, described in Chapter 2, was placed in a ring resonator and injection-locked with NPRO 2, as shown within the solid box of this figure. The pertinent parameters of the injection-locking experiments were: $T_{oc} = 15\%$, $FSR \sim 300$ MHz, $\beta \sim 1.08$, $\nu_p = 18$ MHz, $P_m = 310$ mW, and $P_{IL} = 22$ W. The phase noise of the slave resonator with respect to NRPO 2 was detected and reduced using the PDH injection-locking scheme by feeding back to Fast PZT 1 of the slave resonator.

6.1 Measuring $K_{A,IL}$, $K_{D,IL}$, and ν_{Lock} and determining PDH error signal is equally susceptible to master and slave laser frequency noise

I followed the procedure outlined in Section 5.4 to measure $K_{A,IL}$ and $K_{D,IL}$ of the PDH injection-locking loop several times over the course of this effort. Common values of $K_{A,IL}$ and $K_{D,IL}$ were 75 MHz/V, and 0.1 V/MHz, respectively. A portion of NPRO2 was directed by mirror R_1 through a phase modulator, $\phi M2$, to the Fabry-Perot, as shown for Technique 1 in Figure 6.1. The actuator coefficient of NPRO2, K_{A2} , was measured to be 5.31 MHz/V by dithering the NPRO PZT and monitoring the error signal obtained at PD2 as discussed in Section 4.3. I measured ν_{Lock} for various values of P_m and P_{IL} by measuring the width of the central dispersive regime of the error signal and by injecting frequency noise on the master laser or slave resonator until the slave laser lost lock.

To determine the frequency noise that caused the slave to lose lock to the master, I mounted a second PZT, Fast PZT 2, with a bandwidth of ~ 50 kHz, to a slave resonator mirror and measured its actuator coefficient, $K_{A,IL2}$, to be 50 MHz/V. The actuator and discriminator coefficients, $K_{A,IL1}$ and $K_{D,IL1}$, of the injection-locking PDH loop containing Fast PZT 1 were measured to be 50 MHz/V and 0.1 V/MHz. With the slave resonator locked to the NPRO2 using Fast PZT 1, I applied a sinusoidal voltage signal (of amplitude, V_{Sig} , and frequency $\nu_n \gg \nu_{UG}$) to either Fast PZT 2 or the Fast PZT of NPRO2

and monitored the spectral density of voltage noise, at the $N_{e,IL}$ point (the input of the servo), of the control loop containing Fast PZT 1. The magnitude of the frequency dither, $S_{f,m}(v_n)$ or $S_{f,s}(v_n)$ in Hz, is equal to the product of V_{Sig} and K_{A2} or $K_{A,IL2}$, respectively. By applying various signals to Fast PZT 2 and the Fast PZT of NPRO2, I verified that Equation 6.1 was valid for $v_n > v_{UG}$ and Equation 6.2 was valid at $v_n < v_{UG}$.

$$N_{a,IL} = V_{Sig} \cdot \frac{K_{A2}}{K_{A,IL1}} \quad \text{OR} \quad N_{a,IL} = V_{Sig} \cdot \frac{K_{A,IL2}}{K_{A,IL1}} \quad (6.1)$$

$$N_{e,IL} = V_{Sig} \cdot K_{A2} \cdot K_{D,IL1} \quad \text{OR} \quad N_{e,IL} = V_{Sig} \cdot K_{A,IL2} \cdot K_{D,IL1} \quad (6.2)$$

This showed that the injection-locking control loop was equally susceptible to the frequency noise of the master laser and slave resonator in agreement with Equations 5.27, 5.37, and 5.38 of the previous chapter.

I measured v_{Lock} with this same experiment by increasing V_{Sig} until the slave laser lost lock and recording the highest $S_{f,m}$ or $S_{f,s}$ achievable before the laser lost lock. However, this value varied by as much as 500 kHz between measurements performed at the same v_n or when varying v_n . Since v_n was limited to 50 kHz, only 40 kHz outside the bandwidth of the PDH injection-locking control loop, I was unable to verify if this was an inaccurate measurement scheme or if it was hampered in my particular case by the PDH feedback loop. However, the only group to report using this method stated that their measurements were generally off by a factor of 2 (several hundred kHz) from the predicted value.²⁴ It is unclear if their error was caused by a lack of accounting for the reduced master laser seed power (proportional to $J_0(\beta)$ as shown in Equation 5.15) when employing a PDH technique or if the measurement itself is a poor indicator of v_{Lock} .

I also used the error signal method for determining ν_{Lock} several times over the course of these efforts and not only found the measurement to be much simpler and faster than the method discussed above, but also relatively precise and accurate. Table 6.1 displays the results of measurements taken while varying P_m and P_{IL} and compares the results to the predictions of Equation 5.15.

P_m (mW)	P_{IL} (W)	ν_{Lock} Predicted (kHz)	ν_{Lock} Measured (kHz)	Meas.-Pred. (kHz)
155	21.3	437.778	459.5	21.722
155	21.3	437.778	435.0	-2.778
155	21.3	437.778	456.5	18.722
310	19.3	650.346	750.0	99.653
310	19.6	645.907	563.5	-82.407
310	20.67	629.017	605.0	-24.017
310	21.33	619.111	715.0	95.888
310	22.53	602.400	580.0	22.4

Table 6.1. Measurements of ν_{Lock} using error signal.

The first three rows of the table display the repeatability of this measurement, with changes in ν_{Lock} of less than 22 kHz between measurements. All entries in the table display good agreement between the predicted and measured values of ν_{Lock} , and show that generally the difference between the two was less than 100 kHz and was often less than 25 kHz.

6.2 Verifying master laser and slave resonator frequency noise transfer functions

Although the injection-locking PDH discrimination method is equally susceptible to master laser and slave resonator frequency noise, the injection-locked output is more susceptible to master laser noise at $\nu_n \ll \nu_{\text{Lock}}$ as predicted by Equation 5.20. In this section, I discuss the methods I developed to verify the frequency noise transfer functions of the master and slave laser since such techniques can also be used to verify the transfer functions of other complex processes (such as the frequency doubler of Chapter 7). To

verify the transfer function of the slave laser frequency noise onto the injection-locked output, the master laser (NPRO2) was prestabilized to the Fabry-Perot using Technique 1 (of Figure 6.1) and the slave laser was locked to the master using Fast PZT 1. A second NPRO (NPRO1 of Figure 6.1) was stabilized to an adjacent longitudinal mode of the same Fabry-Perot at a frequency, ν_{FSR} , away from NPRO2. A portion of the injection-locked output, E_{IL} , and NPRO1, E_{REF} , were mode-matched to a common spatial mode and mixed onto a photodiode, PD3. If we neglect the master laser modulation sidebands of Equation 5.22, then the field incident on PD3 varies as shown in Equation 6.3.

$$E_{PD3} \propto E_{IL} \cdot e^{i\omega_m t} \cdot e^{i \cdot \text{Re}[-iS_{\phi,IL} \cdot e^{i\omega_n t}]} + E_{REF} \cdot e^{i(\omega_m - \omega_{FSR})t} \cdot e^{i \cdot \text{Re}[-iS_{\phi,REF} \cdot e^{i\omega_n t}]} \quad (6.3)$$

Since NPRO1 was stabilized to the Fabry-Perot, we can assume $S_{\phi,REF} \ll S_{\phi,IL}$. The detector signal obtained near ν_{FSR} can be shown to equal Equation 6.4.

$$V_{PD3} \propto 2 \cdot R_{esp} \cdot G_v \cdot \sqrt{P_{IL} \cdot P_{REF}} \cdot \frac{S_{f,IL}(\nu_n)}{\nu_n} \cdot \sin(\omega_n t) \cdot \sin(\omega_{FSR} t) \quad (6.4)$$

The ratio of the voltage signal at $\nu_{FSR} + \nu_n$ to the signal at ν_{FSR} is given by Equation 6.5.

$$\frac{V_{PD3}(\nu_{FSR} \pm \nu_n)}{V_{PD3}(\nu_{FSR})} = \frac{S_{f,IL}(\nu_n)}{\nu_n} \quad (6.5)$$

Equation 6.5 suggests that the ratio of the detected noise sideband to the carrier signal at ν_{FSR} can be used to determine $S_{f,IL}$. I applied sinusoidal signals, V_{Sig} to Fast PZT 2 ($K_{A,IL2} = 50 \text{ MHz/V}$) and compared the predicted value of Equation 5.20, shown in Equation 6.6, to the value found by measuring the signals at ν_{FSR} and $\nu_{FSR} + \nu_n$ and using Equation 6.5.

$$S_{f,IL}(\nu_n) = S_{f,s}(\nu_n) \cdot |T_s(\nu_n)| = V_{Sig}(\nu_n) \cdot K_{A,IL2} \cdot \frac{\nu_n / \nu_{Lock}}{\sqrt{1 + \left(\nu_n / \nu_{Lock}\right)^2}} \quad (6.6)$$

I measured ν_{Lock} to be ~ 1 MHz and applied signals of amplitude 0.1 mV and 1 mV to Fast PZT 2 at ν_n of 10, 15, 19, 25, and 30 kHz. The results of the various measurements are shown in Figure 6.2.

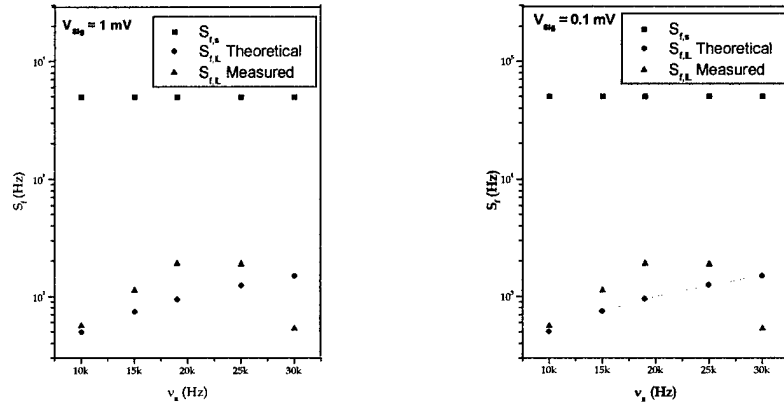


Figure 6.2. Verification of slave resonator frequency noise transfer function, $T_s(\nu_n)$.

The theoretical values of Equation 6.6 are connected with a dotted line. Figure 6.2 shows that the spectral density of frequency noise of the injection-locked output, $S_{f,IL}$, determined from the ratio of the measurements (Equation 6.5) agrees enough with the predicted value of Equation 6.6 to suggest the slave resonator frequency noise, $S_{f,s}$, is reduced at $\nu_n \ll \nu_{\text{Lock}}$ by the factor $T_s(\nu_n)$. For comparison, I plotted the injected $S_{f,s}$ on the same plot to show that there is clearly a factor of a hundred reduction from the injected $S_{f,s}$ and the $S_{f,IL}$ measured. The limited bandwidth of the Fast PZT actuator made further measurements to check the entire transfer function, $T_s(\nu_n)$, at higher ν_n , impossible. Also, I did not check the transfer function of the master laser, $T_m(\nu_n)$, since I used its Fast PZT to maintain lock with the Fabry-Perot. In retrospect, I could have performed this measurement by placing a summing circuit on the Fast PZT input of NPRO2 and adding a noise signal to the feedback actuator signal from the servo.

Another, perhaps more straightforward method of verifying Equation 5.20, would be to lock the lasers using Technique 2 and place known noise signals on Fast PZT 2

($S_{f,s}$) and the Fast PZT of NPRO2 ($S_{f,m}$) with the summing circuit. If we place noise signals on these lasers outside the bandwidth of G_{OL} and $G_{OL,IL}$ then the injection-locked signal of Equation 5.43 simplifies in this regime ($\nu_n \gg \nu_{UG}$ of both loops) to:

$$S_{f,IL2}(\nu_n) = \{S_{f,s}(\nu_n) \cdot T_S(\nu_n) + S_{f,m}(\nu_n) \cdot T_M(\nu_n)\} \quad (6.7)$$

Tracing this signal clockwise through the Fabry-Perot discriminator of the frequency noise control loop diagram (Figure 5.7), with discriminator constant K_{D2} , yields the following expression for the N_e point measurement in this regime. I have neglected the contributions of the discriminator noise, $S_{V,D}$, and Fabry-Perot frequency noise, $S_{f,c}$.

$$N_e(\nu_n) = K_{D2}(\nu_n) \cdot \{S_{f,s}(\nu_n) \cdot T_S(\nu_n) + S_{f,m}(\nu_n) \cdot T_M(\nu_n)\} \quad (6.8)$$

The ratio of N_e to K_{D2} yields the product of $S_{f,m}$, or $S_{f,s}$ and their transfer functions. I did not perform this experiment since I thought of it long after I completed the last injection-locking experiment, but I discuss it here since I did use this same method to verify the frequency noise transfer functions of the external-cavity frequency doubled laser.

6.3 PDH Injection-locking Stabilization Results

Equations 5.39 and 5.40 display the relationship between the relative frequency noise of the slave laser, $S_{f,s}$, and that of the incident master laser, $S_{f,m}$, and the voltage measurements made at the entrance, $N_{e,IL}$, and exit, $N_{a,IL}$, of the servo in the PDH injection-locking experiment. I measured the spectral density of voltage noise at $N_{e,IL}$ and $N_{a,IL}$, the actuator coefficient, $K_{A,IL}$, and the discriminator coefficient, $K_{D,IL}$, various times over the course of this effort. Figure 6.3 displays the most common results obtained for the open and closed loop relative frequency stability of the slave laser with respect to the master laser. This figure shows that as a result of the PDH injection-locking control loop, the frequency noise of the slave laser with respect to the master

laser was generally reduced to $\sim 10 \text{ Hz/Hz}^{1/2}$ out to 100 Hz. I have also plotted the value of the lock range frequency, ν_{Lock} .

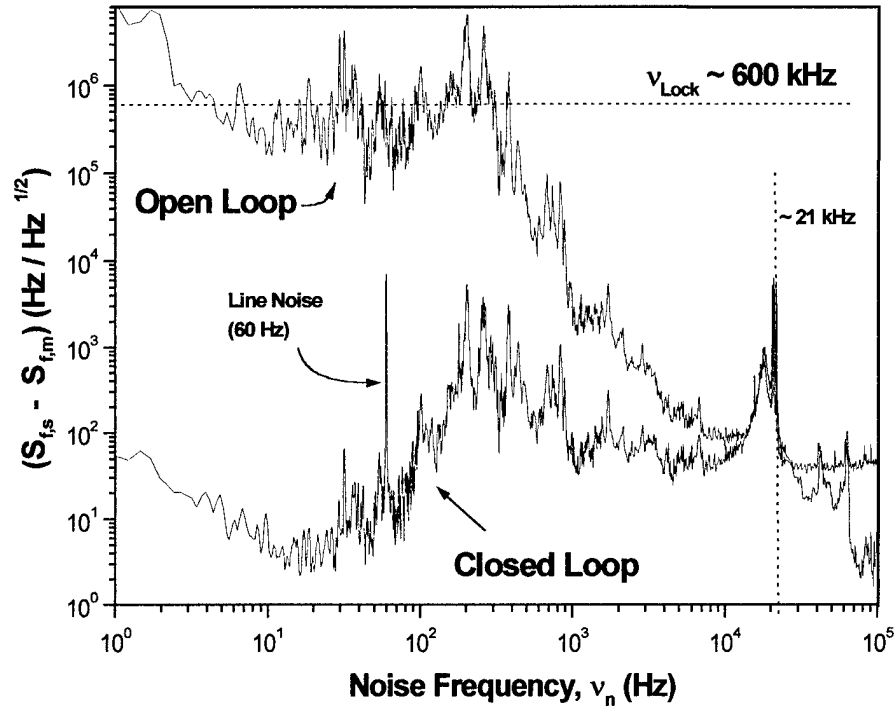


Figure 6.3. Relative frequency noise of the slave with respect to the master.

Notice that the open loop spectral density of frequency noise of the slave laser with respect to the master laser was greater than ν_{Lock} at various noise frequencies. This explains why I was unable to passively injection-lock this system and keep the slave laser locked to master. Thus, the PDH control loop was required to keep the slave laser oscillation frequency locked to that of the incident master laser.

6.4 Comparing Techniques 1 and 2

The theory of Sections 5.1-5.4 was constructed based on the measurements discussed in Sections 6.1 and 6.2. To test the theoretical predictions of Section 5.5, I compared the closed loop injection-locked spectral density of frequency noise obtained

when implementing Techniques 1 and 2. I did not test Technique 3, since I did not have a phase modulator that could withstand the 20+Watt injection-locked output power.

The slave laser was injection-locked to NPRO2 and the frequency noise contribution of the slave resonator onto the injection-locked output was further reduced by implementing a PDH locking scheme, feeding back to Fast PZT 1. Technique 1, prestabilizing the master laser, was accomplished by removing the “Flip-up Mirror” of Figure 6.1 and blocking the low power beam of Technique 2. Technique 2, detecting $S_{\text{f,IL}}$ and feeding it back to the master, was accomplished by replacing the “Flip-up Mirror” and blocking the low power beam of Technique 1.

To compare the closed loop spectral density of frequency noise of the injection-locked output of Techniques 1 and 2, a second NPRO, labeled NPRO1, was stabilized to an adjacent mode of the Fabry-Perot resonator of Figure 6.1. This laser was used as a reference to obtain heterodyne beatnote measurements with a portion of the stabilized injection-locked output at photodiode 3, PD3. For comparison, the linewidth and the Root Allan Variance (RAV) of the heterodyne beatnote signal were measured. The linewidth and RAV of the heterodyne beatnote between the stabilized master laser and the reference laser were also measured, at PD1, to determine the lower bound of the linewidth and RAV data.

The RAV is a measure of the frequency stability of the beatnote in the time domain and is obtained by recording N consecutive frequency measurements at a given time interval, τ , and inserting the results into the following expression.⁵²

$$\sigma(\tau) = \frac{1}{\nu_0} \cdot \sqrt{\frac{\sum_{k=1}^{N-1} (f_{k+1} - f_k)^2}{2 \cdot (N-1)}} \quad (6.9)$$

Where f_k refers to the frequency of the k^{th} measurement of the instantaneous beatnote frequency and ν_0 is the nominal frequency of the laser(s) being analyzed (e.g. $\sim 10^{14}$). By varying the time interval one can measure $\sigma(\tau)$ for various values of τ and plot the results.

Figure 6.4 displays the RAV and Table 6.2 the linewidth of the three beatnote measurements taken.

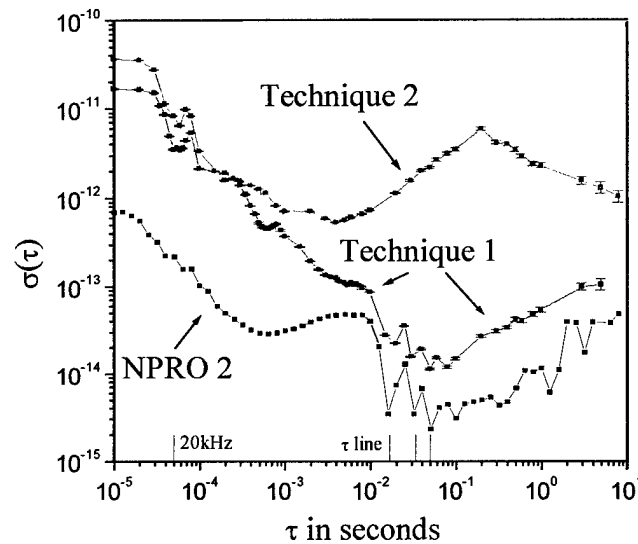


Figure 6.4. Root Allan Variance comparison of Techniques 1 and 2.

	Technique 1 (Master Laser Prestabilized)	Technique 2 (S_{IL} sent to Master)
Master (NPRO 2)	600 mHz	750 Hz
Injection-Locked Laser	1.6 Hz	781 Hz

Table 6.2. Comparison of beatnote linewidths.

When stabilizing the two NPROs alone to adjacent modes of the Fabry-Perot cavity, both lasers exhibited shot noise limited frequency noise spectral densities out to about 1 kHz, measured at N_e of their respective loops. Each exhibited a minimum RAV of 2.2×10^{-15} for a measurement interval of 50 msec (see Figure 6.4), and yielded a heterodyne beatnote linewidth of ~ 600 mHz, see Table 6.2. These results are typical for NPRO lasers and demonstrate their inherent stability.¹³

For Technique 1, heterodyne detection of a 24-W beam showed a minimum RAV of 10^{-14} for a measurement time of 50 msec, and a beatnote linewidth of nearly 1.6 Hz.

Surprisingly, Technique 2 yielded relatively poor frequency stability, despite the added reduction of the slave resonator phase noise predicted in Equation 5.43.

Heterodyne detection yielded a RAV of 5×10^{-13} for a measurement time of 4 msec, and a beatnote linewidth of ~ 780 Hz. The RAV shows that the spectral density of phase noise rises sharply at frequencies below 100 Hz, peaking near 5 Hz. This may be caused by strong low-frequency amplitude fluctuations in the PDH error signal caused by moderate pointing instability in the high-power output field. The strong amplitude fluctuations cause a consequent amplitude modulation of the Fabry-Perot reflected field (the second term of $S_{A,r}$ of Equation 4.29) and can be shown to modulate K_D as the amplitude modulation depth reaches a few percent or higher of the total output amplitude. Thus, incorrect frequency corrections are imposed on the laser system, raising the overall noise floor over the ideal case of a shot-noise-limited frequency noise floor.

In all experiments with the high-power laser, the switching frequency of the power supply of the arc-lamps, at nearly 20 kHz, was apparent as a FM modulation on the injection-locking PDH error signal. This was determined to arise from inadequate electrical shielding, rather than AM to FM coupling. Line noise at 60 Hz was also evident and its associated value of τ , labeled “ τ line”, is shown in Figure 6.4.

I also measured the closed loop spectral density of frequency noise of the injection-locked output of Technique 2 by dividing the N_e point signal of NPRO2 (the master laser) by the Fabry-Perot discriminator constant ($K_{D2} = 2$ V/MHz). The result is

shown in Figure 6.5. I have assumed that the frequency noise contribution of the Fabry-Perot ($S_{f,c}$) is negligible.

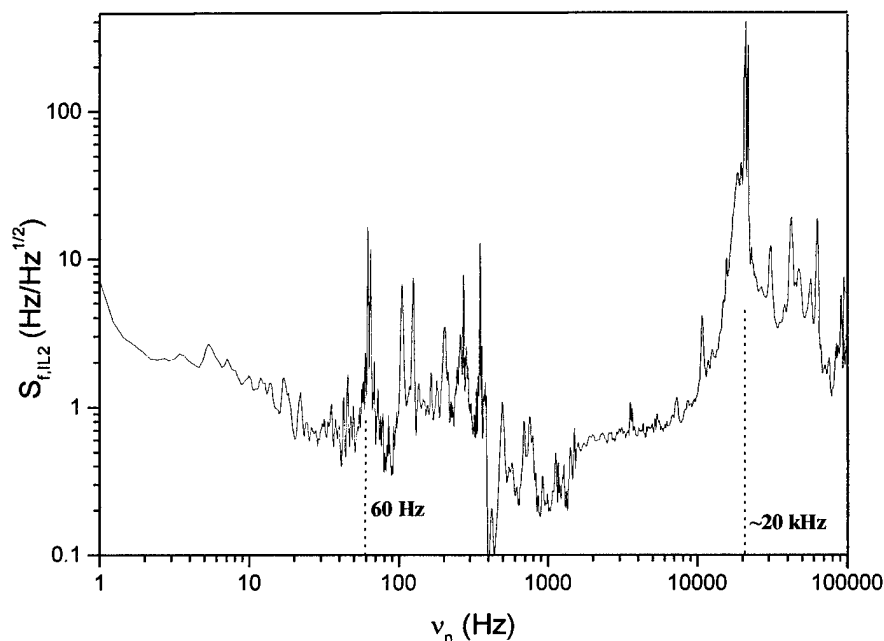


Figure 6.5. Injection-locked spectral density of frequency noise (Technique 2).

I have labeled the line noise at 60 Hz and lamp power supply noise at 20 kHz. I do not report $S_{f,IL}$ of Technique 1, since I had no accurate way of measuring it. I show this plot only to demonstrate that even the results of Technique 2 show an $S_{f,IL}$ of nearly 1 $\text{Hz/Hz}^{1/2}$ out to nearly 10 kHz. One would expect (based on the time domain measurements of Figure 6.4) that the frequency noise of the injection-locked output of Technique 1 was even better.

6.5 Summary

The measurements described in Sections 6.1 and 6.2 were used to generate much of the theory presented in Chapter 5. While feeding back the frequency noise of the injection-locked laser to the master laser yields the best theoretical closed loop spectral density of frequency noise, prestabilizing the master laser prevailed as the better experimental technique since it was less susceptible to pointing instability and amplitude

fluctuations of the injection-locked laser. By prestabilizing the frequency of the master laser, I obtained a cw, linearly polarized (97:1), 24-W output, with an M^2 of 1.07, a linewidth of 1.6 Hz, and a frequency stability of less than $1 \text{ Hz/Hz}^{1/2}$ out to nearly 10 kHz. This injection-locked output represents an increase in the power of the stable low-power seed oscillator by a factor of 60, while increasing the bandwidth by only a factor of 3.

For comparison purposes, the noteworthy injection-locked results of the literature are a 20-W output with a linewidth of 10 kHz,¹⁴ a 10-W output with a frequency stability of $50 \text{ Hz/Hz}^{1/2}$ at 300 Hz,¹⁵ and a 2.2 W output with a frequency stability of $2 \times 10^{-4} \text{ Hz/Hz}^{1/2}$ at 1 kHz.¹⁶ All of these efforts reported using Technique 2 (detecting the injection-locked frequency noise and using the master laser as the frequency actuator) and "less noisy" diode-pumped heads.

CHAPTER 7. The Frequency-Doubler

In this chapter, I review my attempts to characterize and improve the frequency stability of the external cavity frequency-doubled NPRO that I used to establish an in-lab frequency reference, discussed in Chapter 8. I analyze the control loop established in such an experiment in a manner analogous to the loops presented in Chapters 4 and 5. I list the theoretical results of this analysis and compare them with the results of the injection-locking control loop for the sake of drawing similar conclusions regarding the optimal stabilization of the frequency-doubled NPRO. Finally, I list the results of experiments performed to test the frequency noise transfer functions of the doubler cavity and the incident laser onto the output frequency-doubled field.

7.1 Doubler Cavity Frequency Noise Transfer Functions

To lock the resonant frequency of the doubler cavity to the instantaneous incident frequency of a Lightwave Electronics Model 126, 500 mW, NPRO laser, I employed the Hansch-Coulliard locking scheme,⁴⁵ shown in Figure 7.1.

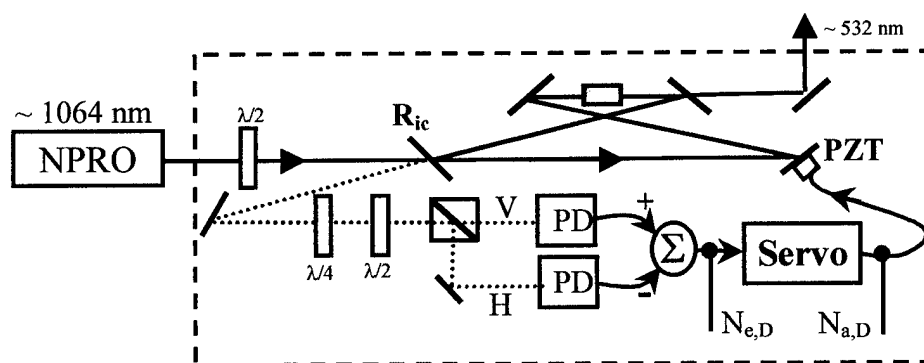


Figure 7.1. Frequency Doubler.

The nonlinear crystal is a MgO:LiNbO_3 crystal, temperature tuned to $\sim 110^\circ\text{C}$ to satisfy the Type II phase matching condition.⁵³ This locking technique takes advantage of the birefringent nature of the nonlinear crystal placed within the cavity and obtains an

error signal by comparing the reflected (non-resonant) horizontally polarized field (denoted with an H) with the reflected portion of the resonant vertically polarized field (denoted with a V). Since the technique is well documented in the literature, I will focus only on determining the frequency noise transfer functions.

Assume that the bow-tie cavity is configured such that the pump field is resonant and the generated visible field perfectly couples out of the resonator. To determine the frequency noise of the output visible field we break the problem up into two steps. First, we can determine the frequency noise transfer functions of the incident field and the doubler length fluctuations onto the circulating pump field using the damped, driven wave equation. Second, we can solve the wave equation for the visible field, with the pump field driving term, to determine the output visible field frequency noise.

We know from Chapter 4 that the frequency noise transfer function of the incident laser field onto the circulating field of the cavity is a low pass filter of corner frequency $\delta\nu/2$ and that of the cavity length fluctuations was a high pass filter of similar corner frequency. We expect then that the only thing to change in this discussion is the value of $\delta\nu/2$. Or in the time domain, we expect the only change to be the photon lifetime of the cavity, τ_p .

The bow-tie ring cavity consists of four mirrors. The reflectivity of the input coupler, R_{ic} , is 95% and the reflectivity of the other three mirrors is assumed to be ~ 1 (at $1.064 \mu\text{m}$). Therefore the chief contributing losses of the resonant pump field are the leakage through the input coupler and the absorption of the pump field in the nonlinear crystal. The circulating pump field experiences a total energy decay rate, γ_c , equal to the sum of the decay rates due to absorption, γ_0 , and transmission through the input/output

coupler, γ_e . These decay rates are defined below in terms of the circulating field round trip time, T , the speed of light, c , and the total cavity length, L .

$$\gamma_c = \gamma_0 + \gamma_e = 2\alpha_0 c + \frac{1}{T} \cdot \ln\left(\frac{1}{R_{ic}}\right) \quad (7.1)$$

$$T = \frac{1}{FSR} \approx \frac{L}{c} \quad (7.2)$$

Assume that the incident field is mode-matched to a longitudinal mode of the cavity, and that the resonator is impedance matched (i.e. $\gamma_e = \gamma_0$), so that all of the vertically polarized field is coupled into the resonator. The damped, driven wave equation for the circulating pump field, E_c , is shown in Equation 7.5 in terms of the vertically polarized portion of the incident laser field, $E_{inc}(V)$, defined in Equation 7.6.

$$\frac{d^2 \tilde{E}_c}{dt^2} + \gamma_c \cdot \frac{d \tilde{E}_c}{dt} + (\omega_c)^2 \cdot \tilde{E}_c = \sqrt{\frac{8 \cdot \gamma_e}{\epsilon \cdot V_c}} \cdot \frac{d}{dt} \left[\tilde{E}_{inc}(V) \right] - \frac{1}{\epsilon} \cdot \frac{d^2}{dt^2} \cdot \tilde{P} \quad (7.5)$$

Where, as in Chapter 4, the incident field is represented as shown in Equation 7.6.

$$\tilde{E}_{inc} = E_0 \cdot e^{i\omega_m t} \cdot e^{iS_{\phi,m} \sin(\omega_n t)} \left(\rho_V \cdot \hat{n}_V + \rho_H \cdot \hat{n}_H \right) = \tilde{E}_{inc}(V) + \tilde{E}_{inc}(H) \quad (7.6)$$

Note that ρ_V is the vertically polarized portion of the incident field and ρ_H is the horizontally polarized portion.

Equation 7.5 can be solved in a manner similar to that done for the injection-locked wave equation of Chapter 5, to yield the following circulating infra-red pump field, E_c , with phase noise, $S_{\phi,IR}$.

$$\tilde{E}_c = E_c \cdot e^{i\omega_m t} \cdot e^{i \text{Re}[-iS_{\phi,IR} \sin(\omega_n t)]} \quad (7.7)$$

The phase noise transfer functions of the incident laser, $S_{\phi,m}$, and those caused by the doubler cavity length fluctuations, $S_{\phi,c}$, onto the circulating field, $S_{\phi,IR}$, are shown in Equation 7.8, in terms of the variable s (defined as $i\omega_n$) and the variable κ defined in Equation 7.9.

$$S_{\phi,IR} = \left[\frac{s}{s + \frac{\gamma_c}{2}} \right] \cdot S_{\phi,c} + \left[\frac{\frac{\gamma_c}{2}}{s + \frac{\gamma_c}{2}} \right] \cdot S_{\phi,m} = \left[\frac{i \cdot \kappa}{1 + i \cdot \kappa} \right] \cdot S_{\phi,c} + \left[\frac{1}{1 + i \cdot \kappa} \right] \cdot S_{\phi,m} \quad (7.8)$$

$$\kappa = \frac{\omega_n}{\frac{\gamma_c}{2}} = \frac{v_n}{\frac{\delta v_c}{2}} \quad (7.9)$$

Equation 7.7 and 7.8 reveal explicit expressions for the circulating infra-red pump field that is resonant in the doubler cavity for a time period equal to τ_p proportional to $1/(\delta v_c/2)$. This field is then assumed to seed the nonlinear process within the crystal. Assume that the pump and generated fields are perfectly phase matched and that none of the generated visible field completes a round trip in the bow-tie cavity to seed the nonlinear process at the entrance of the crystal. The nonlinear, second order, polarization driving term, generated by the field of Equation 7.7, can be simplified to that shown in Equation 7.10 in terms of the second order susceptibility at $2\omega_m$, $\chi^{(2)}(2\omega_m)$.⁵³

$$\tilde{P}^{(2)} = \chi^{(2)}(2\omega_m) \cdot \tilde{E}_c^2 \propto e^{2i\omega_m t} \cdot e^{2i\text{Re}[-i \cdot S_{\phi,IR} \sin(\omega_n t)]} \quad (7.10)$$

Since this term is the source term in the wave equation describing the generated visible field, we can assume that the output frequency-doubled electric field oscillates in phase with this driving term and can be represented as shown in Equation 7.11.

$$\tilde{E}_{VTS} = E_{VTS} \cdot e^{2i\omega_m t} \cdot e^{i\text{Re}[-i \cdot S_{\phi,VTS} \sin(\omega_n t)]} \quad (7.11)$$

Where the phase noise of the output visible field, $S_{\phi, \text{VIS}}$, is defined to be twice that of the circulating infra-red field, $S_{\phi, \text{IR}}$, of Equation 7.10.

According to the above discussion the phase, and hence frequency, noise transfer functions of the incident laser and the doubler cavity onto the output visible electric field frequency noise are shown in Equation 7.12.

$$S_{f, \text{VIS}} = 2 \cdot \left(\left[\frac{i \cdot \kappa}{1 + i \cdot \kappa} \right] \cdot S_{f, c} + \left[\frac{1}{1 + i \cdot \kappa} \right] \cdot S_{f, m} \right) \quad (7.12)$$

The effective frequency noise control loop representing the frequency-doubling process is shown in Figure 7.2.

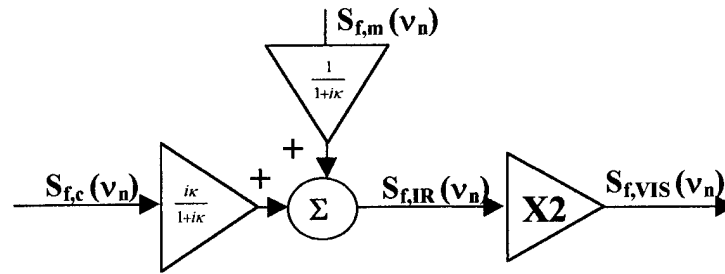


Figure 7.2. Frequency noise transfer functions of the frequency-doubler.

As discussed above, the frequency noise of the circulating infra-red field, $S_{f, \text{IR}}$, is the sum of the contributions from the incident laser, $S_{f, m}$, and those caused by cavity length fluctuations, $S_{f, c}$, each multiplied by their respective transfer functions. The infra-red field is then frequency doubled in the crystal, represented by X2, yielding the output visible frequency noise, $S_{f, \text{VIS}}$.

The Hansch-Couillard frequency discrimination technique detects the relative frequency noise of the circulating infra-red field with respect to the frequency noise of the incident field by subtracting the vertically polarized leakage field (with phase noise $S_{\phi, \text{IR}}$) with that of the reflected horizontally polarized field (with phase noise $S_{\phi, m}$). The

discriminator voltage output, V_{sig} , is shown in Equation 7.13 in terms of the discriminator coefficient, $K_{D,D}$ of Equation 7.14, and the variable η_D of Equation 7.15

$$V_{sig} = K_{D,D} \cdot (S_{f,c} - S_{f,m}) \quad (7.13)$$

$$K_{D,D} = \eta_D \cdot \left(\frac{i\kappa}{1+i\kappa} \right) \quad (7.14)$$

$$\eta_D = \frac{R_{esp} \cdot G_V \cdot P_{inc} \cdot \sin(2 \cdot \theta_1)}{\nu_n} \quad (7.15)$$

Where θ_1 is the angle between the incident laser field's polarization axis and the pump axis of the nonlinear crystal (the vertical axis in this case), and P_{inc} is the total incident power on the doubler cavity. Equation 7.15 shows that the discriminator slope is maximized when the incident field's polarization is rotated 45° from the pump axis of the crystal. Since this also reduces the pump field and the generated visible field amplitude, I often set $\theta_1 \sim 5^\circ$. Figure 7.3 displays the effective control loop of this locking technique.

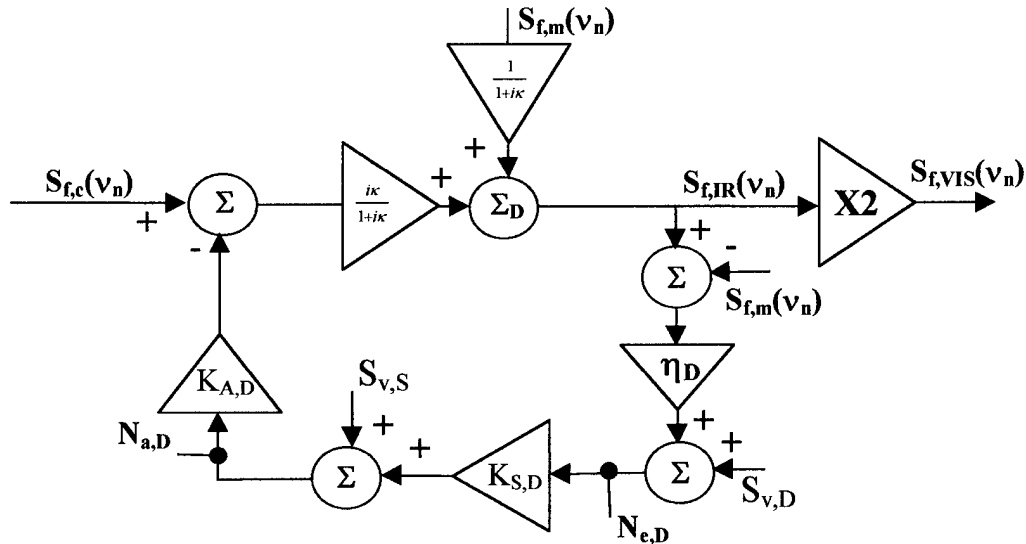


Figure 7.3. Frequency noise control loop (frequency-doubler).

The actuator and servo coefficients are represented as $K_{A,D}$ and $K_{S,D}$ and the error and actuator points are represented as $N_{e,D}$ and $N_{a,D}$.

By tracing the control loop clockwise as done in Chapters 3-5 for other noise control loops, it can be shown that the closed loop spectral density of frequency noise of the generated visible field is given by Equation 7.16.

$$S_{f,vis} = 2 \cdot \left\{ S_{f,m} \cdot \left| \frac{1 + i\kappa \cdot \frac{G_{OL,D}}{1 + G_{OL,D}}}{1 + i\kappa} \right| + \frac{\sqrt{(S_{f,c})^2 + (K_{A,D} \cdot K_{S,D} \cdot S_{V,D})^2 + (K_{A,D} \cdot S_{V,S})^2}}{|1 + G_{OL,D}|} \cdot \left| \frac{i\kappa}{1 + i\kappa} \right| \right\} \quad (7.16)$$

The open loop gain of the doubler control loop, $G_{OL,D}$, is defined in Equation 7.17.

$$G_{OL,D} = K_{A,D} \cdot K_{S,D} \cdot K_{D,D} \quad (7.17)$$

Note that Equation 7.16 is functionally identical to the injection-locking control theory result of Equation 5.30. Thus, the key difference between these two processes, in the frequency stabilization sense, is the corner frequency of their frequency noise transfer functions. In this analysis the corner frequency is $\delta\nu/2$ and in the injection-locking case it was ν_{Lock} . This suggests that the theory of Section 5.5, regarding the further frequency stabilization of the injection-locked field using various global control loops, is equally valid for the further stabilization of the frequency-doubled NPRO. Thus, the optimal frequency stabilization of the frequency-doubled NPRO is achieved by detecting the frequency noise of the visible field (Equation 7.16) and feeding the high frequency ($\nu_n > \delta\nu/2$) noise back to a phase modulator placed in the path of the visible output and the low frequency noise ($\nu_n < \delta\nu/2$) back to the laser.

7.2 Verifying Frequency Noise Transfer Functions

To verify the transfer functions of Equation 7.12, and the noise control loop diagram of Figure 7.2, I sent the frequency-doubled field to a PDH discriminator and locked the second harmonic of the NPRO to a longitudinal resonance of this reference cavity, as shown in Figure 7.4.

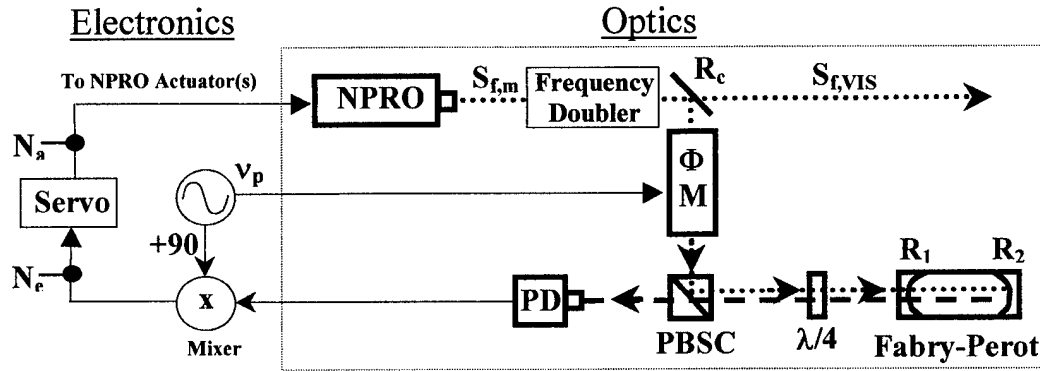


Figure 7.4. Locking the Frequency-Doubled NPRO to a Fabry-Perot.

The frequency noise control loop of this set-up is quite complicated and the resulting closed loop spectral density of frequency noise is also rather complex. If we consider the frequency regime outside the open loop bandwidth of both the doubler cavity and NPRO feedback loops ($\nu_n > \nu_{UG}$) then the signal at the error point of the Fabry-Perot control loop, shown in Figure 7.4, is the product of the Fabry-Perot discriminator constant, K_D , and the open loop visible frequency noise, $S_{f,VIS}$ of Equation 7.12.

$$N_e = K_D \cdot S_{f,VIS} = K_D \cdot \left(\left| \frac{i \cdot \kappa}{1 + i \cdot \kappa} \right| \cdot 2 \cdot S_{f,c} + \left| \frac{1}{1 + i \cdot \kappa} \right| \cdot 2 \cdot S_{f,m} \right) \quad (7.18)$$

To test the validity of this equation, I measured the discriminator coefficient, K_D , of the Fabry-Perot, using the technique outlined in Section 4.3, to be 0.35 V/MHz. I measured the NPRO actuator coefficient, K_A , by sweeping the output infrared NPRO frequency through the resonance of a 1 μm PDH Fabry-Perot discriminator to be ~ 5.25 MHz/V. To

measure the actuator, $K_{A,D}$, and discriminator, $K_{D,D}$, coefficients of the doubler cavity I applied a voltage ramp to the doubler cavity PZT. The actuator coefficient was determined to be the ratio of the voltage applied to the PZT (causing it to sweep through one FSR of the cavity) to the FSR of the cavity, ~ 291 MHz. The actuator coefficient, $K_{A,D}$, was found to be 107 MHz/V. To determine the discriminator coefficient and the bandwidth of the cavity, $\delta\nu_c$, I increased the resolution of the oscilloscope signal surrounding a particular resonance, as shown in Figure 7.5.

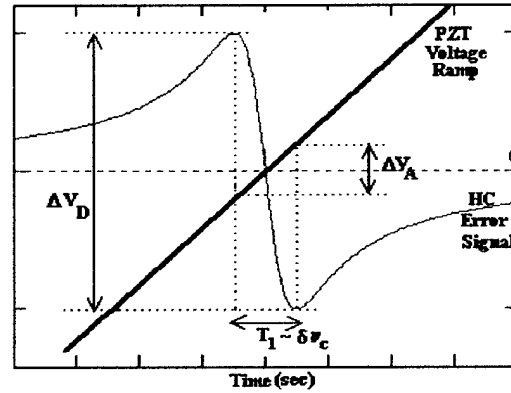


Figure 7.5. Hansch-Coulliard error signal determination of $K_{D,D}$ and $\delta\nu_c$.

The discriminator constant is equal to the ratio of the peak-to-peak voltage of the signal, ΔV_D , to the bandwidth of the cavity, $\delta\nu_c$. Where $\delta\nu_c$ can be shown in the Hansch-Coulliard technique to be equal to the bandwidth of the central dispersive regime of the error signal, measured in the frequency domain. If we assume a linear PZT response, in $\mu\text{m}/\text{sec}$, and thus a linear cavity frequency response, in Hz/sec , then the bandwidth of the cavity, $\delta\nu_c$, is equal to the product of ΔV_A of Figure 7.5 and the actuator coefficient, $K_{A,D}$. Equations 7.19 and 7.20 represent the explicit expressions for the determination of the double cavity bandwidth, $\delta\nu_c$, and the discriminator coefficients.

$$\delta\nu_c = K_{A,D} \cdot \Delta V_A \quad (7.19)$$

$$K_{D,D} = \frac{\Delta V_D}{\delta v_c} \quad (7.20)$$

The measured value of δv_c was 5.35 MHz and that of $K_{D,D}$ was 0.077 V/MHz.

Note that the measurement of δv_c also yields a measure of how well the doubler cavity is impedance matched. After all, we know the value of γ_e of Equation 7.1 (with $R_{oc} = 0.95$, and $L \sim 1.035$ m) divided by 2π to be nearly 2.3 MHz. If the cavity is perfectly impedance matched, γ_0 will equal γ_e and γ_c will equal $2 \times \gamma_e$. Thus, δv_c will equal 4.6 MHz. In this case, δv_c was measured to be 5.35 MHz and the output visible field power was 55 mW. On a separate occasion, with the other reference doubler cavity, δv_c was measured to be 4.46 MHz/V and the output visible power was 95 mW, revealing that the cavity was certainly more impedance matched than the case considered here.

With both the doubler cavity locked to the laser and the laser locked to the Fabry-Perot, I injected known voltage signals onto the laser and the doubler cavity using summing circuits at the exit of each of their servos. I applied 1 mV to the NPRO PZT (yielding an $S_{f,m}$ of 5.2 kHz) and 0.005 mV to the doubler cavity PZT (yielding an $S_{f,c}$ of nearly 5.2 kHz) at slightly offset noise frequencies ($\Delta v_n \sim 0.5$ Hz) simultaneous at v_n ranging from 20 to 60 kHz. I verified that the voltage signals at the error point of the doubler control loop were equal in amplitude for each noise signal, suggesting that $S_{f,m}$ was indeed equal to $S_{f,c}$. I then measured the voltage signals obtained at the N_e point of the Fabry-Perot control loop, and divided them by K_D to determine $S_{f,VIS}$. Figure 7.6 compares the theoretical $S_{f,VIS}$ from Equation 7.12, for the incident laser, $S_{f,m}$, and the doubler cavity, $S_{f,c}$, (both connected with solid lines) with the experimental value of $S_{f,VIS}$ obtained by dividing N_e by K_D .

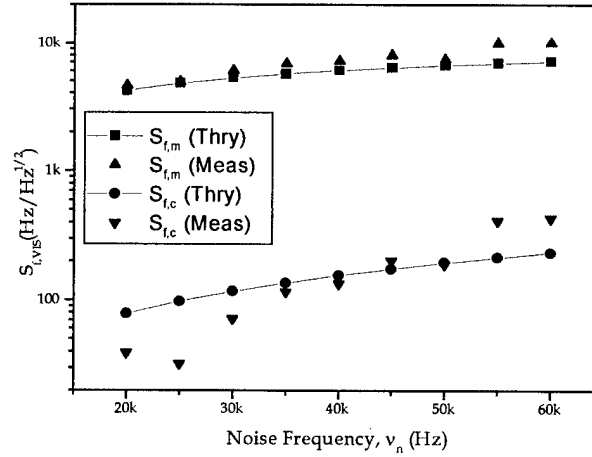


Figure 7.6. Results of experiment to verify visible field frequency noise transfer functions.

Figure 7.6 shows an excellent agreement between the theoretical noise of the frequency-doubled field (given a 5.2 kHz input frequency noise) and the measured noise. This suggests that the control loop of Figure 7.3 and the closed loop spectral density of frequency noise of Equation 7.16 do accurately model the frequency doubler.

7.3 Frequency-Doubler Stabilization Results

Figure 7.7 displays the typical result of the relative frequency stabilization of the doubler cavity resonant frequency to the frequency of the incident NPRO laser.

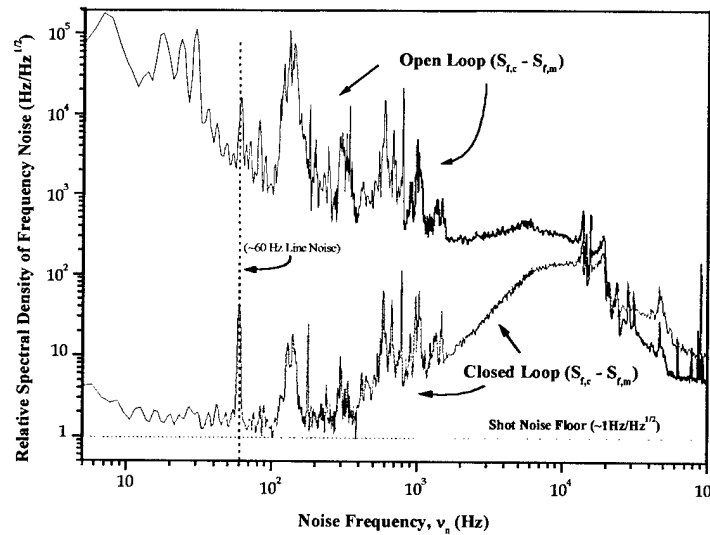


Figure 7.7. Relative frequency noise of doubler cavity with respect to incident NPRO.

According to Figure 7.7, the relative frequency noise of the doubler cavity is nearly shot-noise limited at a value of $\sim 1 \text{ Hz/Hz}^{1/2}$ at noise frequencies out to 400 Hz. The shot noise level was determined based on the DC voltage output of the photodetectors of Figure 7.1, while the laser was locked. The chief limitation to this frequency stabilization effort was the limited bandwidth of the PZT ($\sim 20 \text{ kHz}$) used to control the resonant frequency of the doubler cavity. The resulting open loop unity gain bandwidth was nearly 7 kHz.

Despite this limitation, the combined effect of the high pass transfer function of the doubler cavity and this noise suppression feedback loop significantly reduce the frequency noise contribution of the doubler cavity onto the output visible field, of Equation 7.16, at noise frequencies out to at least 100 kHz. After all, with $\delta\nu_0/2 \sim 2.5 \text{ MHz}$, 100 kHz is still a factor of 25 below the corner frequency of the doubler cavity high pass filter.

7.4 Summary

In this chapter, I determined and experimentally verified the transfer functions of the incident laser and the resonant doubler frequency noise onto the output frequency-doubled field. I showed that the frequency noise of the visible output field is functionally identical to that of the injection-locked output field of Chapter 5. Consequently, I concluded that the optimal stabilization of the frequency-doubled NPRO is established using Technique 3 of Chapter 5: detecting the frequency noise of the visible field and feeding the low frequency ($\nu_n < \delta\nu_0/2$) noise to the NPRO and the high frequency noise ($\nu_n > \delta\nu_0/2$) to an EOM placed in the path of the visible output field. Finally, I reported the common results of my efforts to reduce the frequency noise of the doubler cavity with respect to the incident NPRO laser.

CHAPTER 8. Absolute Frequency Stabilization

Assume that the pointing instability and amplitude noise of the injection-locked laser are eliminated, and the open loop bandwidth of the control loops is increased. Given this situation, the theory of Chapter 5 suggests that Technique 3 is the best global frequency noise suppression scheme. However, the limit of all three global frequency noise suppression techniques of Chapter 5 is the relative frequency stability of the reference. To improve the frequency stability of the high power, injection-locked output one must replace the relative frequency reference (the Fabry-Perot) with an absolute reference: an atomic or molecular transition.

8.1 Absolute Frequency References Near 1.064 μm

Much work has been done in the field of high-resolution saturation spectroscopy to search for atomic and molecular transitions with narrow absorption linewidths at the frequencies of interest for various laser applications. The results of such efforts have revealed the existence of at least five molecules that can serve as potential frequency discriminators near 1.064 μm : C_2HD ,⁵⁴ C_2H_2 ,⁵⁵ CO_2 ,⁵⁶ Cs_2 ,⁵⁷ and I_2 ($\sim 532 \text{ nm}$).^{33,34} A point of interest is that the spectroscopic techniques used to gain higher sensitivity in searching for these transitions can easily be employed to lock the laser to the transition. After all, the same phase information that generates a dispersive curve centered at the transition is used to lock the laser to this transition. Thus, any technique that improves the sensitivity of the spectroscopic signal will also improve the sensitivity of the discriminator to frequency fluctuations of the laser when this transition is later used as a reference.

The electronic transitions of Cs_2 near $1.064\text{ }\mu\text{m}$ and I_2 neighboring 532 nm (probed with a frequency-doubled $1.064\text{ }\mu\text{m}$ laser) have been investigated in great detail using standard Doppler-free, pump-probe, saturation spectroscopy techniques. Since the lifetime of the excited state of such electronic transitions is on the order of a microsecond, the natural linewidth is on the order of a megahertz. Since the linewidth of the transition is the chief determiner of the discriminator slope, K_D , (broader linewidths yielding smaller slopes), it is desirable to use the molecule with the narrowest absorption linewidth to achieve the minimal closed loop spectral density of frequency noise.

The other three molecules (C_2HD , C_2H_2 , CO_2) experience rotational-vibrational overtone transitions at $1\text{ }\mu\text{m}$. The lifetime of the excited states of such transitions is on the order of a millisecond, significantly decreasing their natural linewidth. However, since such transitions are inherently very weak, Doppler-free, cavity-enhanced, saturation spectroscopy techniques have been developed to investigate them which are much more sensitive than the simple pump-probe experiments. The chief limitation to observing the natural linewidths of these molecules is the transit-time broadening of the resonance, brought about by the finite interaction time of a given molecule traversing the cross section of the saturating field.⁵⁸ Since the velocity of the molecule is inversely proportional to the square root of the mass of the molecule, these relatively light molecules are especially sensitive to this limitation. To resolve the natural linewidth, one can expand the saturating beam cross-section or implement a slow molecule detection scheme. Slow molecule optical selection is achieved by reducing the power of the saturating field. In so doing, the slower molecules interact with the field for a longer amount of time than the faster molecules. Therefore the saturation signal is dominated by

the contributions of the slower molecules, significantly reducing the observed linewidth to a value less than the transit-time limit. The use of cavity-enhanced techniques, altered for slow molecule detection, has yielded linewidths of 20 kHz in C₂HD, a factor of thirteen below the transit-time limit of that particular experiment.⁵⁹

Of the three molecules, the narrowest theoretical linewidth is that of CO₂, which is expected to have a transition near 1.064 μm of width 170 Hz.⁶⁰ Preliminary experiments have yielded a saturated linewidth of nearly 410 kHz at a pressure of 5.6 mTorr and a 100 W circulating field.⁵⁶ Also, an adjacent non-saturated absorption peak was observed with a linewidth of nearly 100 kHz. A complete cavity-enhanced saturation spectroscopic investigation, employing slow molecule detection schemes (preferably at pressures much less than a mTorr), of several of the rotational-vibrational lines of CO₂ neighboring 1.064 μm is necessary before discounting this molecule as the best possible frequency discriminator in this frequency regime.

To perform the spectroscopy of CO₂ and to characterize the frequency stability of a laser (or even an injection-locked laser) locked to CO₂ one needs an in-lab frequency reference at 1.064 μm . To characterize the in-lab reference, using standard beatnote measurements, a second, identical in-lab reference is needed. Mr. Joshua Bienfang and I established two identical in-lab frequency references at 1.064 μm by stabilizing two frequency-doubled NPROs to the well-documented hyperfine components of the electronic transitions of I₂, using a modulation-transfer spectroscopy technique.

8.2 Overview

In this chapter, I review my attempts to model the closed loop spectral density of frequency noise of this in-lab reference for the sake of determining the optimal noise

detection and suppression scheme. I expand the control loop of the frequency-doubler, presented in Chapter 7, to include the absolute frequency stabilization control loop established when locking the laser to an electronic transition in Iodine. Finally, I characterize the reference through Root Allan Variance (RAV) measurements of the beatnote of the two in-lab references, and the spectral density of frequency noise measured at the error point of the absolute frequency stabilization control loop.

8.3 Characterizing the 1 μm In-Lab Reference

Using the frequency-doubled NPRO, I probed several well-documented hyperfine components of electronic transitions of I_2 neighboring 532 nm, with the experiment shown in Figure 8.1.

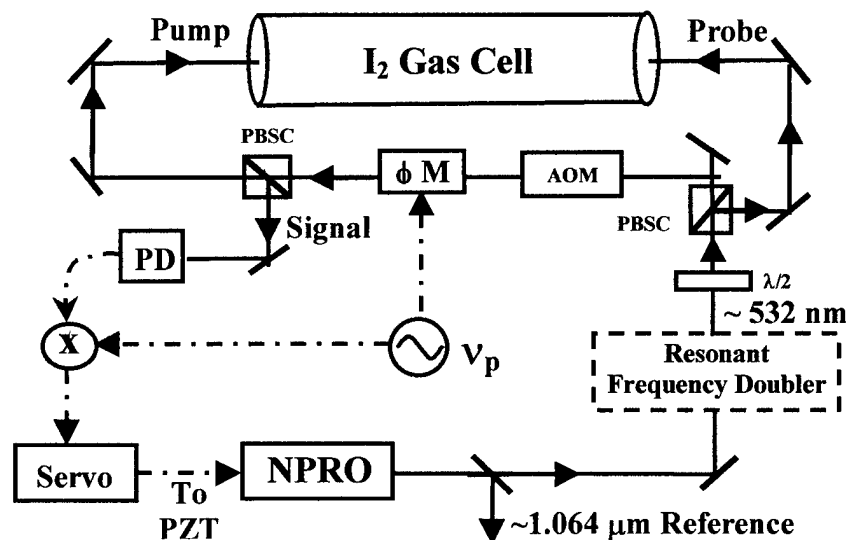


Figure 8.1. In-Lab Iodine reference.

This is a standard FM modulation-transfer spectroscopy experiment and is described in some detail in the literature.^{33,61,62} The frequency-doubled NPRO is split into cross-polarized pump and probe fields. The pump field is frequency shifted by 80 MHz with the AOM and then phase modulated with the EOM at frequency 550 kHz. The

modulation sidebands of the pump field interact with the pump carrier field and the probe field in the nonlinear medium (I_2), in a four-wave mixing process, to generate modulation sidebands on the probe. The probe field and its sidebands are then passed to the photodetector, to obtain the signal. The amplitude of the signal is proportional to the product of the pump field carrier and modulation sideband amplitudes (as was the case for every FM modulation technique of this thesis including the PDH technique).

The actuator coefficient of the NPRO was determined to be 2.3 MHz/V, and the actuator coefficient of the visible field was verified with a Fabry-Perot PDH discriminator to be nearly 4.6 MHz/V. The discriminator coefficient was determined by sweeping the laser through a resonance, as shown in Figure 8.2.

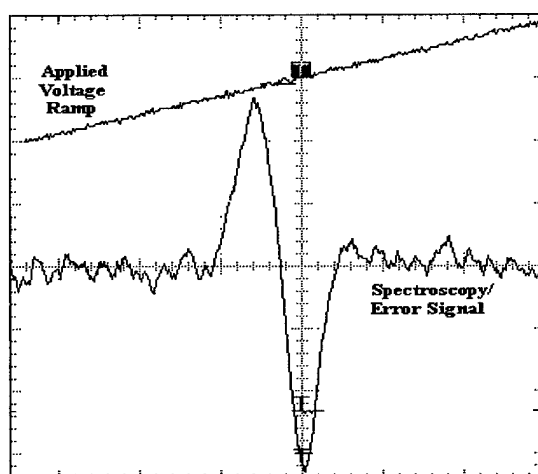


Figure 8.2. Sample Iodine dispersion curve.

Knowledge of the visible actuator coefficient, 4.6 MHz/V, enabled me to determine the width of the dispersion curve (~ 1.5 MHz for this particular resonance). The ratio of the peak-to-peak voltage of the dispersion curve to its frequency width yielded the value of K_D : 0.98 V/MHz.

I locked the frequency-doubled NPRO to this transition and measured the spectral density of voltage noise at the entrance (N_e point) and exit (N_a point) of the servo. To determine the exact relationship between these signals and the open and closed loop spectral density of frequency noise of the $1.064\text{ }\mu\text{m}$ reference field of Figure 8.1, I established the effective control loop of Figure 8.3.

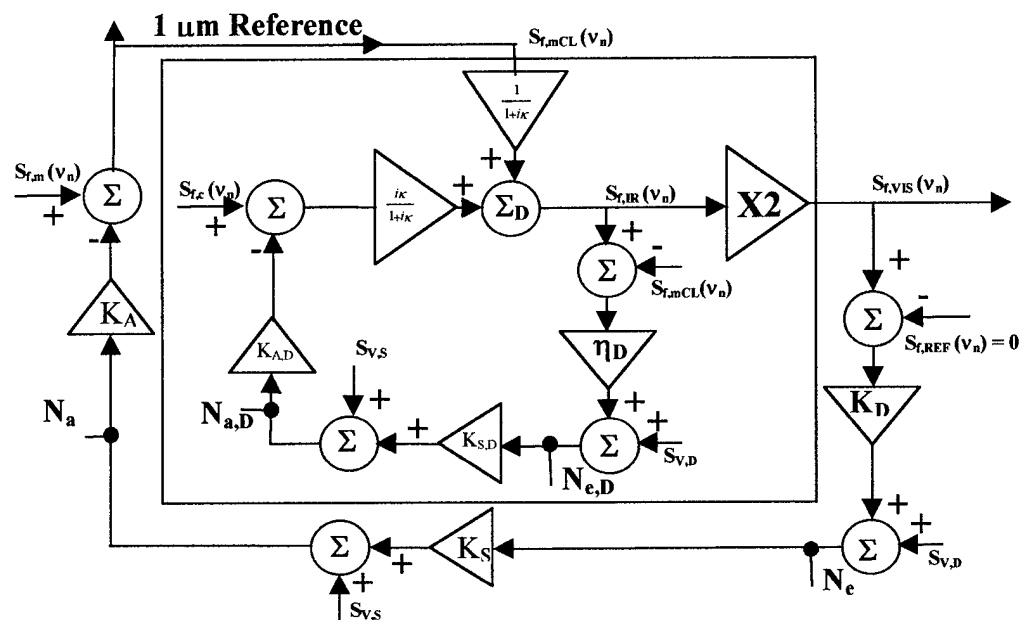


Figure 8.3. Frequency noise control loop (in-lab Iodine reference).

The open loop frequency noise of the NPRO, $S_{f,m}$, is shown at the far left as the input to this control loop. The closed loop frequency noise output of the NPRO, $S_{f,mCL}$, is shown to equal that of the 1 μm reference, given the exact placement of the mirror directing the reference field away from the NPRO in Figure 8.1. The frequency-doubler control loop of Figure 7.3 is shown within the solid box and the absolute stabilization loop is shown to encompass this loop.

The results of the control loop analysis are very similar to those of the injection-locking control loops of Chapter 5. Below, I neglect the frequency noise contributions of

the doubler cavity, since the doubler noise contributions are not only reduced by the doubler control loop but also by the high pass filter transfer function with corner frequency of ~ 2.5 MHz. Analysis of this control loop yields the closed loop spectral density of frequency noise of the $1 \mu\text{m}$ reference field, $S_{f,mCL}$, shown in Equation 8.1, in terms of the closed loop frequency noise transfer function of the NPRO onto the visible field, $T_{M,CL}$, shown in Equation 8.2.

$$S_{f,mCL}(\nu_n) = \left\{ \frac{\sqrt{(S_{f,m}(\nu_n))^2 + (K_A(\nu_n) \cdot K_S(\nu_n) \cdot S_{V,D})^2 + (K_A(\nu_n) \cdot S_{V,S})^2}}{|1 + 2 \cdot T_{M,CL}(\nu_n) \cdot G_{OL}(\nu_n)|} \right\} \quad (8.1)$$

$$T_{M,CL}(\nu_n) = \left\{ \frac{1 + i \cdot \kappa \cdot \frac{G_{OL,D}(\nu_n)}{1 + G_{OL,D}(\nu_n)}}{1 + i \cdot \kappa} \right\} \quad (8.2)$$

Note that the frequency noise of the NPRO laser is reduced by the open loop transfer function of the absolute frequency stabilization control loop, G_{OL} , multiplied by the closed loop transfer function of the NPRO frequency noise onto the visible field, $T_{M,CL}$. This transfer function is equal to one in the frequency regime where the doubler control loop open loop gain, $G_{OL,D}$ of Equation 8.3, is much greater than one.

$$G_{OL,D}(\nu_n) = K_{A,D}(\nu_n) \cdot K_{S,D}(\nu_n) \cdot K_{D,D}(\nu_n) \quad (8.3)$$

Since the unity gain bandwidth of the doubler control loop was limited to nearly 10 kHz, $T_{M,CL}$ becomes a low pass filter of corner frequency, $\delta\nu_c/2 \sim 2.5$ MHz, at frequencies above ~ 10 kHz. Thus, as in Technique 2 of Section 5.5, the global frequency noise control loop (the absolute stabilization loop in the present discussion), is reduced in efficiency at high noise frequencies ($\nu_n > \delta\nu_c/2$).

Given the relatively high value of $\delta\nu/2$ (~ 2.5 MHz) for my experiment, this reduction was negligible since the unity gain bandwidth of the absolute frequency stabilization control loop was nearly 20 kHz (limited by the resonance-free bandwidth of the PZT of the NPRO). Nevertheless, I point out the possible limitation of this experiment in case the experimental parameters are altered (the bandwidth of G_{OL} increases significantly or $\delta\nu_c$ is reduced) in the future.

Tracing the signal clockwise through the elaborate control loop of Figure 8.3 reveals the following relationship between the error (N_e) and actuator (N_a) point voltage measurements and the open and closed loop spectral density of frequency noise of the NPRO.

$$N_e(\nu_n) \approx \begin{cases} K_D (2 \cdot S_{f,mCL}(\nu_n)) & \nu_n < \nu_{UG} \\ K_D \left(2 \cdot S_{f,mCL}(\nu_n) \cdot \left| \frac{1}{1 + iK} \right| \right) & \nu_n > \nu_{UG} \end{cases} \quad (8.4)$$

$$S_{f,m}(\nu_n) \approx \begin{cases} K_A \cdot N_a(\nu_n) & \nu_n < \nu_{UG} \\ \frac{N_e}{2 \cdot K_D \cdot \left| \frac{1}{1 + iK} \right|} & \nu_n > \nu_{UG} \end{cases} \quad (8.5)$$

Well within the unity gain bandwidth of the absolute frequency stabilization control loop, all of the frequency-doubled NPRO noise is incident on the discriminator and the standard error point and actuator point relations prevail. However, outside the loop bandwidth the frequency noise of the NPRO is low pass filtered (with corner frequency equal to $\delta\nu/2$ of the doubler cavity ~ 2.5 MHz) before it arrives to the discriminator. This low pass filter transfer function must be accounted for when determining the original $1 \mu\text{m}$ frequency noise originating from the laser.

8.4 Absolute Frequency Stabilization Results

I locked my laser to a particular hyperfine component of an electronic transition of I_2 . With the laser locked, I recorded the spectral density of voltage noise at N_e and N_a of the absolute stabilization control loop and used Equations 8.4 and 8.5 to determine the open and closed loop spectral density of frequency noise of the $1\text{ }\mu\text{m}$ reference, $S_{f,m}$ and $S_{f,mCL}$, respectively. Figure 8.4 displays the result of this measurement.

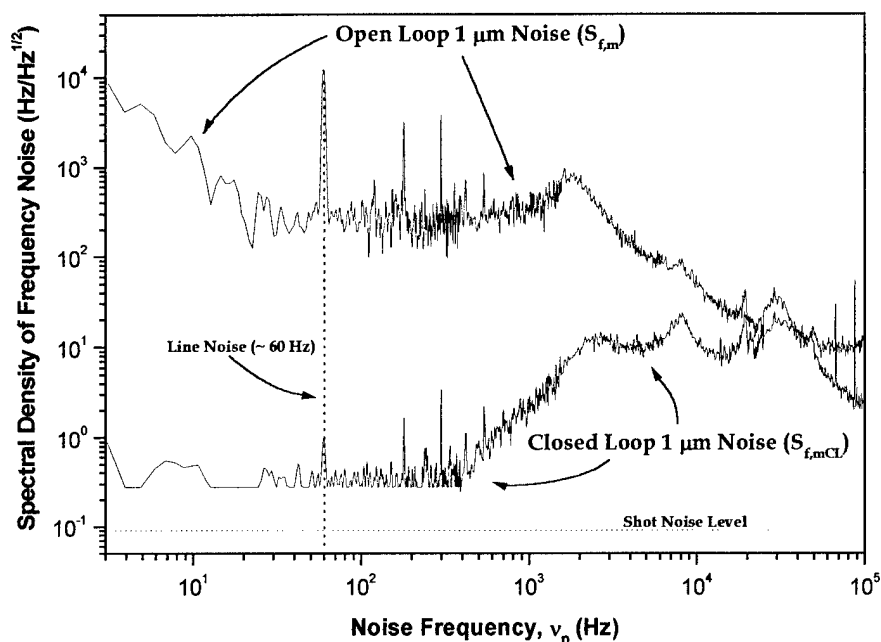


Figure 8.4. Spectral density of frequency noise of the $1\text{ }\mu\text{m}$ reference.

The closed loop spectral density of frequency noise of the NPRO, $S_{f,mCL}$, was reduced to $0.3\text{ Hz/Hz}^{1/2}$ at noise frequencies below 400 Hz, slightly above the shot noise level of $0.09\text{ Hz/Hz}^{1/2}$, determined from the DC voltage output of the photodiode while the laser was locked. This is a factor of 10 worse than the average closed loop relative frequency noise of the NPRO laser locked to a Fabry-Perot which was generally $0.03\text{ Hz/Hz}^{1/2}$ over the course of the various experiments performed in this effort. This is partially due to the factor of five difference between the discriminator slope achieved

with these two locking techniques (0.98 V/MHz in this experiment compared to 5 V/MHz for the Fabry-Perot locking scheme).

To further characterize the 1 μm reference, Mr. Bienfang and I directed a portion of our 1 μm reference beams (from the two identical references) to a photodetector to measure the Root Allan Variance (RAV) of the beatnote signal. Figure 8.5 displays the resulting RAV data (represented with a series of squares connected with a line).

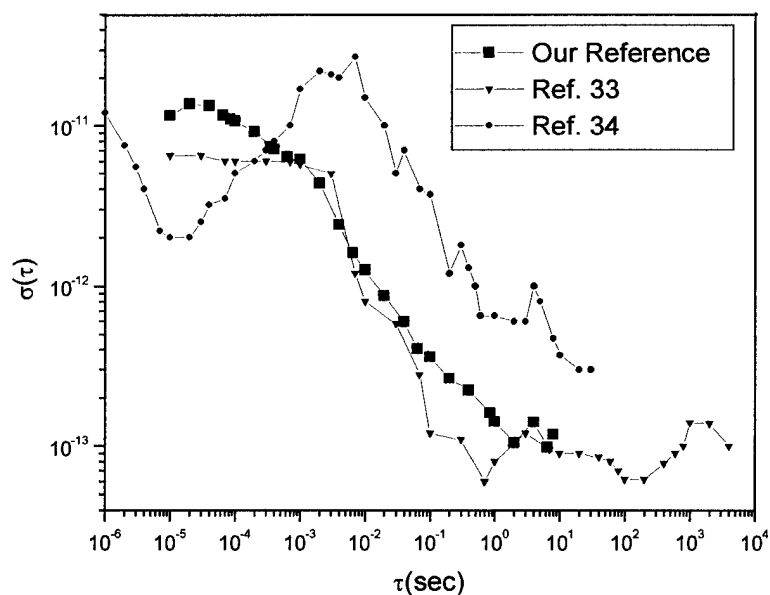


Figure 8.5. Root Allan Variance of the beatnote of our two identical 1 μm references.

For comparison's sake, I also present the previous data obtained from similar I_2 references reported in the literature.^{33,34} Note that our results are very similar to the results of Ref. 33, as expected since we employed the identical modulation transfer scheme employed by this group. The reference displays a minimal RAV of 1×10^{-13} for a time interval of 1 second, about a factor of 3 higher than the lowest RAV reported by Ref. 33 of 3×10^{-14} at a time interval of 0.8 seconds.

8.5 Summary

In this chapter, I modeled the absolute frequency stabilization experiment used to establish an in-lab $1\mu\text{m}$ reference using the control theory principles presented throughout this thesis. I showed that the closed loop spectral density of frequency noise of the reference was nearly identical in form to the closed loop frequency noise contribution of the master laser to the injection-locked output in Technique 2 of Chapter 5. As in Chapter 5 (Technique 3), the optimal stabilization of this laser would detect the frequency noise of the visible field and send the low frequency noise ($\nu_n < \delta\nu_c/2$) to the laser and the high frequency noise ($\nu_n > \delta\nu_c/2$) to a phase modulator placed in the path of the visible field. However, the rather large value of $\delta\nu_c/2$, ~ 2.5 MHz, eliminates the need for this elaborate technique since the residual frequency noise of the laser at these high frequencies is negligible anyway.

Finally, I characterized the frequency stability of the $1\mu\text{m}$ reference. I reported that the closed loop spectral density of frequency noise was reduced to $0.3\text{ Hz/Hz}^{1/2}$ for noise frequencies below 400 Hz and the minimal Root Allan Variance achieved was 10^{-13} for a time interval of 1 second (comparable to the previously reported results of similar references).

CHAPTER 9. Summary and Future Work

In this chapter, I review the key contributions of this thesis and discuss the research necessary to further improve the power and frequency stability of the injection-locked laser.

9.1 Primary Contributions

By using the thermo-optical model of Mordough, I was able to optimize the slave resonators containing three different arc-lamp pumped Nd:YAG rods to achieve greater than 25 W of linearly polarized, TEM₀₀, injection-locked output.

To insure the slave laser remained injection-locked to the master laser, I employed the PDH stabilization technique which is most-often used to stabilize the output frequency of lasers to a resonant frequency of a Fabry-Perot. Based on the results of various measurements made on the injection-locked system, I derived an explicit form of the PDH injection-locking error signal based on the damped, driven wave equation description of the circulating field of the slave laser resonator. I found that even though the transfer function of the master laser frequency noise onto the injection-locked output is a low pass filter of corner frequency, ν_{Lock} , and that of the slave laser is a high pass filter of similar corner frequency, the PDH error signal is equally susceptible to the frequency noise of each. I used this error signal and the results of various measurements to establish a control loop diagram (Figure 5.4) that completely modeled the frequency stability of the injection-locked output field. I then expanded this control loop to compare the theoretical results of employing three different global stabilization schemes. Clearly Technique 3, which detects the frequency noise of the injection-locked output and sends the low frequency noise ($\nu_n < \nu_{\text{Lock}}$) to the master and the high frequency noise

($\nu_n > \nu_{\text{Lock}}$) to an EOM in the output path of the injection-locked laser, was the optimal technique. However, I showed that given the limited bandwidths of the control loops of this thesis (~ 20 kHz), which are much less than ν_{Lock} (~ 750 kHz), the other two schemes (Techniques 1 and 2) yield comparable results. Technique 1 involves prestabilizing the master laser and Technique 2 involves detecting the frequency noise of the injection-locked output and feeding it back to the master laser. I tested this theory and actually found that Technique 1 yielded the best results, primarily due to the susceptibility of Technique 2 to the pointing instability of the slave laser. I reported achieving a 24-W, $M^2 \sim 1.07$, linearly-polarized output with a linewidth of 1.6 Hz by injection-locking an arc-lamp pumped Nd:YAG rod laser to an NPRO laser and further stabilizing the output with Technique 1.⁶³

I revisited the problem of locking a laser to a Fabry-Perot, using the damped, driven wave equation analysis to describe the circulating field of this resonator. This analysis yielded three important contributions to the previous results from the literature. First, this analysis revealed terms describing the coupling between the frequency noise of the incident laser and the amplitude noise of the circulating field. I later showed that this coupling could be eliminated by adjusting the DC offset of the servo element of the feedback loop. Second, this analysis revealed the relations between the frequency noise of the incident laser and the resonant frequency of the Fabry-Perot cavity onto the frequency noise of the circulating field with the corner frequency equal to the halfwidth of the cavity reflection coefficient, $\delta\nu/2$. Comparison of these transfer functions and those of the injection-locking experiment verified that their forms are identical and that the corner frequency of the transfer functions of each are related to the photon lifetime of

the circulating field of each resonator. Third, this analysis revealed the explicit contribution of the frequency noise associated with the Fabry-Perot onto the PDH error signal.

I then used the frequency noise transfer functions of the Fabry-Perot to determine the relationship between the frequency noise of the electric field output of an external cavity frequency-doubled laser and the noise of the incident laser and the frequency noise associated with the length fluctuations of the external cavity. I established an effective control loop to describe the frequency-doubled laser and used this loop to show the similarity between the frequency-doubled laser and the injection-locked laser. I concluded that the optimal stabilization scheme for the injection-locked laser, Technique 3, is the same as the optimal scheme for reducing the frequency noise of the external cavity frequency-doubled laser. Thus, the optimal scheme detects the frequency noise of the doubled field and feeds the low frequency noise ($\nu_n < \delta\nu_c/2$) back to the laser and the high frequency noise ($\nu_n > \delta\nu_c/2$) directly back to an EOM or AOM placed in the path of the doubled field.

Finally, I established an in-lab 1.064 μm frequency reference by stabilizing the frequency-doubled NPRO to a hyperfine component of an electronic transition in I_2 . I did not employ Technique 3 since I was not interested in reducing the frequency noise of the doubled field beyond $\delta\nu_c/2 \sim 2.5$ MHz. Instead, I employed Technique 2, detecting the frequency noise of the doubled field (using the modulation transfer discriminator method) and feeding it back to the laser. I reported achieving a minimum Root Allan Variance of 10^{-13} at a time interval of 1 second and showed that the stability of the in-lab reference was comparable to the results of similar references reported in the literature.^{33,34}

9.2 Future Work

To improve the output power and pump efficiency and reduce the frequency and amplitude noise of the slave laser, one must transition from arc-lamp pumping to transverse diode-pumping. By using the thermo-optical model of Mardouh in conjunction with the birefringent compensation techniques recently reported,⁴¹ one should be able to scale the linearly-polarized TEM₀₀ output power much greater than the highest currently recorded power of 62 W.⁸

One can then injection-lock this laser with an NPRO laser and insure the laser remains locked by employing a PDH locking scheme. The chief limitation to the PDH injection-locking experiments of this thesis was the bandwidth of the slave cavity PZTs (~20 kHz). By replacing these PZTs with higher bandwidth PZTs, one can further reduce the relative frequency noise of the slave with respect to the master laser.

To further improve the frequency stability of the injection-locked output beyond that achieved here, one should establish Technique 3 but replace the Fabry-Perot reference with an absolute frequency reference such as an atomic or molecular transition. Since the slope of the frequency discriminator determines the minimal achievable spectral density of frequency noise, the narrowest atomic or molecular transition is desired. The best candidates at 1.064 μm are C₂HD and CO₂. Using slow molecule detection schemes the narrowest linewidth achieved with C₂HD has been ~ 20 kHz.⁵⁹ On the other hand, a preliminary investigation of CO₂ has yielded linewidths much greater than the theoretical natural linewidth of 170 Hz.⁵⁶ This investigation also revealed the possible presence of a two-photon transition neighboring the single line investigated. An in-depth spectroscopic investigation of CO₂ is needed to accomplish two tasks before

discounting this molecule as a possible frequency reference near 1.064 μm . First, slow molecule selection techniques should be used to attempt to resolve the single-photon transition with respect to the two-photon transition. Second, an investigation of the other overtone transitions immediately neighboring this transition should be attempted to determine their linewidths. These transitions are ~ 40 GHz away from the line analyzed in Ref. 56.^{64,65} Although the specification of the tuning range of the NPRO is 40 GHz and the first line is near the center of this tuning range, it may still be possible to probe a neighboring transition with the NPRO. To do this, one might try tuning the temperature of the NPRO to the limit of its range and then applying a DC voltage to the slow frequency control to force the laser to oscillate at a frequency outside of its specified operating regime. Although this will reduce the efficiency of the laser and thus its output power, only 10's of mW are needed (depending on the Finesse of the cavity) for the cavity-enhanced spectroscopy technique.

9.3 Conclusion

Thus, the optimal, high power, frequency-stable laser at 1.064 μm would be achieved by injection-locking a transverse diode-pumped Nd:YAG rod laser with an NPRO laser and further stabilizing the injection-locked output to an overtone transition in CO_2 , pending the results of future spectroscopic investigations of this molecule.

REFERENCES

1. P. Bender, "Distance measurements in space: Gravitational physics and a proposed laser gravitational wave antenna," Proc. Eleventh Int. Conf. on Atomic Physics, 567-588 (1988).
2. F. Bondu, P. Fritschel, C. N. Man, and A. Brillet, "Ultrahigh-spectral-purity laser for the VIRGO experiment," Opt. Lett. **21**, 582-584 (1996).
3. R. Boucher, B. Villeneuve, and M. Tetu, "Calibrated Fabry-Perot etalons as absolute frequency reference for OFDM communications," IEEE Photon. Tech. Lett. **4**, 801-804 (1992).
4. L. Ma and J.L. Hall, "Optical Heterodyne Spectroscopy Enhanced by an External Optical Cavity: Toward Improved Working Standards," IEEE J. Quantum Electr. **26**, 2006-2012 (1990).
5. K. Nakagawa, Y. Shimizu, T. Katsuda, M. Ohtsu, "Highly Stable and High Power Nd:YAG Lasers," SPIE 1837, 40-48 (1992).
6. K. Nakagawa, A.S. Shelkovnikov, T. Katsuda, and M. Ohtsu, "Absolute frequency stability of a diode-laser-pumped Nd:YAG laser stabilized to a high-finesse optical cavity," Appl. Opt. **33**, 6383-6386 (1994).
7. D. Golla, S. Knoke, W. Schone, G. Ernst, M. Bode, A. Tunnermann, and H. Welling, "300-W cw diode-laser side-pumped Nd:YAG rod laser," Opt. Lett. **20**, 1148-1150 (1995).
8. D. Golla, M. Bode, S. Knoke, W. Schone, and A. Tunnermann, "62-W cw TEM₀₀ Nd:YAG laser side-pumped by fiber-coupled diode lasers," Opt. Lett. **21**, 210-212 (1996).
9. D.R. Walker, C.J. Flood, H.M. van Driel, U.J. Greiner, and H.H. Klingenberg, "Efficient continuous-wave TEM₀₀ operation of a transversely diode-pumped Nd:YAG laser," Opt. Lett. **19**, 1055-1057 (1994).
10. M. Zhu and J.L. Hall, "Stabilization of optical phase/frequency of a laser system: application to a commercial dye laser with an external stabilizer," J. Opt. Soc. Am. B. **10**, 802-816 (1993).
11. T.J. Kane and R.L. Byer, "Monolithic, unidirectional single-mode Nd:YAG ring laser," Opt. Lett. **10**, 65-67 (1985).
12. *Diode-Pumped Solid-State Non-Planar Ring Laser Users Manual*, Lightwave Electronics Corporation, pg. 8, (1992).

13. N. Uehara and K. Ueda, "Ultrahigh-frequency stabilization of a diode-pumped Nd:Yag laser with a high-power-acceptance photodetector," *Opt. Lett.* **19**, 728-730 (1994).
14. I. Freitag, D. Golla, A. Tunnermann, H. Welling, and K. Danzmann, "Diode-pumped solid-state lasers as light sources of Michelson-type gravitational-wave detectors," *Appl. Phys. B* **60**, S255-S260 (1995).
15. S.T. Yang, Y. Imai, M. Oka, N. Eguchi, and S. Kubota, "Frequency-stabilized, 10-W continuous-wave, laser-diode end-pumped, injection-locked Nd:YAG laser," *Opt. Lett.* **21**, 1676-1678 (1996).
16. M. Musha, K Nakagawa, K Ueda, "Wideband and high frequency stabilization of an injection-locked Nd:YAG laser to a high-finesse Fabry-Perot cavity," *Opt. Lett.* **22**, 1177-1179 (1997).
17. S.T. Yang, C.C. Pohalski, E.K. Gustafson, R.L. Byer, R.S. Feigelson, R.J. Raymakers, and R.K. Route, "6.5-W, 532-nm radiation by cw resonant external-cavity second-harmonic generation of an 18-W Nd:YAG laser in LiB_3O_5 ," *Opt. Lett.* **16**, 1493-1495 (1991).
18. Y. Hirano, Y. Koyata, S. Yamamoto, K. Kasahara, and T. Tajime, "208-W TEM₀₀ operation of a diode-pumped Nd:YAG rod laser," *Opt. Lett.* **24**, 679-681 (1999).
19. W. Koechner, *Solid State Laser Engineering*, 3rd ed. (Springer-Verlag, Berlin, 1992), Chap 7.
20. M.P. Murdough and C.A. Denman, "Mode-volume and pump-power limitations in injection-locked TEM₀₀ Nd:YAG-rod lasers," *Appl. Opt.* **35**, 5925-5936 (1996).
21. A.E. Siegman, *Lasers* (University Science Books, Mill Valley, Calif., 1986), Chaps. 11, 24, and 29.
22. A.D. Farinas, E.K. Gustafson, R.L. Byer, "Frequency and intensity noise in an injection-locked, solid-state laser," *J. Opt. Soc. Am. B.* **12**, 328-334 (1995).
23. R. Barillet, "Injection-locking technique for the detection of gravitational waves," *Ann. Telecommun.* **51**, 553-566 (1996).
24. R. Barillet, A. Brillet, R. Chiche, F. Cleva, L. Latrach, C.N. Man, "An injection-locked Nd:YAG laser for the interferometric detection of gravitational waves," *Meas. Sci. Techn.* **7**, 162-169 (1996).

25. R.W.P. Drever, J.L. Hall, F.V. Kowalski, J. Hough, G.M. Ford, A.J. Munley, and H. Ward, "Laser Phase and Frequency Stabilization Using an Optical Resonator," *Appl. Phys B* **31**, 97-105 (1983).
26. T. Day, E.K. Gustafson, and R.L. Byer, "Sub-Hertz Relative Frequency Stabilization of Two-Diode Laser-Pumped Nd:YAG Lasers Locked to a Fabry-Perot Interferometer," *IEEE J. Quantum Elect.* **28**, 1106-1117 (1992).
27. N. Uehara and K. Ueda, "Frequency Stabilization of Two Diode-Pumped Nd:YAG Lasers Locked to Two Fabry-Perot Cavities," *Jpn. Journ. Appl. Phys.* **33**, 1628-1633 (1994).
28. Ch. Salomon, D. Hils, and J.L. Hall, "Laser stabilization at the millihertz level," *J. Opt. Soc. Am. B.* **8**, 1576-1587 (1988).
29. S. P. Sandford and C. W. Antill, Jr., "Laser Frequency Control using an Optical Resonator Locked to an Electronic Oscillator," *IEEE J. Quantum Elect.* **33**, 1991-1996 (1997).
30. T. Day, "Frequency Stabilized Solid-State Lasers for Coherent Optical Communications," PhD Dissertation, Stanford University, CA, 1990.
31. Y. Cheng, P.L. Mussche, A.E. Siegman, "Measurement of Laser Quantum Frequency Fluctuations Using a Pound-Drever Stabilization System," *IEEE J. Quantum Elect.* **30**, 1498-1504 (1994).
32. Mr. Joshua C. Bienfang and I worked together to produce the two in-lab frequency references using the modulation transfer spectroscopy technique.
33. M.L. Eickhoff and J.L. Hall, "Optical Frequency Standard at 532 nm," *IEEE Trans. on Instr. and Meas.* **44**, 155-158 (1995).
34. A. Arie, R.L. Byer, "Laser heterodyne spectroscopy of $^{127}\text{I}_2$ hyperfine structure near 532 nm," *J. Opt. Soc. Am. B* **10**, 1990-1997 (1993).
35. A.E. Siegman, *Lasers* (University Science Books, Mill Valley, Calif., 1986), Chap. 15
36. Yariv, *Quantum Electronics*, 3rd ed. (Wiley, New York, 1989), Chaps. 6 and 7.
37. G. Cerullo, "Output limitation in CW single transverse mode Nd:YAG lasers with a rod of large cross section," *Opt. and Quant. Electr.* **25**, 489-500 (1993).
38. W. Koechner, "Thermal Lensing in a Nd:YAG Laser Rod," *Appl. Opt.* **9**, 2548-2553 (1970).

39. M.P. Murdough, "Power scaling of CW injection-locked Nd:YAG lasers," M.S. Thesis (University of New Mexico, Albuquerque, NM, 1995).
40. W. Koechner, *Solid State Laser Engineering*, 3rd ed. (Springer-Verlag, Berlin, 1992), Chap. 3.
41. J. Sherman, "Thermal compensation of a cw-pumped Nd:YAG laser," *Appl. Opt.* **37**, 7789-96 (1998).
42. *Model SR760 FFT Spectrum Analyzer User's Manual*, Stanford Research Systems, Inc., pg. 3-1, (1994).
43. A.L. Lance, W.D. Seal, and F. Labaar, *Infrared and Millimeter Waves*, Vol. 11 (Academic Press, New York, 1984), Chap. 7.
44. S.R. Stein, *Precision Frequency Control*, Vol. 2 (Academic Press, New York, 1985), Chap 12.
45. T.W. Hansch and B. Couillaud, "Laser Frequency Stabilization by Polarization Spectroscopy of a Reflecting Reference Cavity," *Opt. Comm.* **35**, 441-444(1980).
46. S.G. Burns and P.R. Bond, *Principles of Electronic Circuits*, (West Publishing Co., New York, 1987), Chaps. 12 and 15.
47. I used the same method to solve these equations as done by Barillet in Ref. 23 to solve the similar expressions for the injection-locked laser.
48. J.T. Verdeyen, *Laser Electronics*, (Prentice-Hall, Inc., New Jersey, 1995), Chp. 6.
49. Mr. Joshua Bienfang performed most of the stabilization of NPRO lasers to commercial Fabry-Perot resonators to support the injection-locking experiments of this thesis.
50. L. Ziyuan, R.G.T. Bennett, G.E. Stedman, "Swept-frequency induced optical cavity ringing," *Opt. Comm.* **86**, 51-57 (1991).
51. C.D. Nabors, A.D. Farinas, T.Day, S.T. Yang, E.K. Gustafson, and R.L. Byer, "Injection locking of a 13-W cw Nd:YAG ring laser," *Opt. Lett.* **14**, 1189-1191 (1989).
52. Hewlett Packard Application Note 358-12: *Simplify Frequency Stability Measurements with Built-in Allan Variance Analysis*.
53. R.W. Boyd, *Nonlinear Optics*, (Academic Press Inc., San Diego, Calif., 1992), Chap. 2.

54. J. Ye, L. Ma, and J.L. Hall, "Ultrastable Optical Frequency Reference at 1.064 μm Using a C_2HD Molecular Overtone Transition," IEEE Trans. on Instr. and Meas. **46**, 178-181 (1997).
55. K. Nakagawa, T. Katsuda, A.S. Shelkovnikov, M. de Labachellerie, and M. Ohtsu, "Highly sensitive detection of molecular absorption using a high finesse cavity," Opt. Comm. **107**, 369-372 (1994).
56. J. Ye, "Ultrasensitive High Resolution Laser Spectroscopy and its Application to Optical Frequency Standards," PhD Dissertation, University of Colorado, (1998).
57. E. Inbar, V. Mahal, A. Arie, "Frequency stabilization of Nd:YAG lasers to $^{133}\text{Cs}_2$ sub-Doppler lines near 1064 nm," J. Opt. Soc. Am. B **13**, 1598-1604 (1996).
58. S.N. Bagayev, A.E. Baklanov, V.P. Chebotayev, and A.S. Dychkov, "Superhigh Resolution Spectroscopy in Methane with Cold Molecules," Appl. Phys. B **48**, 31-35 (1989).
59. J. Ye, L. Ma, and J.L. Hall, "Ultrasensitive detections in atomic and molecular physics: demonstration in molecular overtone spectroscopy," J. Opt. Soc. Am. B **15**, 6-14(1998).
60. P. Fritschel and R. Weiss, "Frequency match of the Nd:YAG laser at 1.064 μm with a line in CO_2 ," Appl. Opt. **31** 1910-1912 (1992).
61. J.H. Shirley, "Modulation transfer processes in optical heterodyne saturation spectroscopy," Opt. Lett. **7**, 537-539 (1982).
62. M.D. Levenson and S.S. Kano, *Introduction to Nonlinear Laser Spectroscopy*, (Academic Press, San Diego, Calif., 1988) Chap. 3.
63. R.F. Teehan, J.C. Bienfang, C.A. Denman, "Power scaling and frequency stabilization of an Injection-Locked Nd:YAG rod laser," submitted and accepted for publication in Appl Opt. (Spring 2000).
64. 1992 HITRAN database, distributed by AF Phillips Laboratory, Geophysics Directorate, Simulations Branch (Dr. L. Rotham).
65. T.W. Monarski, "Frequency Stabilization of Nd:YAG Lasers," M.S. Thesis (University of New Mexico, Albuquerque, NM, 1996) Chap. 4.

LIST OF VARIABLES (BY CHAPTER)

Chapter 2

Symbol	Name/Description
C_r	radial photoelastic coefficient
C_ϕ	tangential photoelastic coefficient
f_{ic}	slave resonator intracavity lens focal length
K	thermal conductivity
L_c	slave resonator length
L_r	Nd:YAG rod length
n_0	index of refraction at rod center
$n_r \textcircled{r}$	radial index of refraction (r polarization)
$n_\phi \textcircled{\phi}$	radial index of refraction (ϕ polarization)
P_{in}	transverse pump power
$P_{in,max}$	maximum allowable transverse pump power
r_0	Nd:YAG rod radius
R_{end}	rod end-face curvature
R_{oc}	power reflectivity of output coupler
α	thermal coefficient of expansion
β_r	radial quadratic index of rod
β_ϕ	tangential quadratic index of rod
η_T	percentage of P_{in} absorbed as heat in rod

Chapter 3

Symbol	Name/Description
AOM	acousto-optic modulator
C1, C2, C3	capacitors of servo
E_0	real amplitude of electric field output of laser
E_{Laser}	complex electric field output of laser
EOM	electro-optic modulator
G_{CL}	closed loop transfer function of feedback loop
G_{OL}	open loop transfer function of feedback loop
K_A	complex actuator transfer function
K_D	complex discriminator transfer function
K_S	complex servo transfer function
N_a	actuator point (located at exit of servo)
N_e	error point (located at entrance to servo)
PZT	piezo-electric transducer
R1, R2, R3	resistors of servo
$S_{A,\text{Laser}}$	spectral density of amplitude noise of the laser
$S_{f,\text{REF}}$	spectral density of frequency noise of the frequency reference
$S_{f,\text{Sig}}$	spectral density of frequency noise of known noise signal placed on the laser
$S_{f,\text{CL}}$	closed loop spectral density of frequency noise of laser
$S_{f,\text{fbck}}$	spectral density of frequency noise of master laser
$S_{f,\text{Laser}}$	spectral density of frequency noise of master laser
S_V	spectral density of voltage noise
$S_{V,D}$	spectral density of voltage noise of discriminator
$S_{V,S}$	spectral density of voltage noise of servo
$S_{\phi,\text{Laser}}$	spectral density of phase noise of laser
UGBW	bandwidth of open loop gain transfer function
$\Delta\nu$	frequency bin width of spectrum measurement device

Σ	frequency or voltage summer
Σ_1	frequency summer where noise frequency is subtracted from output frequency of laser
ϕ_{CL}	phase of closed loop transfer function of feedback loop
ϕ_{Laser}	instantaneous phase noise of the laser field
ϕ_{OL}	phase of open loop transfer function of feedback loop
$v_{CL}(t)$	instantaneous closed loop frequency output of laser
v_{corner}	corner frequency of the servo (noise frequency where gain vs. frequency slope changes from -12 dB/Oct to -6 dB/Oct)
$v_{fb}(t)$	instantaneous noise frequency negatively fed back to the laser
$v_{Laser}(t)$	instantaneous frequency output of laser
$v_{REF}(t)$	instantaneous frequency of the reference
v_{UG}	unity gain frequency of open loop gain transfer function
ω_0, ν_0	carrier frequency of laser
ω_n, ν_n	noise oscillation frequency

Chapter 4

Symbol	Name/Description
c	speed of light
D	common denominator of frequency noise transfer functions
e	charge of an electron
E_1	field amplitude at point 1
E_2	field amplitude at point 2
E_3	field amplitude at point 3
E_c	amplitude of cavity circulating field
E_{inc}	amplitude of electric field incident on Fabry-Perot
E_r	reflected field amplitude
FSR	free spectral range
G_v	current to voltage gain of photodetector
I_r	intensity of reflected Fabry-Perot field
J_0, J_1	zero and first order Bessel functions
L	length of Fabry-Perot
NPRO	non-planar ring oscillator (off the shelf solid-state laser from Lightwave Electronics, Inc.)
PBSC	polarizing beam splitter cube
PD	photodiode
PDH	Pound-Drever-Hall FM sideband locking technique
R_1	power reflectivity of input/output coupler of Fabry-Perot
R_2	back mirror reflectivity of Fabry-Pert
R_2	power reflectivity of back mirror of Fabry-Perot
R_{resp}	responsivity of photodiode
s	defined to equal $i\omega_n$
$S_{A,m}$	spectral density of amplitude noise of master laser
$S_{A,r}$	spectral density of amplitude noise of cavity reflected field
$S_{f,c}$	spectral density of frequency noise of cavity resonant frequency

$S_{f,m}$	spectral density of frequency noise of master laser
$S_{f,r}$	spectral density of frequency noise of cavity reflected field
$S_{V,D,AM}$	spectral density of voltage noise at discriminator output caused by amplitude noise
$S_{V,D,SN}$	spectral density of voltage noise at discriminator output caused by shot noise
$S_{\phi,c}$	spectral density of phase noise of resonant frequency of the cavity
$S_{\phi,m}$	spectral density of phase noise of master laser
$S_{\phi,r}$	spectral density of phase noise of cavity reflected field
T	round trip time of circulating field
T_1	time it takes laser to swing through $2\nu_p$
T_2	time it takes laser to swing through $\delta\nu_c$
T_C	transfer function of phase noise caused by Fabry-Perot length fluctuations onto the circulating field
$T_{HIGH}(\nu_n, \nu_{corner})$	high pass filter with respect to ν_n , of corner frequency ν_{corner}
T_L	transfer function of phase noise of incident laser onto the circulating field
$T_{LOW}(\nu_n, \nu_{corner})$	low pass filter with respect to ν_n , of corner frequency ν_{corner}
U_c	energy of cavity circulating field
V_c	mode volume of cavity circulating field
V_{Det}	voltage output of photodetector
ΔV_A	voltage applied to NPRO PZT to cause it to swing through $2\nu_p$
ΔV_D	voltage applied to NPRO PZT to cause it to swing through $\delta\nu_c$
$\Delta\phi_{ss}$	steady-state phase delay of the cavity reflected field with respect to the incident field
α_0	absorption coefficient of Fabry-Perot medium
β	modulation index for PDH sidebands
$\delta\nu_c$	full width at half maximum of cavity power reflection coefficient
ϵ	permittivity of Fabry-Perot medium

ϕ_c	phase noise of cavity circulating field
ϕ_m	phase noise of master laser
ϕM	phase modulator
γ_0	energy decay rate due to internal losses
γ_2	energy decay rate due to transmission through mirror R_2
γ_c	total energy decay rate
γ_e	energy decay rate due to transmission through output coupler, R_1
η	constant defined to simplify discriminator transfer function equals K_D in regime $\nu_n < \delta\nu_c/2$
κ	ratio of noise frequency to half width at half maximum (i.e. $\nu_n / \delta\nu_c/2$)
λ	constant defined to simplify terms
$\lambda/4$	quarter wave plate
τ_p	photon lifetime of cavity
ω_c, ν_c	resonant frequency of cavity
ω_m, ν_m	carrier frequency of master laser
ω_n, ν_n	noise oscillation frequency
ω_p, ν_p	PDH modulation sideband frequency

Chapter 5

Symbol	Name/Description
E_{IL}	injection-locked electric field amplitude
E_m	electric field amplitude of master laser
E_s	electric field amplitude of slave laser
$N_{a,IL}$	actuator point of injection-locking PDH loop
$N_{e,IL}$	error point of injection-locking PDH loop
P	polarization of slave laser gain medium atoms
PDH	Pound-Drever-Hall FM sideband locking technique
P_{IL}	power of injection-locked output
P_m	total power of master laser
$S_{A,IL}$	spectral density of amplitude noise of injection-locked output
$S_{f,IL}$	spectral density of frequency noise of injection-locked output
$S_{\phi,IL}$	spectral density of phase noise of injection-locked output
$S_{\phi,m}$	spectral density of phase noise of master laser
$S_{\phi,s}$	spectral density of phase noise of slave laser
T_M	open loop transfer function of master laser frequency noise onto injection-locked output (in absence of PDH loop)
T_{oc}	power transmission of output coupler
T_s	open loop transfer function of slave resonator frequency noise onto injection-locked output (in absence of PDH loop)
V_{Det}	voltage output of photodiode
V_{Sig}	voltage output of photodiode at modulation frequency
$\Delta\phi_{ss}$	steady-state phase delay of injection-locked output field and incident master laser field
χ'	in phase polarization term
χ''	out of phase polarization term
$T_{s,CL}$	closed loop version of T_s (in presence of PDH control loop) in fact $T_{s,CL} = T_s$

ϕ_{IL}	phase noise of injection-locked output field
ϕ_{IL}	phase noise of injection-locked output
ϕ_m	phase noise of master laser
ϕ_s	phase noise of slave laser
$T_{M,CL}$	closed loop version of T_M (in presence of PDH control loop)
γ_m	circulating field growth rate
η_{IL}	constant defined to simplify discriminator transfer function of injection-locking PDH loop
κ_{IL}	ratio of noise frequency to lock range frequency
ω_p, ν_p	PDH modulation frequency
$\omega_{pull}, \nu_{pull}$	pulled resonant frequency of the slave resonator
$\omega_{Lock}, \nu_{Lock}$	lock range frequency
ω_m, ν_m	carrier frequency of master laser
ω_s, ν_s	carrier frequency of unseeded slave laser and resonant frequency of the seeded slave cavity

Chapter 6

Symbol	Name/Description
E_{IL}	injection-locked electric field amplitude
E_{PD3}	total electric field amplitude incident of PD3
E_{REF}	electric field amplitude of reference laser, NPRO1
f_k	the k^{th} RAV frequency measurement at a particular τ
FSR	Free Spectral Range of Fabry-Perot reference cavity
G_V	current to voltage gain of photodiode
$K_{A,IL}$	actuator coefficient of PZT mounted on slave resonator mirror for PDH injection-locking control loop
$K_{A,IL1}$	actuator coefficient of slave resonator PZT 1
$K_{A,IL2}$	actuator coefficient of slave resonator PZT 2
K_{A2}	actuator coefficient of NPRO2
$K_{D,IL}$	discriminator coefficient of PDH injection-locking control loop
$K_{D,IL1}$	discriminator coefficient of PDH injection-locking control loop containing slave resonator PZT 2
N	number of individual frequency measurements made to obtain RAV
$N_{a,IL}$	actuator point of injection-locking PDH loop (located at exit of servo)
$N_{e,IL}$	error point of injection-locking control loop (located at entrance of servo)
NPRO1	reference laser for various beatnote measurements
NPRO2	master laser of PDH injection-locking system
PD3	photodiode 3
PDH	Pound-Drever-Hall FM sideband locking technique
P_{IL}	optical injection-locked output power
P_m	optical power of the master laser
P_{REF}	optical power of reference laser, NPRO1
RAV	Root Allan Variance time domain measurement of frequency

	noise
R_{esp}	responsivity of photodiode
$S_{f,\text{IL}}$	spectral density of frequency noise of injection-locked output
$S_{f,\text{m}}$	spectral density of frequency noise of the master laser
$S_{f,\text{s}}$	spectral density of frequency noise of the slave laser
$S_{\phi,\text{IL}}$	spectral density of phase noise of injection-locked output
$S_{\phi,\text{m}}$	spectral density of phase noise of master laser
$S_{\phi,\text{REF}}$	spectral density of phase noise of reference laser, NPRO1
$S_{\phi,\text{s}}$	spectral density of phase noise of slave laser
T_{M}	open loop transfer function of master laser frequency noise onto injection-locked output (in absence of PDH loop)
T_{M}	transfer function of master laser frequency noise onto injection-locked output
T_{oc}	power transmission of output coupler
T_{oc}	power transmission coefficient of slave laser output coupler
T_{S}	open loop transfer function of slave resonator frequency noise onto injection-locked output (in absence of PDH loop)
T_{S}	transfer function of slave laser frequency noise onto injection-locked output
V_{PD3}	voltage output of photodiode 3
β	PDH modulation index
σ	RAV output: measure of frequency stability in time domain
τ	time interval of a particular RAV measurement
$\omega_{\text{FSR}}, \nu_{\text{FSR}}$	FSR frequency of the Fabry-Perot reference cavity
$\omega_{\text{Lock}}, \nu_{\text{Lock}}$	lock range frequency
$\omega_{\text{n}}, \nu_{\text{n}}$	noise oscillation frequency
$\omega_{\text{m}}, \nu_{\text{m}}$	carrier frequency of master laser
$\omega_{\text{p}}, \nu_{\text{p}}$	PDH modulation frequency

Chapter 7

Symbol	Name/Description
c	speed of light
E_c	amplitude of doubler cavity circulating pump field
E_{inc}	total incident electric field amplitude
$E_{inc}(H)$	horizontally polarized component of incident laser field
$E_{inc}(V)$	vertically polarized component of incident laser field serves as pump field for the frequency doubling
E_{VIS}	electric field amplitude of frequency-doubled field
FSR	Free Spectral Range of doubler cavity
$G_{OL,D}$	open loop transfer function of the doubler control loop
G_V	current to voltage gain of photodiode
$K_{A,D}$	actuator coefficient of PZT mounted on doubler resonator mirror for frequency doubling control loop
$K_{D,D}$	discriminator coefficient of frequency doubling control loop
$K_{S,D}$	servo coefficient of frequency doubling control loop
$N_{a,D}$	actuator point of frequency doubler control loop (located at exit of servo)
$N_{e,D}$	error point of frequency doubler control loop (located at entrance of servo)
R_{ic}	input/output coupler of infra-red pump field
R_{oc}	output coupler of visible electric field
$S_{f,c}$	spectral density of frequency noise of resonant frequency of doubler cavity
$S_{f,m}$	spectral density of frequency noise of incident pump field from the laser
$S_{f,VIS}$	spectral density of frequency noise of generated visible field
$S_{\phi,c}$	spectral density of phase noise of resonant frequency of doubler cavity
$S_{\phi,IR}$	spectral density of phase noise of circulating infra-red pump field

$S_{\phi, \text{VIS}}$	spectral density of phase noise of generated visible field
T	round trip time of cavity circulating field
α_0	absorption coefficient of Fabry-Perot medium
$\chi^{(2)}(2\omega_m)$	second order susceptibility at the second harmonic frequency of the incident laser field
$\delta\nu_c$	full width at half maximum of cavity power reflection coefficient
γ_0	energy decay rate due to internal losses
γ_c	total energy decay rate
γ_e	energy decay rate due to transmission through input coupler, R_{ic}
η_D	constant defined to simplify discriminator transfer function of doubler cavity control loop
κ	ratio of noise frequency to half width at half maximum (i.e. $\nu_n / \delta\nu_c/2$)
ρ_H	horizontal component of incident laser electric field
ρ_V	vertical component of incident laser electric field
ω_c, ν_c	resonant frequency of the doubler cavity
ω_m, ν_m	carrier frequency of master laser
ω_n, ν_n	noise oscillation frequency